Copyright Warning & Restrictions

The copyright law of the United States (Title 17, United States Code) governs the making of photocopies or other reproductions of copyrighted material.

Under certain conditions specified in the law, libraries and archives are authorized to furnish a photocopy or other reproduction. One of these specified conditions is that the photocopy or reproduction is not to be "used for any purpose other than private study, scholarship, or research." If a, user makes a request for, or later uses, a photocopy or reproduction for purposes in excess of "fair use" that user may be liable for copyright infringement,

This institution reserves the right to refuse to accept a copying order if, in its judgment, fulfillment of the order would involve violation of copyright law.

Please Note: The author retains the copyright while the New Jersey Institute of Technology reserves the right to distribute this thesis or dissertation

Printing note: If you do not wish to print this page, then select "Pages from: first page # to: last page #" on the print dialog screen

ABSTRACT

THE ROLES OF INHIBITION IN C. ELEGANS LOCOMOTION

by
Lan Deng

Inhibition plays important roles in modulating neural activities at different levels from small synapses to brain regions, and different systems from sensory to motor. To achieve translocation, locomotor systems produce alternation of antagonist muscles, including axial posture and limb movement and alternation. In the nematode *C. elegans*, a cross-inhibition circuit, involving excitatory cholinergic and inhibitory GABAergic motoneurons, is believed to generate the dorsoventral alternation of body-wall muscles that supports backward undulatory locomotion. This dissertation challenges this prevalent hypothesis, delves into studying different roles of inhibition, and depicts the expression pattern and functional role of ionotropic $GABA_A$ receptor, UNC-49, in motoneurons and body-wall muscles in the locomotion circuit.

This dissertation demonstrates that the shrinking phenotype, formerly demonstrated only by harsh touch to the head of GABA transmission mutants, is exhibited by wild type as well as mutant animals in response to harsh touches to the head or tail and that only GABA transmission mutants show slow locomotion post-stimulation. Impairment of GABA transmission, either genetically or optogenetically, induces lower undulation frequency and lower translocation speed during crawling and swimming in both directions. GABAergic motoneurons' activity pattern is different during low and high undulation frequency. During low undulation frequency, GABAergic VD and DD motoneurons show a similar activity pattern; while during high undulation frequency their activity alternate. The experimental results suggest at least three possible roles for inhibition that we test with

a computational model – cross-inhibition or disinhibition of body-wall muscles, and inhibitory reset or disinhibition of cholinergic VA and VB motoneurons – that could underlie fast undulatory locomotion in *C. elegans*.

This dissertation also shows the distribution of ionotropic $GABA_A$ receptor, UNC-49, in motoneurons and body-wall muscle cells, and demonstrates the contribution of UNC-49 to fast undulatory locomotion at different elements of the locomotion circuit. Besides formerly reported expression in body-wall muscles, UNC-49 also expresses in GABAergic motoneurons and the promoter *unc-49p* induces gene transcription in cholinergic VA and VB motoneurons. Tissue-specific rescue demonstrates the UNC-49 in body-wall muscles plays the most important role in sustaining fast undulatory locomotion.

The experimental optimization in the dissertation projects is elaborated, including synchronized two-channel calcium imaging, big plasmid construction using Gibson Assembly, and NeuroPAL imaging using confocal microscopy.

The results of this dissertation demonstrate that GABAergic motoneurons are not necessary for dorsoventrally undulatory locomotion in *C. elegans*, while they are critical for sustaining fast locomotion. Ionotropic $GABA_A$ receptor, UNC-49, expresses in body-wall muscles as well as GABAergic motoneurons and cholinergic VA and VB motoneurons but contributes to sustaining fast undulatory locomotion mostly via synapses from GABAergic motoneurons to body-wall muscle cells.

THE ROLES OF INHIBITION IN C. ELEGANS LOCOMOTION

by
Lan Deng

A Dissertation
Submitted to the Faculty of
New Jersey Institute of Technology
and Rutgers, The State University of New Jersey - Newark
in Partial Fulfillment of the Requirements for the Degree of
Doctor of Philosophy in Biology

Federated Biological Sciences Department

May 2020

.

APPROVAL PAGE

THE ROLES OF INHIBITION IN C. ELEGANS LOCOMOTION

Lan Deng

Dr. Gal Haspel, Dissertation Advisor — Date
Assistant Professor of Federated Biological Sciences Department
New Jersey Institute of Technology
and Rutgers, The State University of New Jersey – Newark

Dr. Farzan Nadim, Dissertation Committee Chair — Date
Professor of Federated Biological Sciences Department
New Jersey Institute of Technology
and Rutgers, The State University of New Jersey – Newark

Dr. Daphne F. Soares, Dissertation Committee Member — Date
Assistant Professor of Federated Biological Sciences Department
New Jersey Institute of Technology
and Rutgers, The State University of New Jersey – Newark

Dr. Eric S. Fortune, Dissertation Committee Member — Date
Associate Professor of Federated Biological Sciences Department
New Jersey Institute of Technology
and Rutgers, The State University of New Jersey – Newark

Dr. Andrew M. Leifer, Dissertation Committee Member — Date
Assistant Professor of Physics Department
and the Princeton Neuroscience Institute
Princeton University

BIOGRAPHICAL SKETCH

Author: Lan Deng

Degree: Doctor of Philosophy

Date: May 2020

Undergraduate and Graduate Education:

- Doctor of Philosophy in Biological Sciences,
  New Jersey Institute of Technology and Rutgers, The State University of New Jersey - Newark, Newark, NJ, 2020

- Bachelor of Engineering in Life Science and Biotechnology,
  China Pharmaceutical University, Nanjing, Jiangsu, P. R. China, 2011

Major: Biological Sciences

Presentations and Publications:

Deng L, Denham JE, Yuval O, Cohen N, Haspel G. Inhibition underlies fast undulatory locomotion in *C. elegans*, submitted.

Anwar H, Saghafi S, Deng L, Denham JE, Cohen N, Diekman CO, Haspel G. Bidirectional undulatory output is shaped by connections in distributed coupled-oscillators model of *C. elegans* locomotion network, in preparation.

Deng L, Haspel G. The roles of inhibition in *C. elegans* locomotion. The New York Area Worm Meeting-Winter 2019, New York City, New York, USA, Jan 2020.

Deng L. *C. elegans*. "From Behavior to Brains: The Neuroethological Way to Neuroscience" Society for Neuroscience Virtual Conference, USA, April 2019.

Deng L, Denham JE, Ranner T, Yuval O, Arya C, Cohen N, Haspel G, Inhibitory reset supports fast locomotion, CeNeuro 2018, Madison, Wisconsin, USA, June 2018.

Deng L, Marfil V, Doyle C, Haspel G. Cross-inhibition is crucial in fast undulatory locomotion in *C. elegans*. Society for Neuroscience Annual Meeting, Washington D.C, USA, November 2017.

Deng L. Inhibition sharpens locomotion in *C. elegans*. 6th Small Circuits and Behavior Meeting, Philadelphia, Pennsylvania, USA, August 2017.

Deng L, Marfil V, Doyle C, Haspel G. The roles of cross-inhibition in *C. elegans* locomotion. 21st International *C. elegans* Conference, Los Angeles, California, USA, June 2017.

I would like to dedicate this dissertation to my parents Jiayuan Deng and Qionghui Shen who always support my decisions.

献给在这个世界上我最好的爸爸妈妈，
谢谢你们把我带到这个世界，给了我一个自由快乐的童年，
也谢谢你们在我长大后无条件支持我做的每一个决定。
——永远爱你们的女儿

ACKNOWLEDGMENT

Throughout the past six years, I have felt extremely lucky to meet and know so many kind and smart people. I would like to take this opportunity to acknowledge some of them.

First and most important, I would like to acknowledge my knowledgeable, patient, and supportive advisor Dr. Gal Haspel, who helped me to develop my dissertation project from my laboratory rotation and connected me to excellent collaborators and peers. I have benefitted greatly from his guidance. I would also like to thank my other dissertation committee members. Dr. Farzan Nadim has always been supportive, and he guided me through different phases of my Ph.D. study, from helping me choose my program, courses, and laboratory to serving as my dissertation chair. Dr. Daphne Soares and Dr. Eric Fortune provided me constructive advice about the behavioral study, and Dr. Andrew Leifer gave me great advice about calcium imaging.

Second, I would like to acknowledge all the people who helped me in my research: our first laboratory technician Craig Schindewolf; our remarkable postdoc Dr. Vanessa Vives; great collaborators and friends including the Netta Cohen laboratory, the Ian Hope laboratory, Dr. Haroon Anwar, Dr. Anthony Fouad, Omer Yuval, Jack Denham, Dr. Eviatar Yemini and Thomas Geer; the laboratories or organizations that offered us *C. elegans* strains including the Caenorhabditis Genetics Center of the University of Minnesota, the Shin Takagi Laboratory of Nagoya University, the Christopher Fang-Yen Laboratory of the University of Pennsylvania, the Oliver Hobert Laboratory of Columbia University; and my sweet laboratory members Zainab Tanvir, Maria Belen Harreguy, Samiksha Vittalraj, Lianhua Jin, Supriya Kannan, Charu Aryu, Conor Jdoyle, Assma Itani, Hardik Darji and Anmol Mittal. Moreover, thank you to whomever provided mental and

health support whether intentionally or unintentionally: Dr. Nelly Daur, Dr. Anna C. Schneider, Marina Polak Yoffe, Elizabeth Cronin, Omar Itani, Smita More-potdar, Stefanie Margulies, Karen Roach, Shamay Carty, Sherri M. Brown, Yinbo Chen, Dr. Xinping Li, Dr. David Fox, Dr. Krish Pillai, Dr. Diana Martinez, Dr. Kristen Severi, Dr. Dirk Butcher, Dr. Horacio Rotstein, Dr. Jorge Golowasch, Dr. Erjian Zhang, Xiang Lin, Yingxi Tang, Dr. Xiaotang Ma, Dr. Leng Biao, Xindi Ruan, Luo Jia, Dr. Gan Luan, Dr. Ke Gen, Dr. Lun Li, Dr. Guoqiang Wang, Dr. Binhong Hao, and Xueyang Fan. Finally, thank you to the two great universities that fostered my doctoral program research: New Jersey Institute of Technology and Rutgers University.

Last, a million thanks to my beloved husband Chuanlong Cui who is always by my side whenever I need him, and to my parents Jiayuan Deng and Qionghui Shen, who are supportive of whatever decisions I make, even if they have no clue what my research means. Finally, sincere thanks go out to all my foster dogs and to the other dogs that appeared in my life over the last six years. You made my Ph.D. life more colorful.

TABLE OF CONTENTS

TABLE OF CONTENTS
(Continued)

Chapter **Page**

TABLE OF CONTENTS
(Continued)

Chapter **Page**

TABLE OF CONTENTS
(Continued)

Chapter **Page**

TABLE OF CONTENTS
(Continued)

Chapter **Page**

LIST OF TABLES

LIST OF FIGURES

LIST OF FIGURES
(Continued)

LIST OF FIGURES
(Continued)

Figure **Page**

CHAPTER 1

INTRODUCTION

1.1 Objective

The objective of this dissertation is to understand the role of neural inhibition in the generation of rapid behavior and determine the roles of neural inhibitory elements, including inhibitory GABAergic motoneurons and an ionotropic $GABA_A$ receptor, in supporting fast undulatory locomotion in *C. elegans*.

1.2 Background

1.2.1 *C. elegans* as a model animal

Caenorhabditis elegans (*C. elegans*) is a small (~ 1 mm in adult) non-parasitic cylindrical shape nematode. In nature, this small creature lives in soil and feeds on bacteria and microbes. In contrast to its small size, it has tremendous contributions in many fields of biology that was recognized by three Nobel prizes: for the studies in programmed cell death awarded in 2002, RNA interference awarded in 2006, and the use of green fluorescent protein awarded in 2008. *C. elegans* is an easy handle experimental organism. They can be maintained on agar plates or liquid cultures with *E. coli* as their food source. The majority of *C. elegans* are self-producing hermaphrodites which can produce both oocytes and sperms. Under stressful environment, there will be a higher chance of the advent of males. The life cycle of hermaphrodites from embryo to adult is 3.5 days at 20°C in the optimal environment (Figure 1.1); the life cycle decreases while the environmental temperature increases (e.g. 25°C) and increases at low temperature (e.g. 15°C) (Byerly et al., 1976).

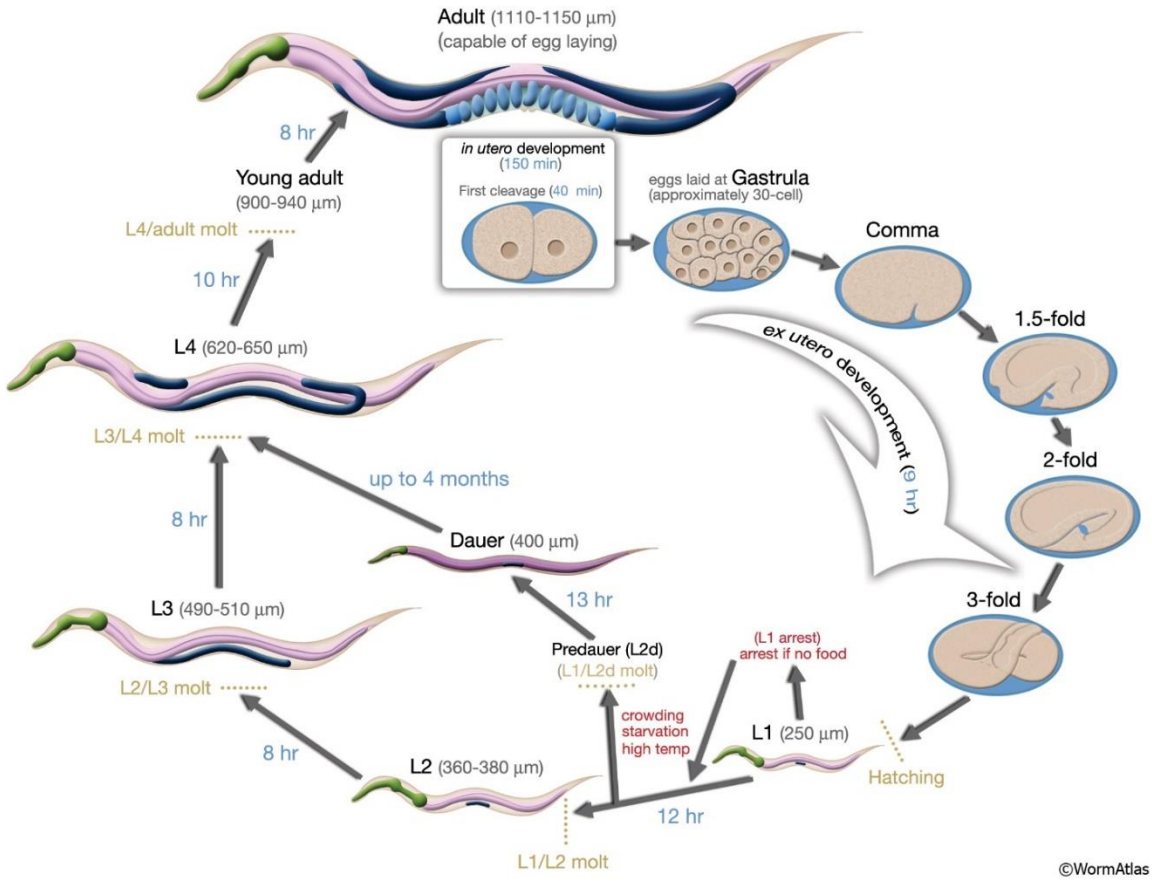

Figure 1.1 The length of the life cycle varies with environmental temperatures and conditions. At 20˚C, each animal grows into an adult from a hatched egg in 3.5 days involving four larval stages. The first larval stage (L1) is when the animal is freshly hatched. In the optimal environmental condition, L1 animals will molt and enter to the second larval stage (L2) to the fourth larval stage (L4) then become adult animals. In unfavorable environmental condition, L1 animals will undergo dauer arrest, and jump to the fourth larval stage directly in good environmental condition. The life cycle of *C. elegans* decreases while the temperature goes up (e.g. 25˚C) and increases while the temperature decreases (e.g. 15˚C). Adapted from Wormatlas (https://www.wormatlas.org/hermaphrodite/introduction/Introframeset.html, accessed on Feb 20th 2020).

Under optimal standard laboratory conditions, each hermaphrodite can produce 200-300 offspring that can be genetically assigned to their single parent (Brenner, 1974). *C. elegans* has a compact nervous system with almost fully mapped neuronal connections: hermaphrodites have 959 somatic cells including 302 neurons, while males have 1031 cells including 385 neurons (Sulston and Horvitz, 1977; Sulston et al., 1983). Besides, *C.*

elegans is the first multicellular organism of which the genome has been fully sequenced (Consortium, 1998) and the first transgenic model animal to express fluorescent proteins (Chalfie et al., 1994). After years of study, there are many powerful transgenic and optogenetic tools are available in *C. elegans*.

1.2.2 Locomotion of *C. elegans*

In the 1970s, Sydney Brenner established nematode *C. elegans* as an experimental organism to fill the gap between gene codes and the complex nervous system. *C. elegans* generate undulatory locomotion by propagating the dorsoventral body bends along the

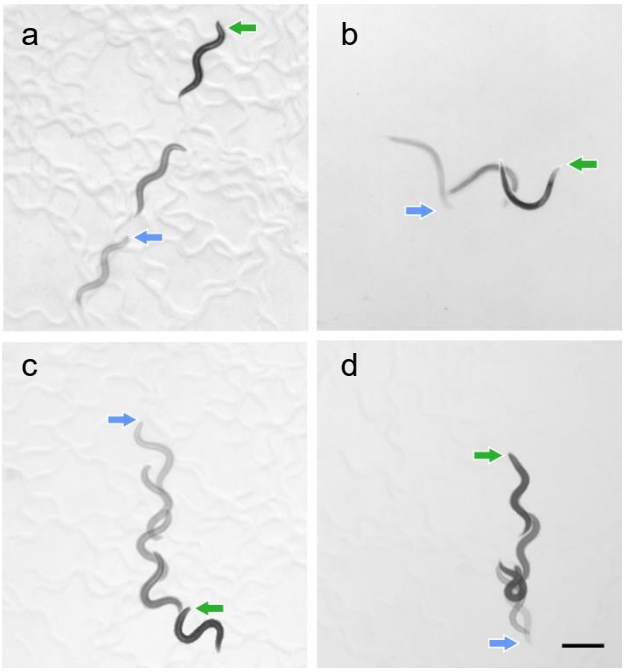

Figure 1.2 *C. elegans* moves in an undulatory pattern, propagating bends along its body against the direction of movement. The wavelength and amplitude of the locomotion cycle depend mainly on the resistance of the environment, and they are shorter for viscous fluids or high surface tension. Forward crawling on an agar plate (a) produces shorter wavelength and smaller amplitude than swimming in liquid (b). Less frequent behaviors, reversals (c) and turns (d), are also prominent and stereotypic during crawling and swimming (not shown). Blue arrows indicate the head position at the beginning of a sequence and the green arrows indicate the head position of the same animal at the end. The sequence lengths for a - d are 12 s, 1 s, 10 s and 14 s, respectively, note that undulation frequency is higher for swimming. Scale bar = 0.5 mm.

body against the direction of locomotion (Gray and Lissmann, 1964). Such distinct and rigorous behaviors facilitate the study of the nervous system by exposing subtle changes in behavior that could be traced back to altered neural activity. In Brenner's 1974 paper (Brenner, 1974), he reported a large number of behavioral mutants that he named with 'unc' (short for 'uncoordinated'). The locomotion of *C. elegans* changes in different ambient environments. When the animals are under high mechanical loads, like when crawling on the agar surface, they produce an 'S' shape sinusoidal pattern with wavelengths that are shorter than body length (Figure 1.2a). When under low mechanical loads, like when swimming in liquid, the animals produce a 'C' shape sinusoidal pattern with larger wavelengths (Figure 1.2b). Other than the differences in shape, the dorsoventral bending frequencies of crawling and swimming behaviors are different: the animals crawl at low frequency (around 0.4 Hz) and swim at high frequency (around 1.5 Hz) in both directions of locomotion. Other than the bidirectional undulatory crawling and swimming, *C. elegans* can generate a larger single curve until it touches or crosses over the posterior of the body (Figure 1.2d); these large bending behaviors are called Omega- or Delta-turns, respectively (Broekmans et al., 2016), and are usually associated with directional changes during avoidance response and chemotaxis behavior.

In this dissertation, we focus on the bidirectional crawling and swimming behaviors of adult hermaphrodite animals.

1.2.3 The locomotion neural circuit

The structure of the *C. elegans* nervous system has been mostly mapped by serial section electron microscopy, so most of the neuron morphology and cell connections are known (White et al., 1976, 1986). Their nervous system can be roughly categorized into ganglia

in the head and tail composed mostly of somata of sensory and interneurons, and dorsoventral nerve cord where a row of somata of motoneurons are situated at the ventral midline (Figure 1.3). The locomotion circuit is composed of five pairs of descending premotor interneurons (sometimes erroneously referred to as 'command neuron') from the head and tail ganglia, and 75 cholinergic and GABAergic motoneurons in the ventral nerve cord. These motoneurons are divided by their morphology into 8 classes that together innervate 95 muscle cells arranged in four transverse quadrants along the body. Different sets of motoneurons are active and different sets of premotor interneurons are required during bidirectional forward and backward locomotion (Chalfie et al., 1985; Haspel et al., 2010). During forward locomotion, PVC and AVB are primarily required, and they make contact to dorsal and ventral B-type motoneurons that mainly drive forward locomotion in the motor neuronal circuit via chemical synapses and gap junctions, respectively. During backward locomotion, AVA, AVD, and AVE are involved (Chalfie et al., 1985). These premotor interneurons make contact with dorsal and ventral A-type motoneurons that drive forward locomotion via chemical synapses and gap junctions: AVA contacts A-type motoneuron via both contacts, AVD via a chemical synapse, and AVE via chemical synapses in the anterior body (de Bono and Maricq, 2005).

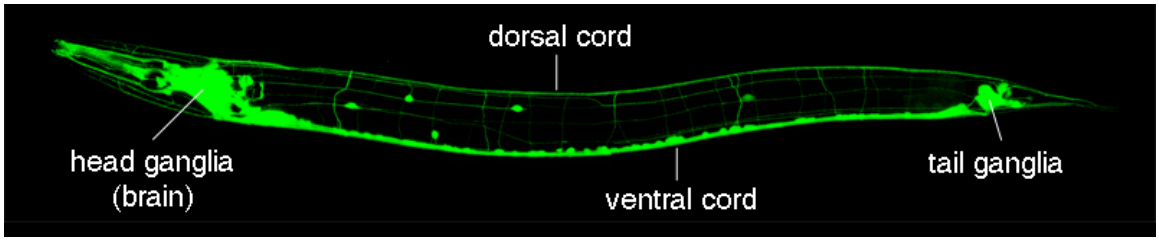

Figure 1.3 *C. elegans* nervous system (in green, labeled by GFP) is comprised the ganglia on the head (also considered as the brain, and called nerve ring), the ganglia on the tail, and ventral and dorsal nerve cords. All the somata of motoneurons locate in the ventral nerve cord.

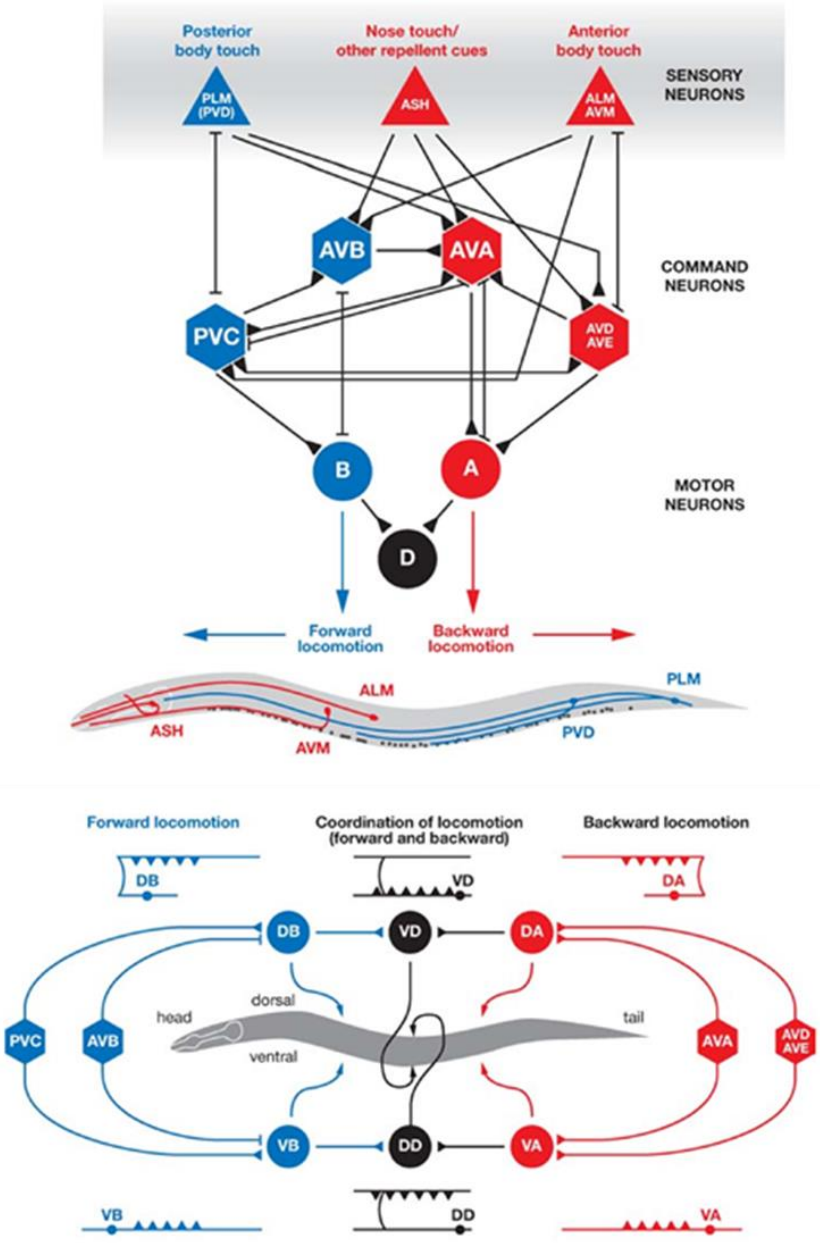

Figure 1.4 The motor neural circuit composes premotor neurons: AVB, PVC, AVA, AVD and AVE (*hexagons),* and motoneurons: B-type, A-type and D-type (*circles*). These neurons make contact via chemical synapses (*small black triangles*) and gap junctions (*T-ended lines*). The chemical synapses from ALM and AVM to PVC, from PLM to AVD, and from ASH to AVA, AVB, AVD, and AVE are inhibitory. Directional response to touch can be driven by input from mechanosensory neurons (PLM, PVD, ASH, ALM, AVM, *triangles*). The neurons in blue primarily involve in forward locomotion, and those in red involve in backward locomotion. Derived from de Bono and Maricq (2005).

The body-wall muscle cells are arranged in four quadrants along the body with two rows of muscle cells in each quadrant. Motoneurons do not synapse to body-wall muscle cells directly, but to processes extended from each muscle cell, called ‘muscle arms’. A-type and B-type motoneurons are cholinergic excitatory each with a ventral and a dorsal class: 12 VA, 9 DA, and 11 VB, 7 DB. Ventral motoneurons (VA and VB) innervate and excite the body-wall muscles on the ventral side, and dorsal motoneurons (DA and DB) excite body-wall muscles on the dorsal side (Figure 1.4 and 1.5).

Cholinergic motoneurons also innervate the GABAergic inhibitory D-type motoneurons which do not receive input from premotor or sensory neurons. According to the body-wall muscle they innervate, GABAergic motoneurons are also categorized into two classes: 6 DD and 13 VD motoneurons; all morphologically shaped like the letter ‘H’ with processes in the ventral and dorsal cords connected by a commissural neurite. DD motoneurons are excited by VA and VB motoneurons via chemical synapses and inhibit dorsal body-wall muscles; correspondingly VD motoneurons are excited by DA and DB motoneurons and inhibit ventral body-wall muscles (Figure 1.4 and 1.5). In addition, there are chemical synapses between VD and DD motoneurons, while only VD motoneurons synapse to the ventral excitatory VA and VB motoneurons (White et al., 1976; Haspel and O'Donovan, 2011).

The 11 AS and 6 VC are cholinergic excitatory motoneurons that are mostly overlooked. AS is similar to DA morphologically, except for shorter dorsal-anterior neurite. Unlike DA that is required for backward locomotion, AS is involved in bidirectional locomotion (Tolstenkov et al., 2018) and is innervated by both forward and backward premotor interneuron groups (White et al., 1976; Haspel and O'Donovan, 2011).

VC motoneurons innervate ventral body-wall muscle cells very sparsely, instead, they innervate dorsal GABAergic motoneurons (DD); two mid-body VC motoneurons innervate vulva muscles and are involved in egg laying (White et al., 1976, 1986; Haspel and O'Donovan, 2011; Emmons, 2015).

1.2.4 Neurotransmitters and their receptors in the motor circuit

In *C. elegans*, the main neurotransmitters are Acetylcholine (ACh), Glutamate (Glu) and Gamma-aminobutyric acid (GABA), as well as neuropeptides and biogenic amines, such as Dopamine, Tyramine, Octopamine, and Serotonin. Of these, ACh and GABA are the main neurotransmitters in the motor circuit.

ACh, which acts as an excitatory neurotransmitter in vertebrates neuromuscular junctions to skeletal muscles, plays a similar role in the nematode (Delcastillo et al., 1963; Del Castillo et al., 1967). A- and B-type motoneurons, as well as and VC, are cholinergic motoneurons. In these motoneurons, ACh is synthesized by choline acetyltransferase (ChAT, CHA-1), transported into transporter vesicles via vesicular acetylcholine transporter (VAChT, UNC-17), then released to the synaptic cleft to activate the acetylcholine receptors (AChRs, many such as UNC-29, UNC-38, LEV-8, ACR-2, ACR-5, ACR-8) on the postsynaptic body-wall muscles or motoneurons. The *C. elegans* genome contains twenty-nine genes of AChR (Bargmann, 1998; Mongan et al., 1998). The levamisole L-type and nicotine N-type AChRs in body-wall muscles and a class of AChRs that are similar to L-type AChRs in composition but insensitive to levamisole in motoneurons have been identified (Fleming et al., 1997; Touroutine et al., 2005; Boulin et al., 2008).

GABA, which acts as a primary inhibitory neurotransmitter in the central nervous system in vertebrate, plays a similar role in the nematode neuromuscular junction to relax the body-wall muscles during locomotion. GABA is synthesized in the cytoplasm of GABAergic motoneurons by converting glutamate to GABA under the action of glutamic acid decarboxylase (GAD, UNC-25). Then GABA is transported by the vesicular GABA transporter (VGAT, UNC-46 and UNC-47) into the synaptic vesicle which will be released to the synaptic cleft (Schuske et al., 2004). In the enteric system, GABA is excitatory and induces muscle contraction during defecation. Five ionotropic $GABA_A$ receptors subunits have been reported to express in locomotion motoneurons. GAB-1, LGC-35 and LGC-37 express in DA and DB motoneurons; GAB-1, LGC-35, LGC-36, LGC-37 and LGC-38 express in VA and VB motoneurons; GAB-1 and LGC-37 express in AS and VC motoneurons (Bamber et al., 1999; Jobson et al., 2015; Gendrel et al., 2016). LGC-35 expresses in cholinergic A and B motoneurons and was reported to serve a modulatory function receiving extrasynaptic spillover GABA signal (Jobson et al., 2015; Nicholl et al., 2017). The functions of GAB-1, LGC-36, LGC-37, and LGC-38 in locomotion are unknown. GAB-1, LGC-37, and UNC-49, as well as EXP-1 which is an excitatory GABA-gated cation channel mediating enteric muscle contraction (Beg and Jorgensen, 2003). No expression of $GABA_A$ receptor was reported in GABAergic motoneurons DD and VD.

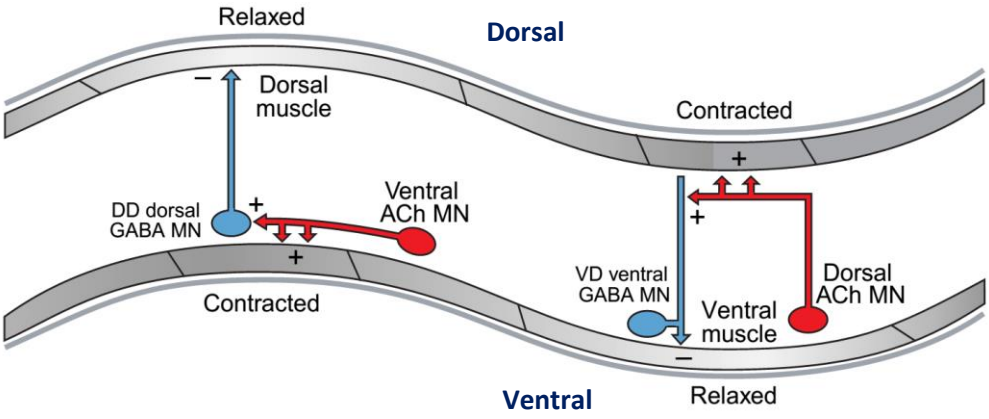

Figure 1.5 The dorsoventral cross-inhibition hypothesis of GABAergic D-type motoneurons. All motoneurons' cell bodies are in the ventral nerve cord (bottom) of *C. elegans*. It was suggested that when cholinergic motoneurons (red) activate the body muscles, they also activate postsynaptic GABAergic motoneurons (red), which in turn relax the contralateral body muscles. All the motoneurons synapse to muscle arms instead of muscle cell bodies in *C. elegans*. Adapted from Schuske and Jorgensen （2005）.

1.2.5 The morphology and connectivity of motoneurons suggest dorsoventral cross-inhibition

In *C. elegans*, a cross-inhibition circuit was suggested to coordinate dorsoventral body-wall muscle contraction, contributing to backward crawling locomotion (Figure 1.5) (McIntire et al., 1993b; Schuske et al., 2004). In this hypothesis, when for example a ventral cholinergic motoneuron (VA) activates its postsynaptic ventral muscle arms and dorsal GABAergic motoneuron (DD), the ventral muscle will contract while the opposing dorsal muscle with a muscle arm postsynaptic to DD will relax due to inhibition. Correspondingly, when the dorsal cholinergic motoneuron (AS, DA) is excited, its postsynaptic dorsal muscle arms and ventral GABAergic motoneuron (VD) will be activated as well, leading to dorsal muscle excitation and ventral muscle inhibition.

This prevalent cross-inhibition hypothesis is only partially supported. In mutants deficient in different components of GABA transmission (e.g. *unc-25, unc-46,* and *unc-49*; Figure 1.6), as well as animals in which GABAergic motoneurons had been laser ablated,

a touch to the head that would produce a rapid reverse undulation in a wild type animal is followed by a shrinking response. The GABA deficient animals shorten the anterior portion of their body and then propagate backward in a slow crawling speed (Figure 1.7). The shrinking phenotype suggests that dorsal and ventral body-wall muscles contract simultaneously (McIntire et al., 1993a; McIntire et al., 1993b), supporting a cross-inhibition mechanism. Further support to the hypothesis, the mutants were reported not to move backward and to seem to perform normal forward undulation, albeit with decreased undulatory amplitude. The shrinking phenotype was reported to be triggered only by head touching (McIntire et al., 1993b). However, this dissertation challenges this prevalent backward specific cross-inhibition locomotion hypothesis.

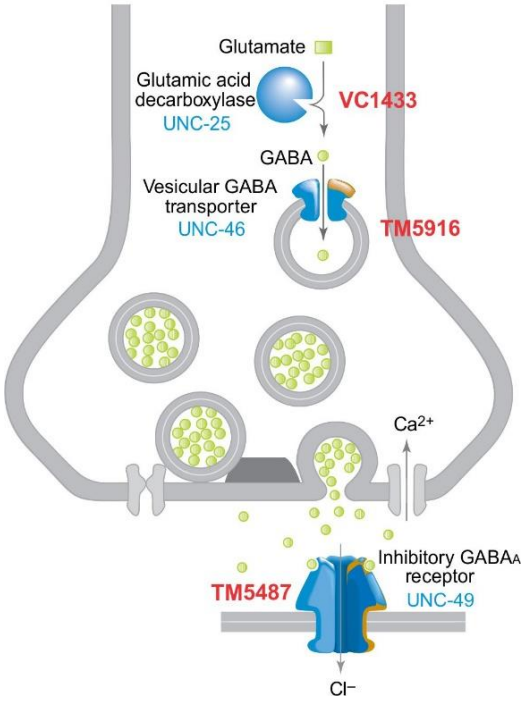

Figure 1.6 Genes *unc-25*, *unc-46* and *unc-49* encode different components of GABA transmission, from glutamic acid decarboxylase, vesicular GABA transporter to inhibitory $GABA_A$ receptor. The GABA transmission knockout strains used in Chapter 2 are VC1433, TM5916 and TM5487 are GABA transmission knockout strains in which hundreds to thousands base pairs of *unc-25*, *unc-46* and *unc-49* have been deleted, respectively**.** Adapted from Schuske and Jorgensen (2005).

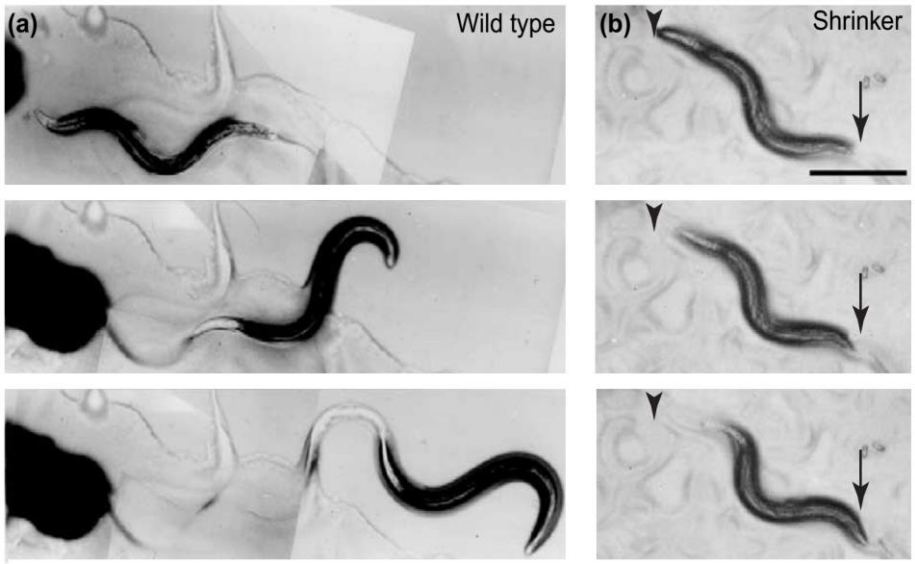

Figure 1.7 Escape responses of wild type animal and a GABA transmission mutant. (a) When a wild type nematode escapes from a touch to the head, it propagates backward rapidly. (b) However, the "shrinker" GABA transmission mutant shortens its anterior body first, then propagates backward. Scale bar 0.5 mm. Adapted from Schuske and Jorgensen (2005).

1.3 Outline

In this dissertation, there are two main stories about the inhibitory elements that support rapid dorsoventral alternation in *C. elegans*.

In the first story (Chapter 2), we focus on inhibitory GABAergic motoneurons which were suggested to play cross-inhibition to support dorsoventral body-wall muscle alternation during backward crawling. The defects in GABA transmission or GABAergic motoneurons were reported to fail to generate backward sinusoidal undulatory locomotion and produce body shrinkage after harsh stimulation to the head. However, we find that the shrinking phenotype exists in wild type and mutant animals regardless of locomotion direction. A combination of behavior analysis and optogenetic experiments show that when GABA transmission is defective genetically or GABAergic motoneurons are acutely

inhibited, the animal can still perform dorsoventral alternation, but in an uncoordinated manner. In addition, the crawling and swimming behaviors of these animals are slower with lower translocation speed and undulation frequency in forward and backward locomotion directions. Calcium imaging revealed cell activity that when plotted against cycle phase recording shows that the activity patterns of GABAergic motoneurons are different during low and fast undulation frequencies. During high undulation frequency, GABAergic motoneurons that innervate body-wall muscles of dorsal and ventral sides exhibit different and mostly opposing inactive phases. In contrast, during low undulation frequency, they exhibit similar activity patterns. Based on the calcium imaging results during high-frequency undulation, we suggest three inhibitory roles of GABAergic motoneurons: cross-inhibition to the body-wall muscles of the opposing side, disinhibition to the innervated body-wall muscles, and inhibitory reset of ventral GABAergic motoneuron. We test these hypothesized roles using a proprioceptive mechanical control model and a feedforward general pattern generator-like model.

In the second story (Chapter 3), we identify the expression pattern of UNC-49, an ionotropic $GABA_A$ receptor previously identified only in body-wall muscle cells. We find it also expresses in ventral nerve cord GABAergic motoneurons, and that its native promoter *unc-49p* initiates gene transcription in GABAergic and ventral-cholinergic motoneurons. In *unc-49* knockout animals, expression of full-length UNC-49 in either body-wall muscles, GABAergic motoneurons, or ventral cholinergic motoneurons, rescue fast locomotion when expressed specifically in body-wall muscle.

CHAPTER 2

INHIBITION UNDERLIES FAST UNDULATORY LOCOMOTION IN C. ELEGANS

2.1 Introduction

Alternating activation of antagonistic muscle is ubiquitous in motor programs. During locomotion, limbed animals alternate flexor-extensor muscles, as well as left and right counterparts; while limbless locomotion involves antagonistic axial muscles that generate body bending. To perform these rhythmic and symmetric behaviors, when one side of the body or the limb is driven by excitatory neurons, the antagonist is activated less, or inhibited, to allow movement. The generation of alternating pattern involves either direct or indirect cross-inhibitory pathways. In the tadpole, commissural GABAergic and glycinergic interneurons project contralaterally in the spinal cord, directly onto inter- and motoneurons (Roberts et al., 2008); in mammals, inhibitory interneurons inhibit contralateral motoneurons or commissural excitatory interneurons project on ipsilateral inhibitory interneurons to inhibit motoneurons indirectly. Limbed animals typically also transit among locomotion gaits, for example from walk to trot, gallop, and bound, as they increase moving speed (Kiehn, 2016). Inhibition serves multiple roles in the generation, maintenance, and modulation of the locomotive program. Hypotheses range from cross-inhibitory induced alternation of antagonists, postinhibitory rebound contributing to rhythm generation. Ascending interneurons produce recurrent inhibition of sensory pathways that gates reflex responses and limits firing of central pattern generator (CPG) neurons during locomotion; while descending interneurons can produce tonic or phasic

inhibition that reduce responsiveness and spontaneous locomotion, or stop it altogether (Roberts et al., 2008).

In *C. elegans*, GABAergic motoneurons were suggested, based on their morphology, connectivity, and mutant phenotype, to provide cross-inhibition necessary for backward crawling (McIntire et al., 1993a; McIntire et al., 1993b; Schuske et al., 2004). Notably, all the elements that compose the locomotion circuit and their connectivity are known (White et al., 1976, 1986; Chen et al., 2006; Emmons, 2015; Altun and Hall, 2020). The locomotion circuit is composed of 75 cholinergic and GABAergic motoneurons with somata within a ventral nerve cord, divided by their morphology into 4 excitatory cholinergic and 4 inhibitory GABAergic classes that innervate 95 muscle cells arranged along the body. The motoneurons synapse onto thin processes called muscle arms that are extended from muscle cells onto the ventral cord (White et al., 1976, 1986; Chen et al., 2006; Emmons, 2015; Altun and Hall, 2020). Muscle arms are functionally analogous to vertebrate motoneurons, while *C. elegans* motoneurons are functionally analogous to vertebrate spinal interneurons. Nineteen GABAergic motoneurons, six DD that innervate dorsal muscle and thirteen VD that innervate ventral muscle, are all shaped like the letter H with a dendrite and an axon connected by a commissural neurite. GABAergic inhibitory motoneurons receive inputs only from other motoneurons (White et al., 1976, 1986; Haspel and O'Donovan, 2011; Petrash et al., 2013). Each VD receives input from the dorsal excitatory cholinergic motoneurons (DA, DB, and AS) that innervate the opposing muscle cells, while DD motoneurons receive input from the ventral excitatory cholinergic motoneurons (VA and VB) (White et al., 1976, 1986; Haspel and O'Donovan, 2011). The GABAergic motoneurons also receive cholinergic input from VC motoneurons (Haspel

and O'Donovan, 2011). In addition to their synaptic output at neuromuscular junctions, opposing DD and VD motoneurons also innervate each other, whereas VD motoneurons also innervate the local VA and VB (Figure 2.1) (White et al., 1986; Haspel and O'Donovan, 2011). Laser ablation of either VD or DD motoneurons induces a bending bias towards the ablated side causing the animal to move in circles; while optogenetic activation or inactivation of DD motoneurons also induces ventral or dorsal bending, respectively (Donnelly et al., 2013). *C. elegans* that are defective in any part of their GABAergic transmission (the so-called *shrinker* mutants) respond to anterior noxious stimuli, such as a harsh touch to the head, with coactivation instead of alternation of antagonistic dorsoventral muscle, producing a shrinking response instead of the rapid reverse undulation seen in the wild type. The mutant animals, as well as the animal in which the GABAergic motoneurons had been laser ablated, shorten the anterior portion of their body and were reported not to move backward while performing normal forward crawling, albeit

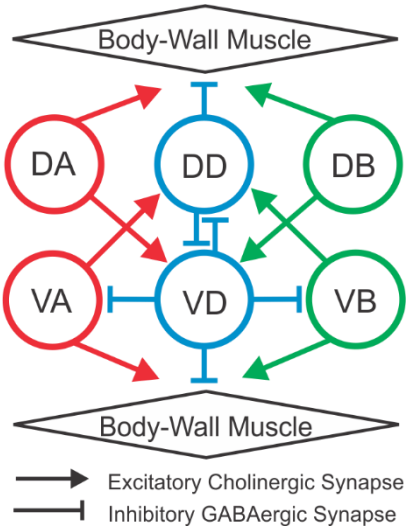

Figure 2.1 GABAergic motoneurons provide inhibition to body-wall muscles and motoneurons through three types of synapses. When cholinergic motoneurons (DA, DB, VA, VB, and AS not shown) activate body-wall muscle cells, they also activate postsynaptic GABAergic motoneurons, which in turn provide inhibition to contralateral body-wall muscles and motoneurons. All the motoneurons synapse to muscle arms that extend into the ventral nerve cord. Other than neuromuscular junctions, there are inhibitory synapses between DD and VD, and asymmetric synapses from VD to VA and VB.

with decreased undulatory amplitude (McIntire et al., 1993a; McIntire et al., 1993b). Hence it was suggested that GABAergic motoneurons mediate dorsoventral cross-inhibition, contributing to backward locomotion (McIntire et al., 1993b) or direction change (Schuske et al., 2004). In this hypothesis, when an excitatory cholinergic A motoneuron (e.g. VA) activates postsynaptic muscle arms and an inhibitory GABAergic motoneuron (e.g. DD) that inhibits and causes relaxation of the opposing muscle; shrinking is caused by the coactivation of A- and B-type cholinergic motoneurons, resulting from competition of their pre-motor interneurons. An alternative hypothesis is given in a computational study of forward locomotion (Boyle et al., 2012) which suggests that neural, rather than muscle, inhibition could play an important role. In this model, abolishing neural (VD to VB) inhibition is detrimental to rapid swimming in liquid, but not for slower crawling.

Here, to assess the relative contributions of these hypotheses, we quantify the response to harsh touch and spontaneous crawling and swimming behaviors of different GABA transmission mutants as well as an optogenetic strain in which GABAergic motoneuron can be inactivated acutely; we record the activity of GABAergic motoneurons with calcium imaging during low and high undulation frequencies; we suggest competing hypotheses for the roles of inhibition in *C. elegans* locomotion and test them with computational models.

2.2 Methods

2.2.1 *C. elegans* strains

We maintained *C. elegans* strains under the standard laboratory condition on Nematode Growth Medium (NGM) agar plates with OP-50-1 *Escherichia col*i (*E. coli*) bacterial lawn

at 20°C (Brenner, 1974; Corsi et al., 2015). All the animals we used in the experiments were hermaphrodites.

The *C. elegans* strains used in this study were N2, VC1433, TM5916, TM5487, TOL12, TOL15, TOL11, and CZ1632. We obtained N2 (a reference laboratory strain considered as wild type), VC1433 *[unc-25 (ok1901) III]*, and CZ1632 (*juIs76 [unc-25p::GFP + lin-15(+)]II*) strains from Caenorhabditis Genetic Center of University of Minnesota (https://cgc.umn.edu/), and TM5916 *[unc-46 (tm5916)]V*, and TM5487 *[unc-49 (tm5487)]III* from National Bioresource Project of Japan (https://shigen.nig.ac.jp/c.elegans/top.xhtml). We generated TOL11 (*aatIs11[Pmyo-3::R-CaMP2; Punc-25::G-CaMP6; Punc-47::ChR2::P2A::DsRed2; Podr-1::DsRed]III* and TOL12 (*aatIs12[unc-47p::Arch::GFP, myo-2p::mCherry*]) by integrating the extrachromosomal arrays in *jqEx456 [Pmyo-3::R-CaMP2; Punc-25::G-CaMP6; Punc-47::ChR2::P2A::DsRed2; Podr-1::DsRed]* and OKA074 (*ncEx2351 [unc-47p::Arch::gfp, myo-2p::mCherry]*) into the animals' genome via UV irradiation methods, respectively (Okazaki et al., 2012; Inoue et al., 2015); then we crossed the integrated strains with wild type N2 for at least 5 generations and screened for the homozygous (Ahringer, 2006). We generated TOL15 by crossing TOL14 (*aatIs4 [myo3p::nls::RCaMP2]V*) and ZW495 (*zwIs132 [myo-3p::GCamp2 + lin-15(+)]*) and screening for the homozygous of *aatIs4* and *zwIs132*.

2.2.2 Free locomotion behavioral tracking

We recorded the free crawling and swimming of wild type, GABA transmission knockouts, and an optogenetic strain on NGM agar plates or in NGM buffer solution by a static multi-worm tracker. The tracker was composed of three major parts. From top to bottom: a

camera (Basler ace acA4024-29um) connected with a fixed focal length lens (C Series 5MP 35mm 2/3" fixed focal length lens, Edmund Optics) with an infrared cut-off filter (M25.5 x 0.5 Mounted IR Cut-Off Filter, Edmund Optics); a specimen stage for plates or slides; and an infrared LED light (M850L3, Thorlabs) mounted with a collimation adaptor (COP1-B-Collimation Adaptor, Thorlabs).

One day before recording, we transferred fourth larval stage (L4) animals onto new NGM plates with OP-50-1 *E. coli* bacterial lawn so that experimental animals would be first-day young adults. During tracking, at least 30 animals were freely moving on 35 mm NGM plates without a bacterial lawn or in NGM solution between a microscope slide and a coverslip, 1 mm apart. We recorded at least 9 videos by Pylon Viewer (Basler pylon Camera Software Suite) at 25 frames per second (fps) for 15 to 20 s. During video acquisition, we cropped video frame dimensions around 2,000x2,000 pixels. For crawling behavior tracking of N2 (wild type), the number of videos, animals, and data points were 12, 235, and 67,209, respectively; for VC1433, the numbers were 11, 213, and 80,407; for TM5916, the numbers were 11, 255, and 94,446; and for TM5487, the numbers were 12, 289, and 121,374. For swimming behavior tracking of N2 (wild type), the number of videos, animals, and data points were 46, 707, and 164.057, respectively; for VC1433 the numbers were 39, 778, and 247,656; for TM5916 the numbers were 38, 1014, and 316,094; and for TM5487 the numbers were 34, 668, and 293,482.

One day before behavioral tracking of the optogenetic strain TOL12, we transferred L4 animals onto NGM plates that had been freshly seeded with 50 mM all-trans-retinal (ATR) in OP-50-1 *E. coli*. To allow the animals to incorporate ATR, we kept the plates in the dark at 20°C for 24 hours. Animals fed with ATR but recorded in the dark (under

infrared LED) were tracked as one negative control group, and the same animals under lime-colored LED light that activated Archaerhodopsin-3 were the experimental group. Another negative control group were TOL12 animals not fed with ATR but kept and tracked under the same conditions as the experimental group. We used lime-colored light (M565L3, 565 nm LED with a Collimator) which is the optimal activation light of Archearhodopsin-3 (Mattis et al., 2011; Okazaki et al., 2012), with working illumination power of 10 mM/cm^2. To prevent the desensitization of TOL12 to the activation light, the maximum time of light exposure was 1 minute (Okazaki et al., 2012). The rest of the operations and software settings were the same as the behavior tracking aforementioned. For crawling behavior tracking of TOL12 without feeding ATR, the number of videos, animals, and data points were 20, 375, and 104,098, respectively; for TOL12 that were fed with ATR and tracked in the dark, the numbers were 27, 335, and 98,017; and for TOL12 that were fed with ATR and were exposed to lime light during tracking, the numbers were 26, 235, and 66,803. For swimming behavior tracking of TOL12 without feeding ATR, the number of videos, animals, and data points were 20, 326, and 81,291, respectively; for TOL12 that were fed with ATR in advance and tracked in the dark, the numbers were 22, 361, and 97,630; and for TOL12 that were fed with ATR and were exposed to lime light during tracking, the numbers were 18, 216, and 48,323.

2.2.3 Head and tail harsh touch experiments

We transferred L4 animals to new OP-50-1 *E. coli* seeded NGM plates one day before the experiment. During the experiment, we transferred animals onto 60 mm NGM plates without a bacterial lawn. We touched the head or tail of the animals using a blunt glass probe while they were crawling forward. We acquired the videos continuously with a

CMOS camera (U3CMOS14000KPA, ToupTek) and acquisition software (ToupView, https://www.touptek.com/) at 30 fps and 1,048x822 pixels greyscale during several stimulations of different animals. We further trimmed these videos into clips with one stimulation each by video editing software Premiere Pro (Adobe) or Shotcut (https://shotcut.org/).

2.2.4 Behavior analysis

Behavioral Tracking. We processed crawling and swimming tracking by Tierpsy Tracker v1.4.0, a multi-worm behavior tracker software (https://github.com/ver228/tierpsy-tracker/releases/) (Javer et al., 2018). Then we analyzed the processed results in hdf5 files by custom programs written in Matlab.

Each video had between 10 to 30 animals each assigned with an index by Tierpsy. We analyzed translocation speed and undulation frequency during forward and backward locomotion from the midbody of the animals, as well as primary wavelength and maximal amplitude. Tierpsy computes the undulation frequency using the waveform frequency from the largest peak via the Fourier transform over a time window. We collated the means of these parameters from individual animals from all the videos, then used one-way ANOVA and Tukey's multiple comparison to compare the estimated population means among strains or different conditions. We plotted scatter plots, histograms and box plots to visualize the data distribution.

We used Tierpsy Tracker v1.4.0 to extract the aforementioned kinetic parameters from trimmed video clips before and after head or tail stimulation. We calculated the means of these 4 parameters within 5 s before and 5 s after the stimulation from 9 trimmed clips in each stimulation direction of N2 strain and each GABA transmission knockout strain.

We used paired two-tail T-Test to determine the statistical difference of the parameters before and after stimulation, and one-way ANOVA and Tukey's multiple comparison for the parameters of after harsh touch to the head or tail between wild type and each GABA transmission knockout.

Linear regression in crawling and swimming behaviors. We first picked the data points where primary or secondary wavelength could be extracted by the analysis software (Tierpsy). These data points in crawling behavior were 4% to 23% of the raw data. The sample sizes of wild type, *unc-25, unc-46,* and *unc-49* during forward crawling were 11,935 (23%), 7,760 (14%), 7,773 (12%), and 5,378 (7%), respectively; those during backward crawling were 1,260 (11%), 2,319 (11%), 2,552 (10%), and 1,714 (4%), respectively. The data points in swimming behavior were and 6% to 54% of the raw data. The sample sizes of wild type, *unc-25*, *unc-46,* and *unc-49* during forward swimming were 74,948 (54%), 46,355 (26%), 69,682 (31%), and 17,015 (11%), respectively; those during backward swimming were 2,137 (14%), 6,249 (11%), 16,728 (21%), and 7,297 (6%), respectively. Then we picked the data points where the path of an undulation cycle (translocation speed × undulation cycle period) was larger than either the primary or secondary wavelength. Based on this selection criterion, we picked 27 to 54% data points for the correlation construction in crawling behavior. The sample sizes of wild type, *unc-25*, *unc-46,* and *unc-49* during forward crawling were 5,671 (48%), 2,058 (27%), 2,259 (30%), and 2,313 (43%), respectively; those during backward crawling were 686 (54%), 1,096 (47%), 1,199 (47%), and 856 (50%), respectively. We picked 0.4% to 26% of the data points in swimming behavior. The sample sizes of wild type, *unc-25, unc-46*, and *unc-49* during forward swimming were 271 (0.4%), 3,985 (14%), 2,086 (3%), and 2,965 (17%),

respectively; those during backward swimming were 138 (7%), 1,150 (18%), 975 (6%), and 1,897 (3%), respectively. Using these selected data, we calculated linear regressions between undulation frequency and translocation speed in forward and backward crawling and swimming separately.

Change in Body Length. We analyzed the body length at different times in the 9 trimmed clips in each stimulation direction of N2 strain and each of the GABA transmission knockout strains, as well as head stimulation of *vab-7* knockout animals (CB1562) and tail stimulation of *unc-4* knockout animals (CB120): before the harsh stimulation, immediately after the stimulation, as well as 0.5 s, 1 s and 2 s after the stimulation. We used 'Freehand Line' tool in ImageJ (https://imagej.nih.gov/ij/) to measure the body length of animals. We expressed body length as a percentage of pre-stimulus length and plotted the means of normalized body lengths for each strain at each time point. In addition, we used one-way ANOVA and Tukey's multiple comparison to compare the statistical difference between wild type and the other strains.

2.2.5 Calcium Imaging in Microfluidic Device

To repeatedly measure activity at particular phases of the locomotor cycle, we placed young adult animals in a waveform silicon microfluidic device with channels designed to restrict their motion to a pattern that mimics undulatory locomotion; the cycle was fixed in space and predictable at any location along the path (Figure 2.9a). The wavelength, amplitude, and width of the channel were 686.5, 322.5, and 133.5 μm, respectively. To unify the frame of reference, we arbitrarily designated the phase of a maximal dorsal bend as 90° and a maximal ventral bend as 270° (Figure 2.9a) and defined the rest of the phase positions accordingly. We presented collated recordings during forward locomotion from

motoneurons and body-wall muscle with phase (rather than time) being the common frame of reference.

We transferred the healthy fourth larval stage (L4) animals to a new OP-50-1 *E. coli* seeded plate one day before imaging. Before imaging, we added drops of methyl cellulose solution onto the face of a microfluidic device, and then transferred animals into these drops. To seal the microfluidic device, we flipped and pressed it onto an 18 mm diameter round coverslip. The transgenic animals could crawl freely inside the channels, and we manipulated their undulation frequency by changing the ambient viscosity. We used 3% and 0.5% (w/w) methyl cellulose in NGM buffer while recording calcium level changes in GABAergic motoneurons in TOL11, 1.5% (w/w) methyl cellulose to record calcium level changes in body-wall muscles in TOL15, and 3% and 0.5% (w/w) methyl cellulose to image GFP (as a negative control calcium-insensitive fluorescent protein to determine motion artifact) in GABAergic motoneurons in CZ1632.

To image and record fluorescence change of GCaMP or GFP, we used an inverted microscope (Olympus IX73) with a 40x/NA0.95 UPlanSApo objective and an sCMOS camera (Hamamatsu Orca Flash 4.0) and a solid-state excitation light source (X-Cite 120LED) with a dual-band filter set (Chroma 59022 ET-EGFP/mCherry), and a dual-camera image splitter (TwinCam, Cairn Research with a T565lpxr dichroic beam splitter). We used Micro-Manager (v1.4; https://micro-manager.org/) to acquire multiple videos of animals moving through different parts of the channel (i.e. different locomotor phases). We saved videos as separate tiff files (2,048x2,048-pixel resolution) at a frame rate of 100 fps with 10 ms exposure for animals crawling in 0.5% (w/w) methyl cellulose, and 50 fps with 20 ms exposure for animals crawling in 1.5% (w/w) and 3% (w/w) methyl cellulose. We

did not use NGM with less than 0.5% (w/w) methyl cellulose because it resulted in discontinuous and less smooth locomotion. Between acquisitions, we moved the microscope stage manually to follow animals when they moved out of view.

We used a customized Matlab program to analyze the change of the fluorescence intensity inside the identifiable body-wall muscle cells or somata of GABAergic motoneurons. For each frame, we measured the mean fluorescence intensity of the top 50% pixels within the manually traced region of interest (ROI) around the cell of interest ($F_{top50\%}$). We then calculated and subtracted the median intensity of the frame as background (F_{BG}). Finally, we demeaned the value by dividing it by the mean fluorescence signal of this cell in this video of n frames: $\Delta F/F = (F_{top50\%}-F_{BG}) / (\Sigma(F_{top50\%}-F_{BG})/n)$. Our Matlab code provides a graphical user interface (GUI) to track the cell as it moves across the field of view, following a trajectory that is set by the waveform channel, to mark the location of 90° (maximal dorsal bend) or 270° (maximal ventral bend, Figure 2.9a), and to trace $\Delta F/F$ against time or undulatory phase. We categorized traces from GABAergic motoneurons into low and high-frequency undulations of crawling inside the microfluidic channel; the undulation frequency was calculated as the fraction of the locomotor cycle traveled by the cell of interest divided by the elapsed time. Undulation frequency 0.6 Hz was the cut-off for these two categories, regardless of methyl cellulose concentration; therefore, we categorized traces from 3 DD and 4 VD motoneurons recorded in TOL11 in 3% (w/w) methyl cellulose solution as high-frequency undulation. We collated and plotted all traces of $\Delta F/F$ against the phase of each type of cell at 5° bins. We corrected the soma position of motoneurons to their neuromuscular postsynaptic position according to the published perimotor locations (Chen et al., 2006; Haspel and O'Donovan, 2011). We

removed videos or parts of videos in which the cell of interest went out of focus or if we could not positively identify it. We included data analyzed from 11 focused and cell-identifiable videos of TOL15; 11 and 9 videos of CZ1632, TOL11 in 0.5% (w/w) methyl cellulose, respectively; and 12 and 9 videos in 3% (w/w) methyl cellulose, respectively. From these videos we analyzed 27 and 24 ventral and dorsal body-wall muscles, respectively, in TOL15; 17 VD and 18 DD motoneurons in the high undulation frequency and 26 VD and 13 DD motoneurons in low frequency in CZ1632; and 32 VD and 15 DD motoneurons in the high undulation frequency and 27 VD and 14 DD motoneurons in low frequency in TOL11.

2.2.6 Computational Modeling

The computational modeling was carried out by our collaborator Jack Denham from University of Leeds in England.

Our animal model consists of a mechanical body, driven by neuromuscular activation and subject to fluid drag forces (Denham et al., 2018). We chose to focus on control circuits for only one direction of locomotion – forward locomotion, an assumption that follows from our results that suggest that the phenotypes of the GABA transmission mutant are manifested not only during a switch in direction but also during forward and backward locomotion and primarily caused by defects in the ventral nerve cord circuitry, rather than by defects in pre-motor interneurons. To this end, we adapted an existing model of forward locomotion control (Denham et al., 2018). In particular, we explored two different forms of neural control: a proprioceptively driven model and a feedforward model, mimicking CPG control (Denham et al., 2018). We subjected each model to different perturbations and explored the behavior generated in our neuromechanical framework in liquid and agar-

like conditions. Both models of neural control output a single muscle activation function acting continuously along the body, which sums the muscle activation from cholinergic B-type excitatory and GABAergic D-type inhibitory motoneurons on both sides of the body (Figure 2.2b).

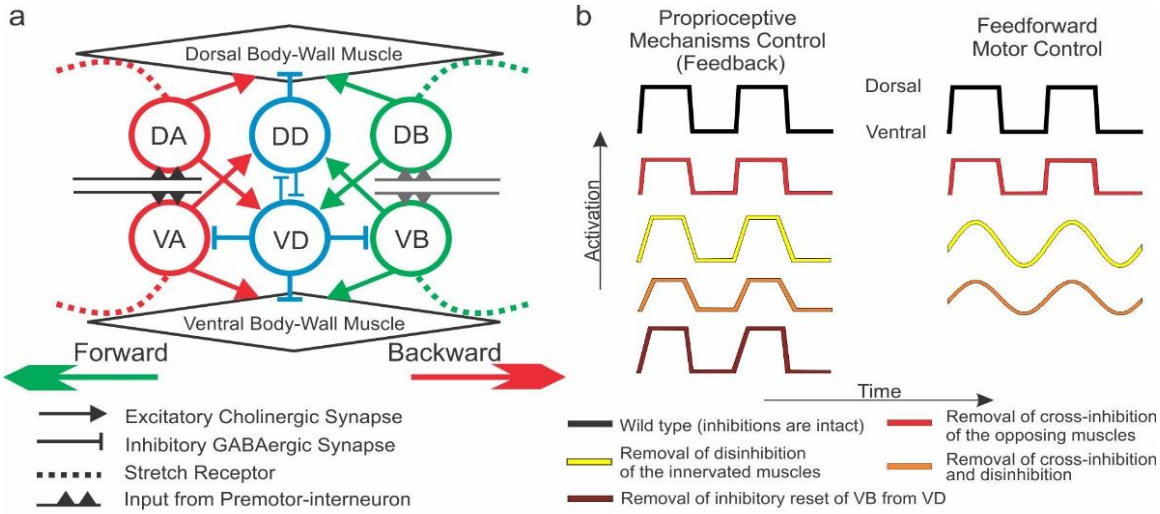

Figure 2.2 Locomotion motor circuit of the *C. elegans* ventral nerve cord has served as a basis for proprioceptive (feedback) mechanisms control computational models. (a) Schematic of locomotion motor circuit of the *C. elegans* in the ventral nerve cord, depicted as a neuromuscular unit, has served as a basis for proprioceptive (feedback) mechanisms control computational models. During forward locomotion, VB and VD (DB and DD) motoneurons innervate ventral (dorsal) muscles and VD motoneurons innervate VB motoneurons. During backward locomotion, A-type cholinergic motoneurons get involved. Stretch receptors (dash lines) transfer the proprioception of local bending and trigger the activation of VB motoneurons during forward locomotion. The non-iterative synapse contact between VD and DD motoneurons (blue thin lines) is not considered in the model. Adapted from Figure 1b of Cohen & Denham (2019). (b) Schematics of the neural activation or muscle input in the proprioceptive control model (left) and feedforward control model (right). The schematic traces indicate muscle input activation status of dorsal and ventral body-wall muscles. When inhibitions are intact in the model wild type (black), the dorsal muscle input (which increases when the trace rises) and the ventral muscle input (which increases when the trace drop down) is antiphase in square shape in proprioceptive feedback and feedforward models. When inhibition(s) is (are) removed, the amplitude or the shape of muscle input traces will be affected.

Proprioceptive Control. At every point along the body, B-type motoneurons receive proprioceptive input, which corresponds to the mean body curvature integrated over their receptive range, set here to half the body length, posteriorly to the muscle coordinate

(Denham et al., 2018). Excitatory ventral B-type (VB) and dorsal B-type (DB) motoneurons act as bistable switches. Each switch is associated with two thresholds (for switching on and off, akin to Boyle *et al.* 2012). Pre-motor activation from AVB is absorbed into the thresholds for parsimony. Following Boyle *et al*. (2012) and the published connectivity, we also assumed D-type neurons instantaneously react to excitation from B-type neurons on the opposite side of the body (Fig. 8a). Thus, if DB (or VB) is on at some point along the body, VD (or DD) is activated. In addition, we include VD to VB inhibition (Figure 2.2a), with the inhibition strength set such that the thresholds of VB and DB collapse to a single bistable switch when DB (hence also VD) is active. The corresponding reduced model, with only a single bistable switch, is presented and analyzed in depth in Denham, Ranner & Cohen (2018).

CPG control. Following Denham *et al.* (2018) and in the absence of detailed CPG mechanisms, we modeled feedforward neural activation, $A(u,t)$, at location u and time t, by a retrograde traveling sine wave that activates the muscles continuously along the body: $A(u,t) = sin\,(2\pi uL/\lambda_{\mathrm{f}} - 2\pi t/T_{\mathrm{f}})$, where L is the body length, and $\lambda_{\mathrm{f}}, T_{\mathrm{f}}$ are the wavelength and period of the undulation.

Model muscles. Under proprioceptive control, the neural circuit controls the muscles, modeled by a leaky integration equation that converts the muscle activation function at every point along the body, u, to a mechanical torque; the muscle model contains two free parameters, corresponding to a muscle time scale (100 ms in the wild type) and an amplitude or maximum curvature (10 mm^{-1} in the wild type). In the CPG-driven model, we sharpened the rise in muscle activation using a hyperbolic tangent function (Section

2.2.7), which we removed when accommodating our muscle disinhibition hypothesis (see 'Model perturbations' in Section 2.2.7).

Biomechanics. Our model of the *C. elegans* body consists of a continuous incompressible viscoelastic shell. At each point along the body, we assumed the width of the nematode's body is fixed in time, which allows us to collapse all internal and external forces onto the midline (Cohen and Ranner, 2017; Denham et al., 2018). Four free parameters modulate the biomechanical properties of the body and its interaction with the environment. Environmental forces were modeled by resistive force theory and parametrized by two drag coefficients that act to resist the motion in the normal and tangential directions. This allows us to model both Newtonian and linear viscoelastic environments in the low Reynolds number regime. Our simulations here mimic two environmental conditions: swimming in liquid (buffer solution) and crawling on agar. The passive body is parametrized by Young's modulus (the effective elastic resistance to bending or body stiffness, set to 100 kPa for the wild type), and an internal viscosity (the body damping in response to bending) which we neglect for simplicity. The model equations balance internal and external forces and torques subject to mass conservation within the nematode's body (Cohen and Ranner, 2017).

Model perturbations:

1. Eliminating cross-inhibition of opposing body wall muscles (Hypothesis 1). To implement this hypothesis, we eliminated all muscle inhibition, leaving neural inhibition intact. In our model, the muscle forcing on both sides of the body is combined into a single muscle activation function acting along the midline of the body. Therefore, the elimination of muscle cross-inhibition by D-type neurons is equivalent to decreasing the effective

excitation by the actively contracting side of the body. Unless otherwise stated, we set the strength of the muscle inhibition by D-type neurons to 20% that of the muscle excitation by B-type neurons (estimating that animals with maximal shrinking are at most 20% shorter than in the fully relaxed state).

2. Eliminating disinhibition of innervated body wall muscles (Hypothesis 2). This could be modeled by a more complex nonlinear muscle model. Alternatively, using our linear muscle model, we assumed a faster muscle response following phasic release from inhibition. In the proprioceptive model, this is achieved by reducing the muscle time scale and therefore crudely models the faster response by alternating sides of the body. Unless otherwise stated, we increased the muscle time scale by 20% to mimic the effect of eliminating the disinhibitory muscle response. In the CPG-driven wild type model, we sharpen the increase and decrease in our periodic muscle activation using a hyperbolic tangent function, $\beta_0 \tanh\big(\alpha A(u,t)\big) \;/ \tanh(\alpha)$, keeping the amplitude β_0 unchanged. The tanh function is omitted in the default perturbation or gradually suppressed (through a modulation of α) in the parameter sweeps.

3. Eliminating inhibitory reset of VB by VD (Hypothesis 3). In our proprioceptive control model, elimination of neural inhibition implies that VB neurons are not inhibited when DB neurons are active, but that muscle inhibition remains intact. Thus, we modeled it by a constant positive offset applied to both thresholds of the VB bistable switch. Since our simplistic feedforward model does not take into account individual motoneurons, we only explore this hypothesis in the feedback model.

In coordinated locomotion, the undulation frequency (the reciprocal of the period of undulation) was computed from curvature kymograms. For a given point along the body,

the period was defined as the mean time interval between positive (increasing) zero crossings of the body curvature.

2.2.7 Computational models, equations, and parameters

The mechanical component of the model, described in 'Body mechanics', is actuated by a spatially continuous neural activation function $A(u,t)$, where $u \in [0,1]$ represents the distance along the midline of the worm from head ($u = 0$) to tail ($u = 1$), and t is time. Two neural activation functions are used: the first mimics a central pattern generated (CPG) traveling wave, which drives the muscles in a purely feedforward paradigm. The second function models neural activation that is driven by proprioceptive feedback. Under CPG control, the activation function takes the form of a unit amplitude traveling sine wave with period T_{f} and wavelength λ_{f},

$$A(u,t) = \sin(2\pi uL/\lambda_{\mathrm{f}} - 2\pi t/T_{\mathrm{f}}) . \quad (1)$$

Under proprioceptively driven control, we introduce spatially continuous binary motoneurons with states in $\{0,1\}$. VB and DB motoneuron states are denoted $V_{\mathrm{VB}}(u,t)$ and $V_{\mathrm{DB}}(u,t)$. We assume that D-type motor neurons respond instantaneously to excitation from B-type motoneurons on the opposite side of the body, so V_{VB} (V_{DB}) $= 1$ implies that DD (VD) is also activated. We model B-type motor neurons as bistable elements, following Boyle *et al.* (2012) and inspired by electrophysiological recordings of bistable RMD head motor neurons (Mellem et al., 2008). The bistability is implemented as distinct on and off thresholds on the ventral (V) and dorsal (D) sides, $\theta_{k,\mathrm{ON}}$ and $\theta_{k,\mathrm{OFF}}$ ($k \in \{\mathrm{V},\mathrm{D}\}$), which need to be crossed for a neuronal state change of VB or DB to occur. Both VB and DB receive the same constant input from the AVB premotor interneurons, I_{AVB}. A

proprioceptive input, $I_\kappa(u,t)$, is defined for the dorsal side such that the input on the ventral side at the same position and time is $-I_\kappa(u,t)$. In addition, VB is inhibited by VD (when DB is active), $I_{\mathrm{VD}}(u,t) = w\, V_{\mathrm{VD}}(u,t)$. State switches depend on the following relations:

$$\begin{aligned} V_{\mathrm{DB}}(u,t) &\to 1 \quad \text{if } I_{\mathrm{AVB}} + I_\kappa > \theta_{\mathrm{D,ON}}\,, \\ V_{\mathrm{VB}}(u,t) &\to 1 \quad \text{if } I_{\mathrm{AVB}} - I_{\mathrm{VD}} + I_\kappa > \theta_{\mathrm{V,ON}}\,, \\ V_{\mathrm{DB}}(u,t) &\to 0 \quad \text{if } I_{\mathrm{AVB}} + I_\kappa < \theta_{D,OFF}\,, \\ V_{\mathrm{VB}}(u,t) &\to 0 \quad \text{if } I_{\mathrm{AVB}} - I_{\mathrm{VD}} + I_\kappa < \theta_{\mathrm{V,OFF}}\,. \end{aligned} \tag{2}$$

In practice, constant values such as I_{AVB} can be absorbed into the threshold. The state of a neuron is driven by changes in proprioceptive input current $I_\kappa(u,t)$ which is defined here as the mean of the body curvature $\kappa(u,t)$ over a specified proprioceptive range $\Delta(u)$, represented as a fraction of the body length:

$$I_\kappa(u) = \int_u^{u+\Delta(u)} \kappa(u')|\boldsymbol{x}_u(u')|du' \int_u^{u+\Delta(u)} |\boldsymbol{x}_u(u')|du', \tag{3}$$

where $\boldsymbol{x}$ denotes a coordinate of a point along the body in the lab frame and the subscript u denotes a partial derivative. This encoding of body posture is fed back to the motoneurons, thus closing the brain-body-environment loop. The above input current represents the effective stretch of the dorsal side of the body at that time. Here, we keep $\Delta(u) < 0$ which by our convention corresponds to a strictly posterior proprioceptive range, though $\Delta(u) > 0$, and combinations of anterior and posterior range are also possible (Denham et al., 2018). For u sufficiently close to the tail, the proprioceptive range terminates at the tail, therefore decreasing linearly with u. Hence the denominator in

Equation (3) normalizes by this range, effectively making posterior neurons more sensitive to stretch 'density' to compensate for the reduced range. Our mechanical model uses a midline parametrization to determine the internal forces driving body curvature. Therefore, our neural activation function sums the contributions of adjacent neurons from both sides of the body, weighted by excitatory and inhibitory neuromuscular junction weights, ${w^{\mathrm{exc}}}_{\mathrm{NMJ}}$, ${w^{\mathrm{inh}}}_{\mathrm{NMJ}}$

$$A(u) = {w^{\mathrm{exc}}}_{\mathrm{NMJ}}\big(V_{\mathrm{DB}}(u) - V_{\mathrm{VB}}(u)\big) - {w^{\mathrm{inh}}}_{\mathrm{NMJ}}\big(V_{\mathrm{DD}}(u) - V_{\mathrm{VD}}(u)\big) \tag{4}$$

to define our activation $A(u)$, which then drives the muscle via Equation (5).

Muscles:

For simplicity, the model assumes that the body wall muscles respond linearly to input over timescale τ_{m} (100 ms, Table 2.1), and are also spatially continuous along the body. Under proprioceptive control, muscles receive current input from ventral and dorsal motor neurons and output the muscle activation, $\beta(u,t)$, acting about the animal's midline,

$$\tau_{\mathrm{m}}\frac{d\beta}{dt} = -\beta + \beta_0 A, \tag{5}$$

where β is a preferred curvature (akin to a rest length of a spring) and β_0 sets the curvature amplitude (Equation (6)). In the case of CPG control, and in order to accommodate hypothesis 2, we assume that the muscle activation in the wild type polarizes more sharply than in the GABA mutants. We therefore set the muscle activation to

$$\beta(u,t) = \beta_0 \tanh\big(\alpha A(u,t)\big) \,/\, \tanh(\alpha) \tag{6}$$

with the steepness α corresponding to the strength of the disinhibition and where the denominator normalizes the amplitude of the muscle activation.

Body mechanics:

A detailed description of the body mechanics is given in Cohen and Ranner (2017). The worm's body is represented by a thin, incompressible viscoelastic shell of fixed length, subject to internal pressure and external forces. The mechanical properties of the body are defined by its effective Young's modulus, E, and second moment of area I_2, in addition to an internal viscosity which we neglect. The interaction of the body with the external fluid environment is modeled using resistive force theory in which tangential and normal drag coefficients (K_τ and K_v) act against the cuticle in the respective directions (denoted by unit vectors $\boldsymbol{\tau}$ and $\boldsymbol{\nu}$)

$$\boldsymbol{F}_{\text{env}} = K_v v_v \boldsymbol{\nu} + K_\tau v_\tau \boldsymbol{\tau}. \tag{7}$$

This approximation is sufficient to reproduce the experimentally observed gait transition (Berri et al., 2009; Fang-Yen et al., 2010) under feedback control (Boyle et al., 2012; Denham et al., 2018). To produce a body bend, midline curvature $\kappa(u,t)$ is driven by the muscle activation $\beta(u,t)$ (here, a torque that is represented as a preferred body curvature) which in turn is driven by activation $A(u,t)$ in either the CPG or proprioceptive sense. By convention, positive and negative $\beta(u,t)$ correspond to dorsal and ventral excitation, respectively. The timescale of undulations depends on both the elasticity of the body E and the resistivity of the environment (Cohen and Ranner, 2017; Denham et al., 2018). The balance of forces is summarized as follows:

$$\boldsymbol{F}_{\text{env}} - \frac{1}{|\boldsymbol{x}_u|}(p\boldsymbol{\tau})_u + \frac{1}{|\boldsymbol{x}_u|}\left(\frac{1}{|\boldsymbol{x}_u|} E I_2 (\kappa - \beta)_u \boldsymbol{\nu}\right)_u = 0, \tag{8}$$

where p represents the worm's internal pressure which acts as a line tension along the midline of the worm. Zero force and zero torque are enforced at the boundaries, such that $\beta(u,t) = \kappa(u,t)$ at both the head and tail ends of the body ($u = 0,1$).

Table 2.1 Default Parameters of Both Computational Models

	Description	Parameter	Value
Body geometry	Body length	L	1 mm
	Cuticle thickness	r_{cuticle}	0.5 μm
	Maximum body radius	R	40 μm
Muscles	Muscle timescale (feedback model)	τ_{m}	0.1 s
		α	3.0
	Muscle disinhibition (CPG model)	β_0	10 mm^{-1}
	Curvature amplitude		
Mechanics	Young's Modulus	E	10^5 Pa
	Tangential drag coefficient	$K_{\tau,\text{water}}$	$3.3x10^{-3}kgm^{-1}s^{-1}$
		$K_{\tau,\text{agar}}$	3.2 $kgm^{-1}s^{-1}$
	Normal drag coefficient	$K_{v,\text{water}}$	$5.2x10^{-3}kgm^{-1}s^{-1}$
		$K_{v,\text{agar}}$	128 $kgm^{-1}s^{-1}$
CPG (feedforward) control	Undulation wavelength (water)	λ_{f}	0.6 mm
	Undulation wavelength (agar)	λ_{f}	1.6 mm
	Undulation period (water)	T_{f}	0.6 s
	Undulation period (agar)	T_{f}	2.0 s
Proprioceptive control	Ventral ON/dorsal OFF thresholds	$\theta_{\text{V,ON}}$, $\theta_{\text{D,OFF}}$	3.0
		$\theta_{\text{V,OFF}}$ $\theta_{\text{D,ON}}$	-3.0
	Ventral OFF/dorsal ON threshold	δ	0.5
	Proprioceptive range	$w^{\text{exc}}{}_{\text{NMJ}}$	0.8
	VB, DB NMJ weight	$w^{\text{inh}}{}_{\text{NMJ}}$	0.2
	VD, DD NMJ weight	w	0.2
	VD → VB inhibitory weight		

Model perturbations:

Based on the experimental results, we explore three hypotheses to explain the role of inhibition in sustaining high-frequency locomotion; each of these hypotheses in our computational models are tested separately under purely feedforward (CPG) and purely feedback (proprioceptive) neural control.

Hypothesis 1. Cross inhibition of the opposing body wall muscles increases the dorsoventral difference in muscle activation. Losing this inhibition effectively results in reduced activation on the bending side. In the CPG-driven model, we implement this change with a multiplicative constant applied to our preferred curvature:

$$\beta(u,t) \rightarrow c\beta(u,t), \text{ where } c = 0.8,$$

(with $c = 1$ in the wild type). In the absence of cross muscle inhibition, $c < 1$ indicates that the muscle on the stretched side remains partially activated (Petzold et al., 2011; Boyle et al., 2012). In our proprioceptively driven model, we set the neuromuscular junctions of B- and D-type motoneurons such that eliminating muscle inhibition gives an identical outcome.

Hypothesis 2. Disinhibition of the body wall muscles should increase muscle force, immediately after the muscle inhibition is released, resulting in a sharper upstroke in muscle activation on the contracting (bending) side of the body. We distinguish between CPG and proprioceptively driven control as follows:

CPG control: In the wild type model worm, we enforce a sharpness in the upstroke of muscle drive using a sigmoidal muscle activation function, which we neglect in disinhibition deficient worms:

$$\beta^{\mathrm{hyp2}}(u,t) = A(u,t) = \sin(2\pi uL/\lambda_{\mathrm{f}} - 2\pi t/T_{\mathrm{f}}) .$$

Proprioceptive control: We assume disinhibition deficient worms have a slower muscle timescale on the contracting side of the body. Due to the alternation of muscle

contraction, we model the combined dorsoventral muscle activation, $\beta^{\mathrm{hyp2}}(u,t)$, with an overall slower effective muscle timescale, ${\tau^{\mathrm{hyp2}}}_{\mathrm{m}}$, yielding

$${\tau^{\mathrm{hyp2}}}_{\mathrm{m}}\frac{d\beta(u,t)}{dt} = -\beta(u,t) + \beta_0 A(u,t), \text{ where } {\tau^{\mathrm{hyp2}}}_{\mathrm{m}} = 1.2\tau_{\mathrm{m}} .$$

Hypothesis 3. Inhibitory reset of VA and VB by VD is required for rapid swimming. Boyle *et al.* (2012) hypothesized that worms lacking neural inhibition will fail to undulate in liquid-like environments, in which wild type worms undulate at higher frequency. As this hypothesis depends explicitly on the GABAergic neural circuit, we do not implement this hypothesis in our ad hoc CPG model. In our proprioceptive control model, VB activation depends on the state of DB due to the DB→VD →VB connectivity. To model defects corresponding to this hypothesis, we set $I_{\mathrm{VD}} = 0$ at all times. Unless otherwise stated, we only knock out one form of inhibition in the model in a given simulation.

2.3 Results

2.3.1 Both wild type and the GABA transmission mutants shrank in response to harsh touch to the head or tail

C. elegans mutants defective in GABA transmission are known as *'shrinkers'* because of their distinct decrease in body length in response to a harsh touch to the head (McIntire et al., 1993a; McIntire et al., 1993b; Schuske et al., 2004), whereas wild type animals respond with rapid backward motion. Because this phenotype has been described as a defect in backward locomotion, we first looked at the shrinking response of wild type and GABA transmission mutant animals to harsh touch to the head that induces rapid backward undulation in wild type animals, as well as the response to the tail touch to study the

association of shrinking response to forward locomotion. We chose three knockout mutant strains in which hundreds to thousands of DNA base pairs had been deleted in the genes encoding the GABA synthesis enzyme glutamic acid decarboxylase (GAD, *unc-25*, VC1433), vesicular transporter (*unc-46*, TM5916), and ionotropic GABA receptor (*unc-49*, TM5487), and compared them to the laboratory reference strain (wild type, N2). We found the shrinking response was common in wild type and mutant animals following head or tail stimulation (Figure 2.3a). To quantify the shrinking response of wild type and the GABA transmission knockout animals, we measured the change in body length in 9 stimulation experiments for each strain and stimulation direction at different times (before, immediately after, 0.5 s, and 2 s after stimuli), and normalized the body length to their value before stimuli (Figure 2.4a, Table 2.2). Immediately after a harsh touch to the head or tail, both wild type and the GABA transmission knockout animals decreased their body length, while wild type animals shrank less: the body length of wild type animals reduced to 94% ± 2% and 95% ± 3% (mean ± SD), respectively, while the body length of GABA transmission knockouts reduced to 90-92% ± 2-4% (mean ± SD). In addition, wild type recovered to their pre-stimulus body length faster. At 2 s after the head and tail stimulation, the body length of wild type reached to 98-99% ± 2-4% (mean ± SD) of the pre-stimulus body length, while that of the mutants was 92-97% ± 4-6% (mean ± SD). Moreover, GABA transmission knockouts occasionally exhibited voluntarily shrinking without stimulation (Figure 2.3f).

A possible explanation to the coactivation of dorsoventral body-wall muscles that causes body shrinkage in response to harsh touch is simultaneous activation of all A- and B type cholinergic motoneurons by pre-motor interneurons that are associated with forward

and backward locomotion (activating DA and VA during backward, and DB and VB during forward (Haspel et al., 2010). This hypothesis requires a short temporal overlap between the activities of the two groups of cholinergic motoneurons. To test this hypothesis, we tested the shrinking response of *vab-7* mutant animals (CB1562), in which DB motoneurons differentiate as DA (Esmaeili et al., 2002), after harsh touch to the head and the shrinking response of *unc-4* mutant animals (CB120), in which DA and VA motoneurons differentiate as DB and VB (Miller et al., 1992; Miller and Niemeyer, 1995), after harsh touch to the tail. Both mutant strains have very uncoordinated locomotion in one direction (i.e. forward for *vab-7* and backward for *unc-4*) and we tested whether they shrink to a stimulus that induces rapid locomotion to the seemingly unaffected direction. We measured the body length before, immediately after, 0.5 s, 1 s, and 2 s after stimuli. *vab-7* animals reduced their body length; not statistically different from those of wild type (One-way ANOVA with Tukey test, $p=0.124 \sim 0.975$ pairwise comparison to wild type; percent of pre-stimulus). The reduction of the normalized body length of *unc-4* was not different from those of wild type either (One-way ANOVA with Tukey test, $p=0.892 \sim 0.999$ pairwise comparison to wild type; Figure 2.4a, Table 2.2). These results disapproved the aforementioned explanation, suggesting that the shrinking phenotype is localized within the motor circuit and not associated with direction change.

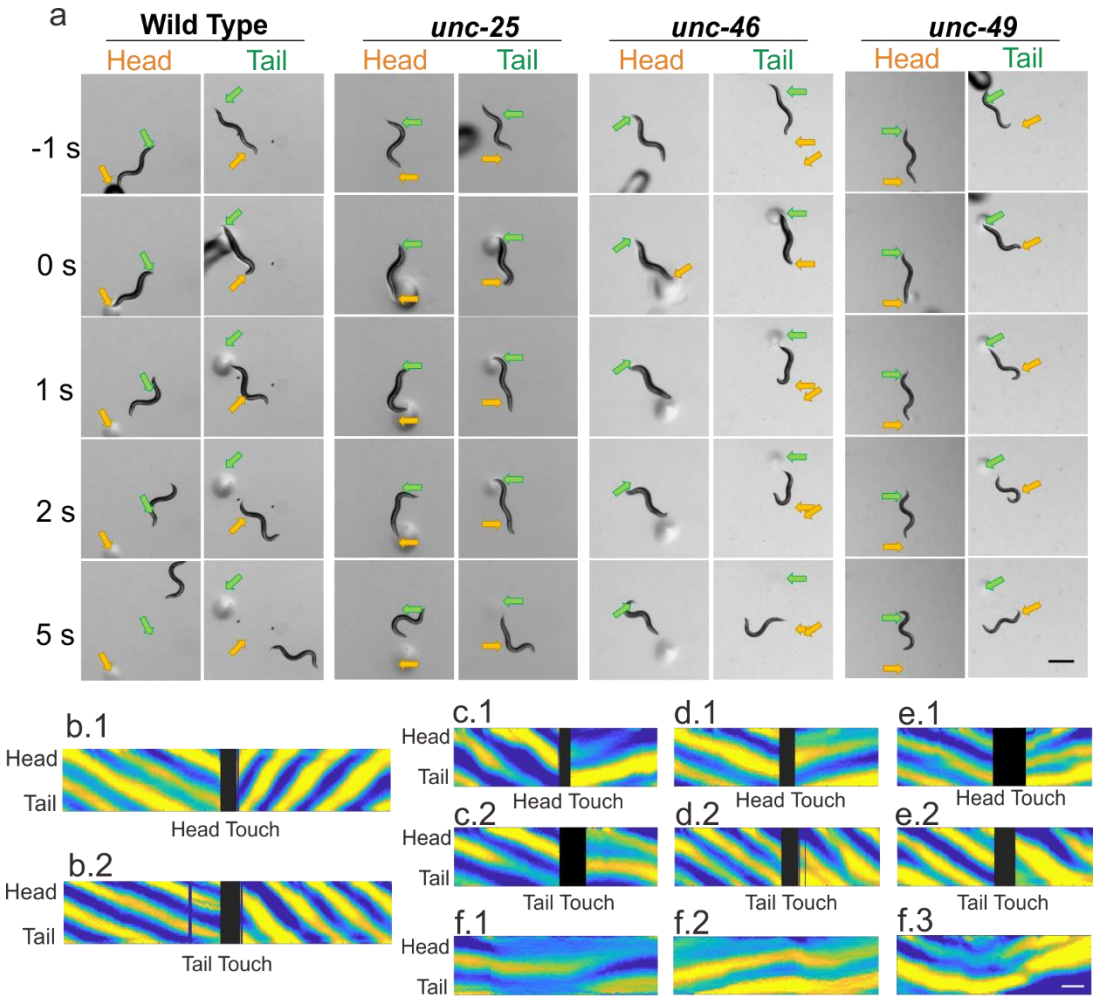

Figure 2.3 Wild type and GABA transmission knockouts shrank after harsh touch to the head or tail, while only wild type escaped rapidly. (a) While moving forward, animals were touched by a blunt glass probe as a harsh stimulation to the head (yellow arrow) or tail (green arrow). Wild type animals briefly shrank immediately after stimulation (0 s compare to -1 s before stimulation) and rapidly moved away from the stimuli, while GABA transmission knockouts shrank for a longer time and moved away slowly. Note that by 5 s all animals had moved away from the stimuli. Scale bar = 0.5 mm. Dark and circular shadows were the glass probe and the marks it left on agar. After harsh stimulation, wild type animals (b) increased undulation frequency to escape backwards (b.1) or forwards (b.2), while the three GABA transmission mutants – *unc-25* (c), *unc-46* (d) and *unc-49* (e) – moved away from the stimulus but decreased undulation frequency. Moreover, there was a period in which the body posture of these mutants did not change after the stimulation (c-e). The mutants, *unc-25* (f.1), *unc-46* (f.2) and *unc-49* (f.3), occasionally shrank without stimulation. Yellow and blue shaded area in b-f represent dorsoventral curvature (y axis is the length of animal from the head on the top to the tail), along time (x axis, scale bar is 1 s); black blocks, indicating the harsh touch stimulation, were caused by probe.

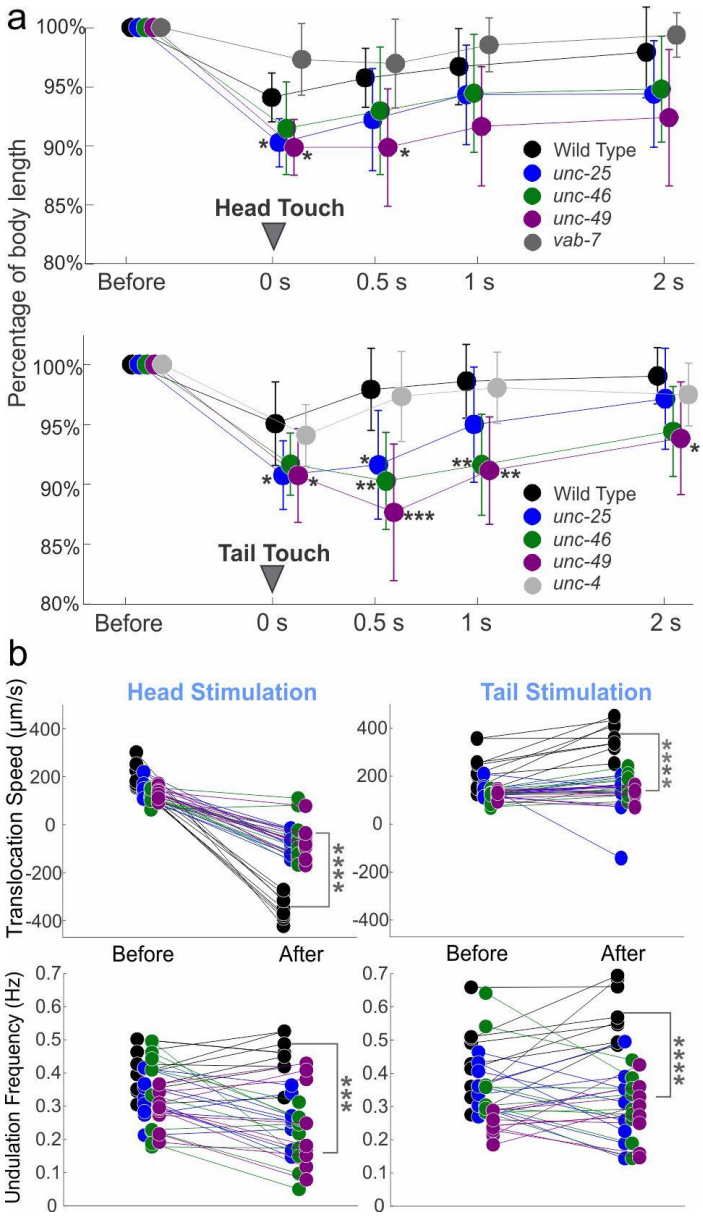

Figure 2.4 Both wild type and GABA transmission knockout animals shrank after harsh stimuli; wild type animals shrank less, recovered sooner, and crawled away more rapidly. Statistics, one-way ANOVA with Tukey's pairwise comparison to wild type, * p <0.05, ** p<0.01, *** p<0.001, **** p<0.0001. Black circles: wild type, blue: *unc-25*, green: *unc-46*, and purple: *unc-49*. (a) Wild type and GABA transmission knockout animals decreased their body length after harsh stimuli to the head or tail (0 s). Compared to wild type, GABA transmission mutants decreased their body length more and recovered more slowly (0.5, 1, and 2 s after stimuli). The body length change of *vab-7* and *unc-4* were not statistically different from that of wild type. Body length is normalized to pre-stimulus value for each animal. See Table 2-1for details. (b) Wild type animals moved with higher mean undulation frequency and mean translocation speed during 5 s post-stimulus compared to the 5 s pre-stimulus, while the mutants could not. Two *unc-46* mutant animals did not change locomotion direction after harsh head touch, neither did one *unc-25* mutant animal after harsh tail touch. See Tables 2. 2 and 2.3 for statistic details

Table 2.2 Body Length Change in The Harsh Touch Experiments

		0 s			0.5 s			1 s			2 s		
		Mean ± SD	One-way ANOVA	p value (Tukey test)	Mean ± SD	One-way ANOVA	p value (Tukey test)	Mean ± SD	One-way ANOVA	p value (Tukey test)	Mean ± SD	One-way ANOVA	p value (Tukey test)
Head Stimulation	Wild Type	94±2%	F(4,40) = 11.2, p < 0.0001	Comparison Reference	96±2%	F(4,40) = 3.91, p =0.009	Comparison Reference	97±3%	F(4,40) = 3.68, p =0.0121	Comparison Reference	98±4%	F(4,40) = 3.91, p =0.0091	Comparison Reference
	unc-25	90±2%		0.0432	92±4%		0.4210	94±4%		0.7327	94±5%		0.4168
	unc-46	91±4%		0.2850	93±5%		0.6454	94±5%		0.7698	95±4%		0.5429
	unc-49	90±2%		0.0202	90±5%		0.0447	92±5%		0.0853	92±6%		0.0666
	vab-7	97±3%		0.1236	97±4%		0.9749	99±2%		0.8738	99±2%		0.9496
Tail Stimulation	Wild Type	95±3%	F(4,40) = 3.73, p =0.0114	Comparison Reference	98±3%	F(4,40) = 9.54, p<0.0001	Comparison Reference	99±3%	F(4,40) = 6.89, p =0.0003	Comparison Reference	99±2%	F(4,40) = 3.27, p =0.0207	Comparison Reference
	unc-25	91±3%		0.0402	92±5%		0.0304	95±5%		0.3241	97±4%		0.8014
	unc-46	92±3%		0.1607	90±4%		0.0053	92±4%		0.0053	93±4%		0.0719
	unc-49	91±4%		0.0392	88±6%		0.0001	91±4%		0.0025	94±5%		0.0324
	unc-4	94±2%		0.9631	97±4%		0.9985	98±3%		0.9984	97±3%		0.8921

2.3.2 GABA transmission knockouts failed to escape rapidly as wild type after harsh touch stimulation

After harsh touch stimulation, wild type animals were able to escape at high frequency and translocation speed, while the mutants moved away slowly (Figure 2.3a, note location at 5 s). We measured translocation speed and midbody undulation frequency, as well as maximal amplitude and primary wavelength, within 5 seconds before and 5 seconds after stimulation (n=9 video clips for each strain and stimulation direction, Figure 2.4b, Table 2.3). After harsh touch to the head or tail, wild type animals escaped with significantly higher translocation speed and undulation frequency, while GABA transmission knockouts had lower mean translocation speed except for *unc-46* and *unc-49* after harsh tail touch, and lower mean undulation frequency except for *unc-49* after harsh tail touch (Table 2.3). Compared to the locomotion within 5 s after harsh head or tail touch of wild type, all the GABA transmission knockouts had significant lower translocation speed (One-way ANOVA with Tukey test, $p < 0.0001$ pairwise comparison to wild type) and undulation frequency ($p < 0.05$ pairwise comparison to wild type; Figure 2.4b, Table 2.3). Wild type and GABA transmission knockouts exhibited larger amplitude, but unchanged wavelength after stimulation (except for *unc-46* after tail harsh touch, Figure 2.4b, Table 2.3). Note that to quantify the shrinking response we chose assays in which animals (including mutants) produced sinusoidal crawling before harsh touch. A possible bias from this selection will underestimate the actual difference among strains.

Table 2.3 Locomotion Differences Before and After Stimulation Across Strains

			Head Stimulation			Tail Stimulation		
			Mean*	Std	p**	mean*	Std	p**
Wild Type	Speed (μm/s)	Before	199.334	50.548	<0.001	244.124	75.965	0.003
		After	-345.25	50.529		366.445	61.517	
	Frequency (Hz)	Before	0.388	0.068	0.001	0.443	0.116	0.006
		After	0.453	0.062		0.579	0.084	
	Amplitude (μm)	Before	182.971	29.884	<0.001	184.278	35.265	0.004
		After	322.975	40.708		259.725	60.174	
	Wavelength (μm)	Before	661.575	109.114	0.165	629.363	88.076	0.707
		After	629.909	49.992		615.431	45.689	
unc-25	Speed (μm/s)	Before	142.652	36.174	0.014	150.541	29.416	0.694
		After	-76.18	47.55		130.925	100.75	
	Frequency (Hz)	Before	0.328	0.067	0.026	0.361	0.065	0.186
		After	0.255	0.07		0.304	0.111	
	Amplitude (μm)	Before	166.234	55.398	0.046	153.132	42.383	<0.001
		After	194.091	53.936		213.855	39.218	
	Wavelength (μm)	Before	547.147	39.504	0.379	600.631	45.547	0.981
		After	605.477	202.029		601.13	54.042	
unc-46	Speed (μm/s)	Before	116.991	27.016	0.158	123.233	28.341	0.002
		After	-54.049	95.754		171.188	43.531	
	Frequency (Hz)	Before	0.329	0.127	0.006	0.376	0.129	0.036
		After	0.197	0.086		0.299	0.094	
	Amplitude (μm)	Before	174.184	46.422	0.026	166.694	32.505	0.001
		After	223.996	53.294		229.486	39.217	
	Wavelength (μm)	Before	667.955	80.193	0.086	683.16	97.215	0.011
		After	584.359	76.685		572.421	70.72	
unc-49	Speed (μm/s)	Before	139.75	28.219	0.005	139.49	15.209	0.874
		After	-67.461	81.895		142.927	31.768	
	Frequency (Hz)	Before	0.293	0.061	0.162	0.245	0.041	0.266
		After	0.249	0.129		0.329	0.059	
	Amplitude (μm)	Before	176.482	40.852	0.167	181.484	49.939	0.062
		After	216.915	30.38		219.749	48.219	
	Wavelength (μm)	Before	584.593	87.558	0.549	562.112	47.307	0.908
		After	577.666	121.794		600.432	113.857	

* Estimated population mean; ** p-value, paired two-tail T-Test.

2.3.3 Defect in GABA transmission resulted in slow locomotion during free crawling and swimming

Early descriptions of the locomotion defect of GABA transmission mutant and animals in which most GABAergic motoneurons have been laser ablated emphasize the absence of backward locomotion (McIntire et al., 1993b). Yet, we noted that shrinking occurs regardless of the direction animals were trying to take and that GABA transmission knockout strains seem to slowly crawl in both directions and their locomotion was more impaired during swimming in liquid. We recorded and compared unstimulated free crawling and swimming behaviors of wild type and GABA transmission knockout strains, as well as an optogenetic strain (TOL12) in which GABAergic motoneurons can be inactivated acutely by light.

Crawling on NGM agar surface without bacterial lawn, GABA transmission knockout strains crawled slowly. The distribution of translocation speeds and frequencies of GABA transmission knockouts during forward and backward crawling were significantly different from those of wild type (KS test, $p < 0.0001$, for *unc-25, unc-46,* and *unc-49*). The wild type distribution of undulation frequency was bimodal for both forward and backward crawling. The undulation frequency during forward crawling fits two Gaussian distributions: one distribution with 0.84 mixing proportion has a mean value of 0.47 Hz, and the other with 0.16 mixing proportion has a mean value of 0.17 Hz (Figure 2.5a). GABA transmission knockout strains crawled at lower mean translocation speed and mean undulation frequency compared to wild type (Figure 2.5, Table 2.4). Only the mean undulation frequency of VC1433 during forward crawling was not significantly lower than that of wild type. Maximal amplitude of GABA transmission knockouts was significantly

smaller than those of wild type, as well as primary wavelength of GABA transmission knockouts compared to that of wild type.

During swimming *C. elegans* undulate at higher frequency, wavelength, and amplitude (Karbowski et al., 2006; Pierce-Shimomura et al., 2008; Butler et al., 2015). If the absence of GABA transmission impairs fast undulations, it should have a more severe effect on swimming behavior with a more distinct difference between mutants and wild type. We, therefore, recorded the swimming behavior of wild type and GABA transmission knockouts in NGM buffer. Wild type animals alternated dorsal and ventral bends evenly with bigger undulation amplitude and wavelength than during crawling (Figure 2.6a1). In comparison, GABA transmission knockouts undulated at lower frequency with dorsoventral body alternation that was not as symmetric as wild type (Figure 2.6a2). The distribution of translocation speeds and frequencies of GABA transmission knockouts during forward and backward swimming are significantly different from those of wild type (KS test, $p<0.001$; for *unc-25*, *unc-46*, and *unc-49*; Figure 2.6b).

Indeed, GABA transmission knockout strains swam at significantly lower translocation speed and undulation frequency in the compared to wild type (Figure 2.6bc, Table 2.4). Maximal amplitudes of GABA transmission knockouts were significantly smaller than those of wild type, as well as primary wavelength of GABA transmission knockouts compared to that of wild type.

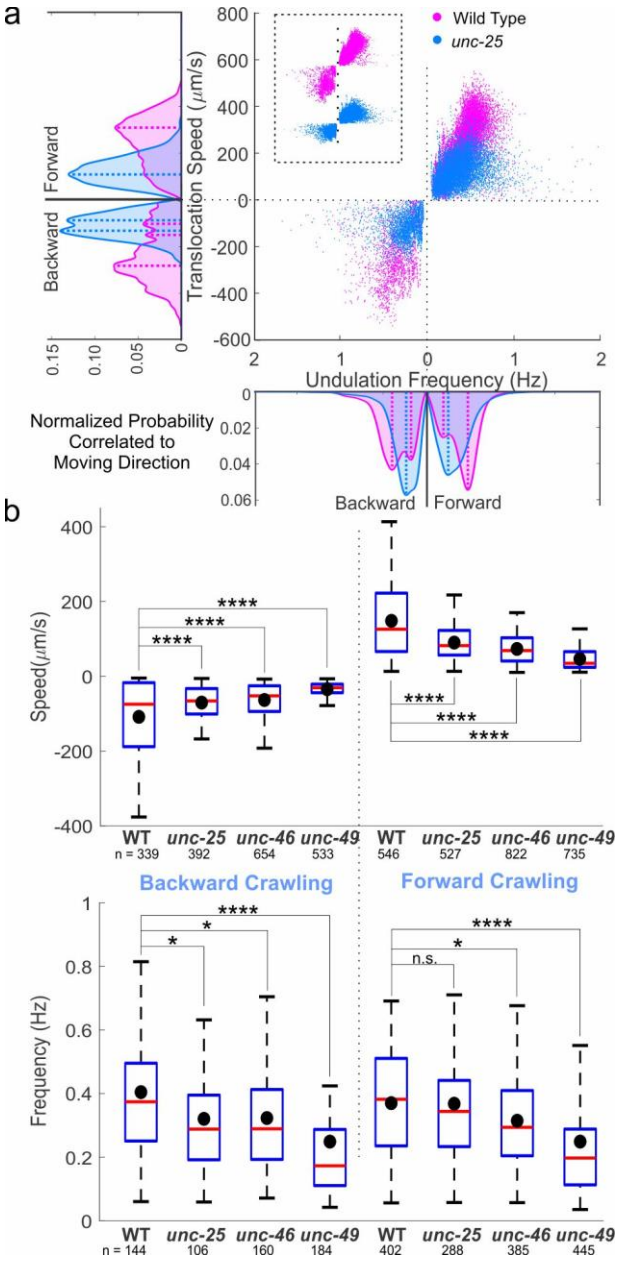

Figure 2.5 GABA transmission mutants crawled slower than wild type. (a) *unc-25* knockout animals crawled on agar surface with lower translocation speed and undulation frequency than wild type. Negative translocation speed and undulation frequency left of 0 represent backward locomotion. Area plots are probability occurrence within each direction either forward or backward. The dashed lines indicate the main peaks in the area plots. (b) Translocation speeds of all the GABA transmission knockouts were significantly lower than that of wild type (WT) during forward and backward crawling. The undulation frequencies of GABA transmission knockouts were significantly lower than that of wild type, except for that of *unc-25* during forward crawling. Blue boxes range the first to third quartiles of each dataset, red lines are medians, black dots are mean values, the bottom and top black whisker are the minimum and the maximum, respectively, excluding outliers (beyond 1.5-fold interquartile range from middle 50% data). ANOVA with Tukey pairwise comparison to wild type, n.s. $p>0.05$, * $p<0.05$, *** $p<0.001$, **** $p<0.0001$. See Table 2.4 for details.

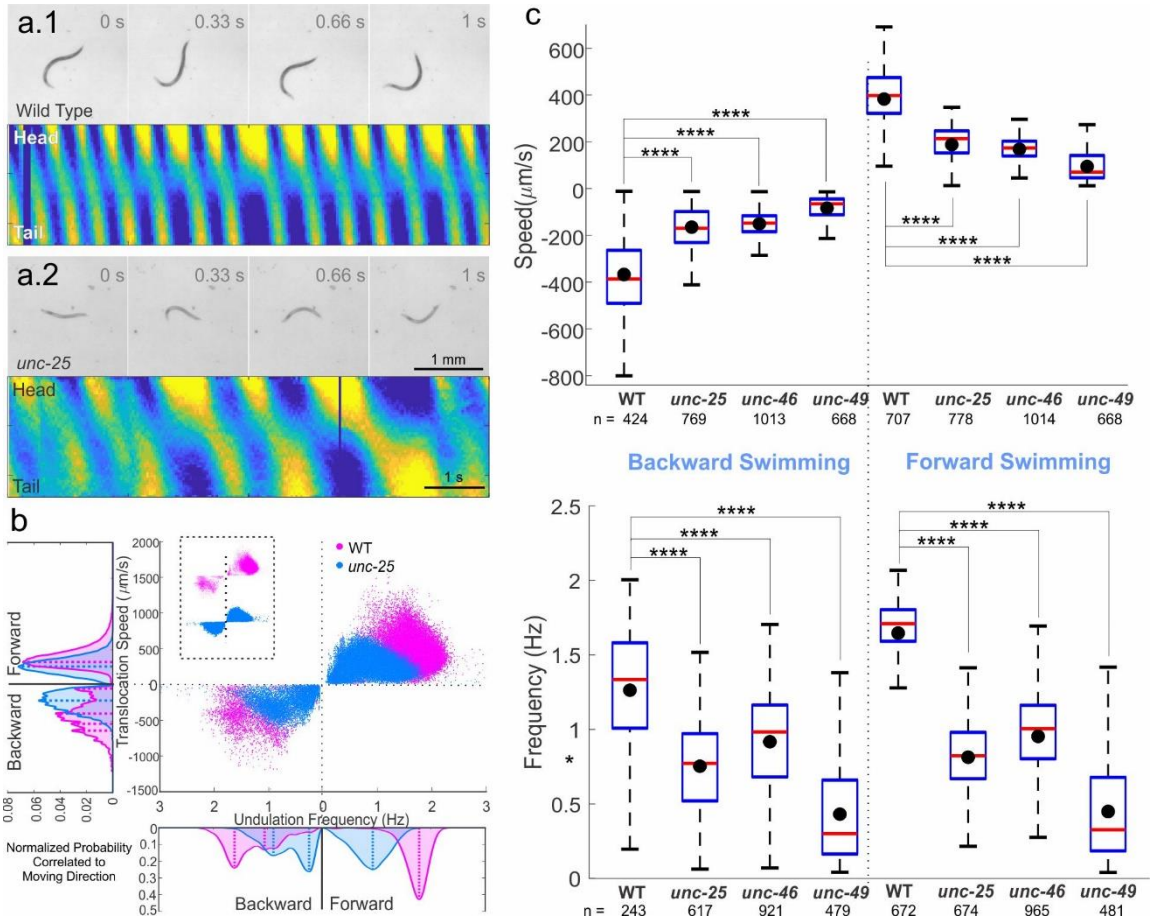

Figure 2.6 GABA transmission knockouts swam slower than wild type. Compared to wild type (a.1), *unc-25* knockout (a.2) swam in liquid with lower undulation frequency and translocation speed, as well as smaller undulation amplitude and wavelength. Video frames are 0.33 s apart; scale bars are 1 mm; and kymograms are color coded as in Figure 2.2, scale bars are 1 s. (b) Wild type swam faster with higher translocation speed and undulation frequency, compared to *unc-25* knockout. Area plots are probability occurrence within each direction, forward or backward. The dashed lines indicate the main peaks in the area plots. (c) Translocation speeds and undulation frequencies of all the GABA transmission knockouts were significantly lower than those of wild type (WT) during forward and backward swimming. Box plots as in Fig. 4. ANOVA with Tukey pairwise comparison to wild type, **** $p<0.0001$. See Table 2.4 for details.

Table 2.4 Locomotion Parameters of Wild type and GABA Transmission Knockout Animals During Free Locomotion Tracking

		Translocation Speed (μm/s)			Undulation Frequency (Hz)			Maximal Amplitude (μm)			Primary Wavelength (μm)		
		mean ±SD	One-way ANOVA	p value (Tukey test)	mean ±SD	One-way ANOVA	p value (Tukey test)	mean±SD	One-way ANOVA	p value (Tukey test)	mean±SD	One-way ANOVA	p value (Tukey test)
Wild Type	Backward Crawling	-108±47	F(3,878) = 64.73, p < 0.0001	--	0.40±0.17	F(3,431) = 8.65, p < 0.0001	--	227±66	F(3,878) = 37.22, p < 0.0001	--	730±260	F(3,843) = 16.42, p < 0.0001	--
unc-25		-70±28		<0.0001	0.32±0.38		0.0295	168±57		< 0.0001	644±113		< 0.0001
unc-46		-63±22		<0.0001	0.32±0.25		0.0307	177±62		< 0.0001	655±114		< 0.0001
unc-49		-34±22		<0.0001	0.25±0.36		<0.0001	208±64		0.0069	646±156		< 0.0001
Wild Type	Forward Crawling	148±114	F(3,987) = 136.49, p < 0.0001	--	0.37±0.2	F(3,682) = 14.10, p < 0.0001	--	225±55	F(3,987) = 44.01, p < 0.0001	--	716±125	F(3,955) = 10.98, p < 0.0001	--
unc-25		90 ±69		<0.0001	0.37±0.17		0.9997	176±50		< 0.0001	662±90		< 0.0001
unc-46		73±69		<0.0001	0.31±0.19		0.0314	181±55		< 0.0001	668±99		< 0.0001
unc-49		47±67		<0.0001	0.25±0.16		<0.0001	212±60		0.0461	665±143		< 0.0001
Wild Type	Backward Swimming	-367±145	F(3,2870) = 802.42, p < 0.0001	--	1.26±0.49	F(3,2256) = 373.06, p < 0.0001	--	294±70	F(3,2863) = 430.86, p < 0.0001	--	866±91	F(3,2715) = 316.55, p < 0.0001	--
unc-25		-165±42		<0.0001	0.75±0.49		<0.0001	209±52		< 0.0001	691±84		< 0.0001
unc-46		-150±30		<0.0001	0.92±0.31		<0.0001	186±49		< 0.0001	746±59		< 0.0001
unc-49		-84±18		<0.0001	0.43±0.27		<0.0001	230±47		< 0.0001	729±125		< 0.0001
Wild Type	Forward Swimming	383±132	F(3,3163) = 1391.20, p < 0.0001	--	1.65±0.26	F(3,2788) = 1684.89, p < 0.0001	--	273±38	F(3,3163) =927.68, p < 0.0001	--	885±59	F(3,3082) = 830.09, p < 0.0001	--
unc-25		188 ±77		<0.0001	0.81±0.27		<0.0001	194±39		< 0.0001	694±73		< 0.0001
unc-46		168±53		<0.0001	0.95±0.27		<0.0001	178±34		< 0.0001	743±50		< 0.0001
unc-49		94±51		<0.0001	0.45±0.33		<0.0001	225±44		< 0.0001	738±123		< 0.0001

The GABA transmission knockout animals are chronically impaired and the effects we describe on locomotion could arise during development or due to compensation mechanisms. Therefore, we studied the locomotion of a transgenic strain (TOL12) that expresses Archaerhodopsin-3 (Arch3) on the cellular membrane of GABAergic motoneurons, so they can be acutely inactivated by light. Arch3 is a light-sensitive proton pump that requires the cofactor all-trans-retinal (ATR) and causes hyperpolarization when exposed to lime-colored light (Nagel et al., 2005; Okazaki et al., 2012). We fed transgenic animals with ATR for 24 hours and tracked their swimming or crawling behaviors under infrared light (that does not activate Arch3) and then under lime-colored light, which is the optimal activation wavelength of Arch3 (Mattis et al., 2011; Okazaki et al., 2012). To prevent desensitization of Arch3 after long exposure, we limited lime-colored light to 1 minute (Okazaki et al., 2012). We also tracked locomotion behavior of transgenic animals that were not fed ATR, as a negative control. When GABA transmission was inactivated acutely by hyperpolarizing GABAergic motoneurons the frequency of undulations decreased, comparable to the effect of GABA transmission mutants. Swimming under lime-colored light, the transgenic animals fed with ATR were slower and less coordinated and their maximal amplitude and primary wavelength decreased while quickly recovered when the optogenetic activation light was turned off (Figure 2.7abc). Crawling NGM agar surface, their translocation speed was significantly lower than that of the same animals under infrared light and that of the animals not fed ATR. Their undulation frequency was lower than that of the same animals under infrared light and that of the animals not fed ATR. Swimming in NGM buffer, their translocation speed was significantly lower than that of the same animals under infrared light and that of the animals not fed ATR. Their

undulation frequency was significantly lower than that of the same animals under infrared light and that of the animals not fed ATR (Figure 2.7d, Table 2.5).

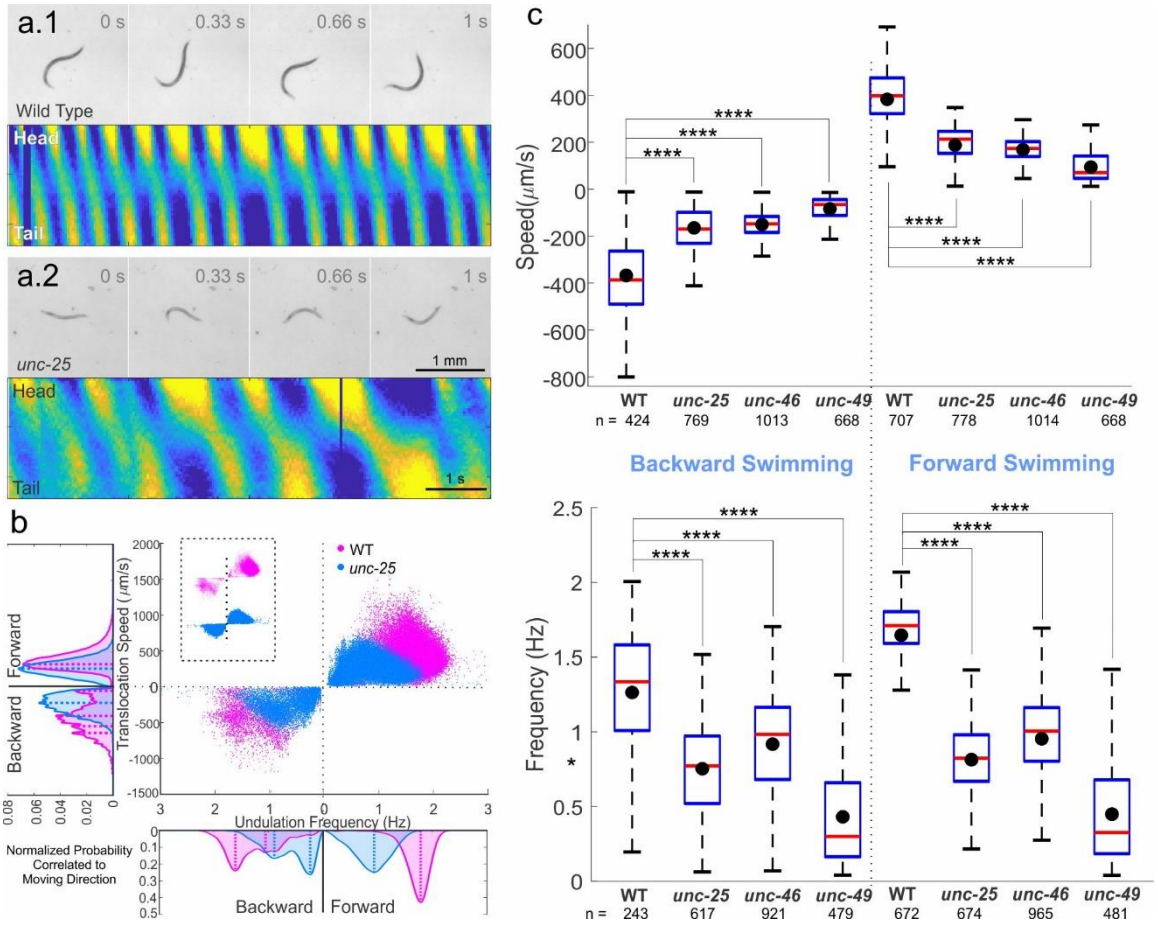

Figure 2.7 GABA transmission knockouts swam slower than wild type. Compared to wild type (a.1), *unc-25* knockout (a.2) swam in liquid with lower undulation frequency and translocation speed, as well as smaller undulation amplitude and wavelength. Video frames are 0.33 s apart, scale bars are 1 mm; and kymograms are color coded as in Figure 2, scale bars are 1 s. (b) Wild type swam faster with higher translocation speed and undulation frequency, compared to *unc-25* knockout. Area plots are probability occurrence within each direction, forward or backward. The dashed lines indicate the main peaks in the area plots. (c) Translocation speeds and undulation frequencies of all the GABA transmission knockouts were significantly lower than those of wild type (WT) during forward and backward swimming. Box plots as in Figure 2.4. ANOVA with Tukey pairwise comparison to wild type, **** $p<0.0001$. See Table 2.5 for details.

Table 2.5 Kinematic Parameters of The Optogenetic Animals (TOL12) During Free Locomotion Tracking

			Translocation Speed (μm/s)			Undulation Frequency (Hz)		
Conditions		Locomotion	mean±SD	One-way ANOVA	p value (Tukey test)	mean±SD	One-way ANOVA	p value (Tukey test)
Control	No ATR under Infrared Light	Backward Crawling	-123±106	F(2,397) = 16.48, p < 0.0001	<0.0001	0.42±0.18	F(2,195) = 5.03, p = 0.0074	0.0074
	ATR under Infrared Light		-101±81		0.0017	0.34±0.18		0.7423
Experimental	ATR under Lime Light		-67±52		Comparison Reference	0.32±0.18		Comparison Reference
Control	No ATR under Infrared Light	Forward Crawling	201±72	F(2,918) = 83.66, p < 0.0001	<0.0001	0.40±0.09	F(2,845) =20.16, p < 0.0001	<0.0001
	ATR under Infrared Light		171±66		<0.0001	0.37±0.09		0.0079
Experimental	ATR under Lime Light		133±68		Comparison Reference	0.34±0.10		Comparison Reference
Control	No ATR under Infrared Light	Backward Swimming	-312±103	F(2,783) = 111.59, p < 0.0001	<0.0001	1.11±0.20	F(2,617) = 47.63, p < 0.0001	<0.0001
	ATR under Infrared Light		-248±53		<0.0001	1.01±0.39		<0.0001
Experimental	ATR under Lime Light		-140±26		Comparison Reference	0.73±0.43		Comparison Reference
Control	No ATR under Infrared Light	Forward Swimming	315±102	F(2,899) = 192.43, p < 0.0001	<0.0001	1.36±0.30	F(2,840) = 181.45, p < 0.0001	<0.0001
	ATR under Infrared Light		247±88		<0.0001	1.07±0.28		<0.0001
Experimental	ATR under Lime Light		162±84		Comparison Reference	0.76±0.46		Comparison Reference

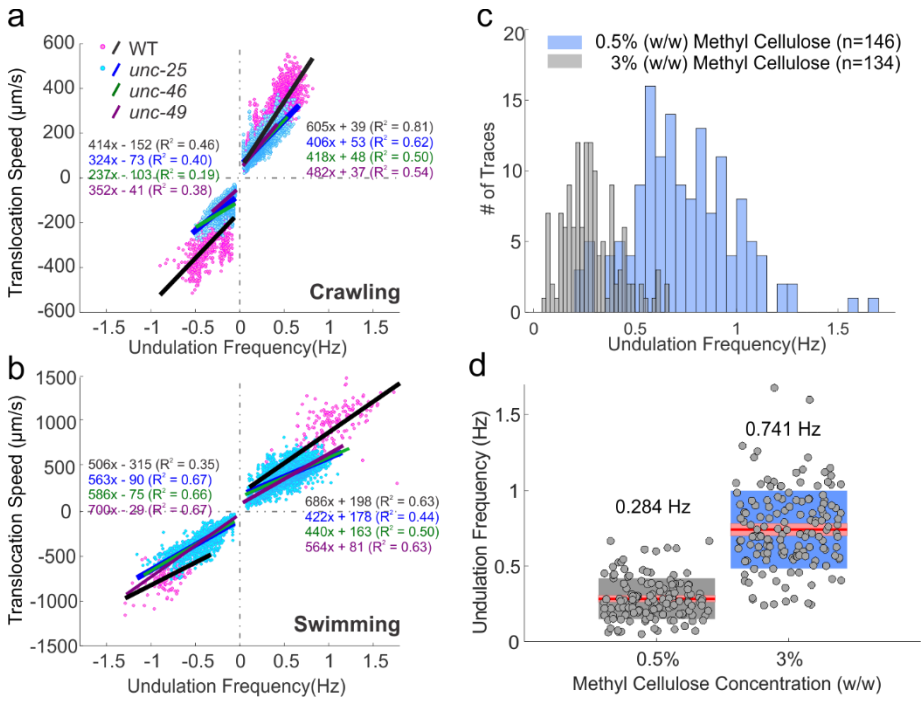

Figure 2.8 During sinusoidal undulation, the undulation frequency correlates to translocation speed; different relevant undulations frequencies were induced by setting ambient viscosity in the microfluidic waveform channels. (ab) Undulation frequency was positively correlated with translocation speed during crawling and swimming. Wild type (magenta dots) and *unc-25* (cyan dots) data were selected from time in which animals performed sinusoidal locomotion. Fitted linear regression lines of wild type (black), *unc-25* (blue), *unc-46* (green) and *unc-49* (purple) strains, coefficients of determination (R^2) and equations are labeled in with the same colors. (c) In waveform microfluidic device, animals can undulate in predetermined channels designed to restrict their path. When the ambient viscosity was high (3% methyl cellulose solution) wild type undulated in lower undulation frequencies than in less viscous environment, (0.5% methyl cellulose solution). Frequency was measured by the movement of neurons and muscle during calcium imaging and sample size (n) is the number of cells analyzed. (d) Same data as c. The average undulation frequency in 3% methyl cellulose solution was 0.28±0.14, and that in 0.5% solution was 0.74±0.26 Hz. Red lines are mean values, pink boxes are 95% confidence intervals for the mean, gray and blue boxes are standard deviation, and gray dots are individual data points.

During free crawling or swimming *C. elegans* exhibits a variety of behaviors from forward or backward almost-sinusoidal undulations, through omega and delta turns, direction changes and pauses, to periods of quiescence (Stephens et al., 2008). When GABA transmission is impaired by knockout mutations or optogenetic inactivation, *C. elegans* becomes less coordinated, their undulation frequencies and translocation speed

decrease. In order to compare the efficiency of harnessing undulation frequency to produce translocation speed in wild type and mutants, we isolated and analyzed the almost-sinusoidal undulations. For all strains, in both directions of crawling and swimming, there were positive linear correlations between undulation frequency and translocation speed. Wild type translocated further with the same undulation frequency compared to any of the GABA transmission knockout strains (Figure 2.8ab).

2.3.4 GABAergic motoneurons showed different activation patterns during low and high undulation frequency

Our behavior analysis demonstrated that in the absence of GABA transmission animals did not move at high undulation frequency and translocation speed in either direction during free locomotion or in response to harsh touch stimulation to the head or tail. Yet, they were capable of slow dorsoventral undulation in both directions during free locomotion and after stimulation. Moreover, when only sinusoidal undulations are considered, undulation frequency is a predictor of translocation speed in wild type and mutants, with wild type exhibiting higher efficiency. Together these results suggest that GABAergic motoneurons' contribution depends on undulation frequency and that they are necessary for high-frequency undulation.

To determine the contributions of GABAergic motoneurons during low and high undulation frequency, we recorded their activity with a genetically encoded calcium sensor. We facilitated keeping track of the locomotive phase and undulation frequency by using a silicon microfluidic device with sinusoidal waveform channels designed to mimic the crawling path of wild type animal (Figure 2.9a) (Lockery et al., 2008). Taking advantage of the predetermined shape of the channel and the published peri-motor location of each motoneuron (Chen et al., 2006; Haspel and O'Donovan, 2011), we converted the soma

position of GABAergic motoneurons during imaging to the locomotive phase of their neuromuscular junction to body-wall muscle. We assigned phases of the locomotion cycle to the location in the channel according to the animal's dorsoventral bending and direction of movement. We define the peak of dorsal bending as 90° and that of ventral bending as 270°, with other positions in the channel assigned accordingly. To manipulate the undulation frequency, we changed the viscosity of the fluid inside the channels with increasing concentration of methyl cellulose (in NGM buffer) up to 3% (w/w) methyl cellulose (higher concentrations prevented animals from entering the channels). When animals crawled in 3% (w/w) methyl cellulose, the mean undulation frequency was 0.28±0.14 Hz, which is close to the undulation frequencies of the GABA transmission knockouts during forward crawling (0.32±0.18 Hz, $p = 0.9$). When animals crawled in 0.5% (w/w) methyl cellulose, they could move faster with a mean undulation frequency of 0.74±0.26 Hz, which is above 99.5% of undulation frequency data points obtained in free forward crawling recording (Figure 2.8cd). We imaged calcium level changes in the cytoplasm of body-wall muscle cells with GCaMP2 (TOL15) in 1.5% (w/w) methyl cellulose and in the cytoplasm of GABAergic motoneurons with GCaMP6 (TOL11) in 0.5% and 3% (w/w) methyl cellulose. Regardless of methyl cellulose concentration, we used 0.6 Hz as the cut-off to categorize data into low and high undulation frequency. Because *C. elegans* infrequently moved backward in the channels, we only collected and analyzed calcium imaging data for forward locomotion.

Calcium imaging signals from the body-wall muscle correlated to muscle contraction and bending. The signal increased when ventral muscle cells went through ventral bending (270°, Figure 2.9b), and when dorsal muscle cells went through dorsal bending (90°).

During high undulation frequency, the GABAergic motoneurons exhibited a sustained level of activation with distinct troughs of phasic inactivity (Figure 2.9c). VD motoneurons exhibited an inactive phase around ventral bending (270°), while DD motoneurons exhibited an inactive phase around dorsal bending (90°). Both VD and DD had an inactive phase around 180°, and only VD had a rise in calcium level between 270° and 360°. In contrast, during low undulation frequency, VD and DD showed the same calcium signal pattern -- a wide inactive phase from 90° to 270°. To examine the contribution of movement to the recorded signal, we recorded the change of fluorescence from calcium insensitive green fluorescent protein (GFP) in GABAergic motoneurons in 0.5% and 3% (w/w) methyl cellulose. Regardless of motoneuron subsets or viscosity conditions, the fluorescence signal of GFP showed the similar pattern: a wide increase from 180° to 360° correlated to ventral bending. Because the fluorescence intensity of GFP is 20-fold brighter than that of GCaMP6, the increase in fluorescence intensity might be due to the decrease in motoneuron volume when the ventral nerve cord went through ventral bends.

Therefore, GABAergic motoneurons exhibited different patterns of activation during high and low undulation frequency. In high-frequency mode, VD and DD motoneurons have different inactive phases, while in low-frequency VD and DD motoneurons showed similar wide inactive phases.

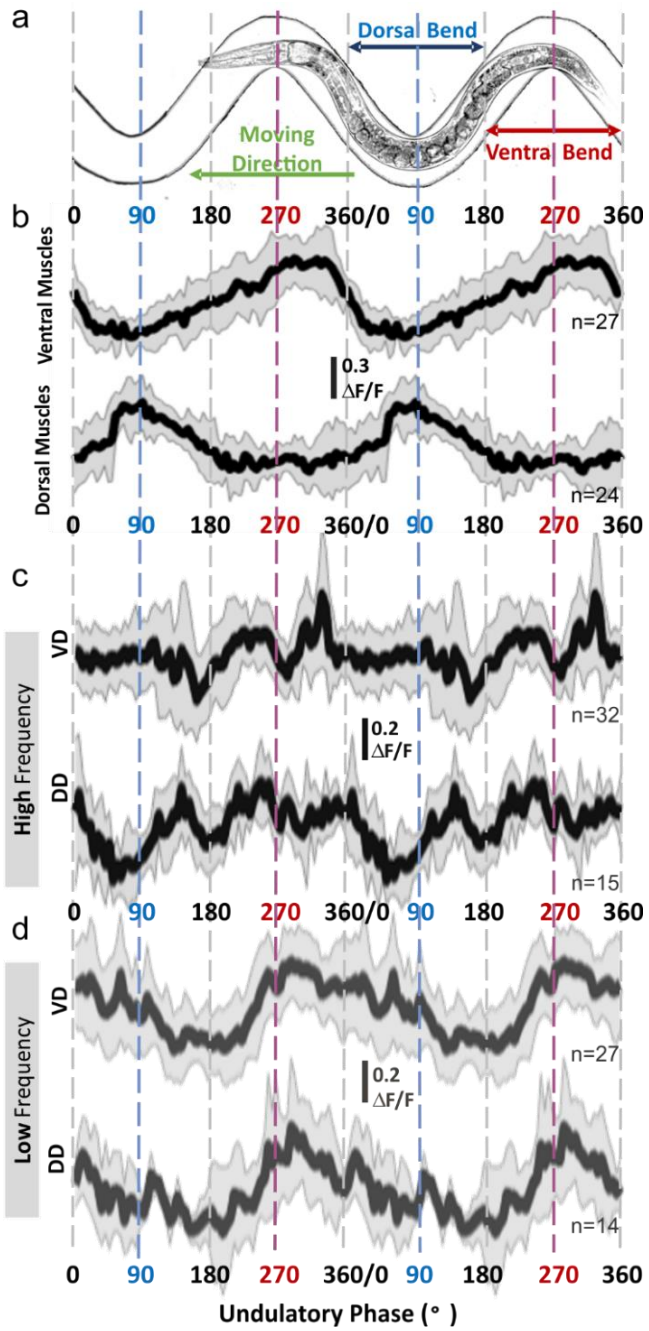

Figure 2.9 Calcium signal pattern of GABAergic motoneurons were different during low and high undulation frequency. (a) animals were free to move in sinusoidal microfluidic channels so that the undulatory cycle, including dorsal and ventral bends are fixed in space. (b) Body-wall muscle cells were active at the inside of body bends (e.g. dorsal muscles were active during dorsal bend around 90°). (b) During high undulation frequency crawling, VD showed two troughs around 180° and 270°, and DD around 90° and 180°; only VD showed a sharp increase around 300°. (c) During low undulation frequency crawling, VD and DD both showed a similar activity with a wide trough around 180°. The sample size (n) indicates the number of analyzed cells. Solid lines and shaded areas in calcium traces are mean and the standard deviation. $\Delta F/F = (F_{top50\%}-F_{BG}) / (\Sigma(F_{top50\%}-F_{BG})/n)$.

2.3.5 Computational models tested three hypotheses for the role of inhibition in fast locomotion

Based on the experimental results, we suggest five hypotheses to explain the role of inhibition in sustaining high-frequency locomotion. First, cross-inhibition of the opposing body wall muscles increases the dorsoventral difference in muscle activation. Second, disinhibition of the innervated body wall muscles increases muscle activation, particularly during its rising phase. Third, inhibitory reset of VA and VB from VD allows higher locomotion frequency through phasic inhibition of ventral motoneurons (Boyle et al., 2012). Fourth, VD disinhibition of VA and VB ventral cholinergic motoneurons amplifies in particular during their rising phase. Fifth, reciprocal inhibition between VD and DD motoneurons stabilizes dorsoventral alternation.

From the experimental results, we found that *vab-7* mutants (in which DB neurons differentiate as VA) and *unc-4* mutants (in which DA and VA differentiate as DB and VB) were not different from wild type in their shrinking response to harsh head and tail touch, respectively. This suggests that the mechanism for the shrinking response is not caused by the coactivation of forward and backward premotor interneurons (AVA and AVB); instead, it is localized within the motor circuit. Furthermore, shrinking appears qualitatively similar in the forward and backward motor circuits. We, therefore, focused our computational models on forward locomotion. Our model results can be reproduced for backward locomotion by changing the direction of the propagating wave under feedforward control or by changing the direction of the proprioceptive field under feedback control (Denham et al., 2018). Our model results are only applied within the scope of the function of inhibition, and we do not assume that forward and backward circuits are driven by the same mechanism.

There are two prevalent hypotheses to explain the undulatory body bends in *C. elegans*: the proprioception (feedback-driven) hypothesis and the endogenous oscillator (feedforward-driven or central pattern generator) hypothesis. Proprioception transduces body curvature to adjacent body segments, so that rhythmic movement propagates along the body; endogenous oscillators (CPG circuits) generate rhythmic movement at the head or tail of the animal, or along the body (Gjorgjieva et al., 2014). Although proprioception and endogenous oscillators have been evidenced in *C. elegans*, their relative contributions during locomotion remain to be determined. Previous models (Denham et al., 2018; Izquierdo and Beer, 2018) have investigated these regimes separately in order to parse their qualitative differences.

The models we used in this study are based on evidence for proprioceptive mechanisms (Wen et al., 2012) and for endogenous oscillators that could provide feedforward motor control (Gao et al., 2018). Using the proprioceptive mechanisms, we tested cross-inhibition, disinhibition, and inhibitory reset. Using the CPG-driven model, we tested cross-inhibition and disinhibition. The role of GABAergic motoneurons in rhythm generation in the *C. elegans* nerve cord remains uncharacterized and is not addressed in our models. In particular, more detailed neural models would be required to test VD disinhibition of VA and VB motoneurons and reciprocal inhibition between VD and DD motoneurons. In addition, a consequence of modeling purely feedforward, CPG-driven motor activity is the absence of a mechanism for the modulation of frequency e.g. in response to changes in environmental viscosity. For both models, we simulated locomotion in two environments (agar-like and liquid-like) but did not directly manipulate undulation frequency within a given environment. We simulated forward locomotion in

agar-like and liquid environments under proprioceptive and CPG control. Then, we compared simulations of wild type animals with simulations that incorporate perturbations of the neuromuscular input due to the omission of cross-inhibition, disinhibition, or both (Figure 2.10).

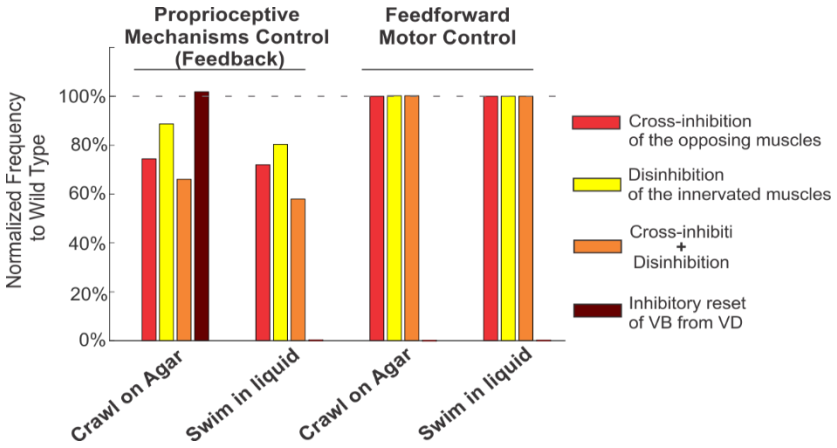

Figure 2.10 Computational model disambiguated hypotheses for role of inhibition. Three hypotheses for the role of inhibition (cross-inhibition of the opposing muscles in red, disinhibition of the innervated muscles in yellow, and inhibitory rest of VB from VD in brown) and one combination (cross-inhibition and disinhibition of muscles in orange) were tested in proprioceptive and feedforward motor control models. In proprioceptive mechanisms control model, these inhibitions play important roles in sustaining rapid undulatory alternations, as in liquid environment the undulation frequency reduced by 100% to 18% of the undulation frequency of wild type. In feedforward motor control model [1], only the inhibitory reset of VB from VD resulted in large undulation frequency reduction by 100% from undulation frequency of wild type.

Under proprioceptive control, all three perturbations induced a substantial decrease in undulation frequency. Simulated mutants lacking cross-inhibition of the opposing muscles showed the largest reduction (25% and 28% of simulated wild type frequency in agar-like and liquid environments, respectively), followed by simulated mutants lacking disinhibitory rebound in the innervated muscle (22% and 20% of wild type frequency in agar-like and liquid environments, respectively). Applying both manipulations simultaneously decreased the undulation frequency of the wild type even further (by 34%

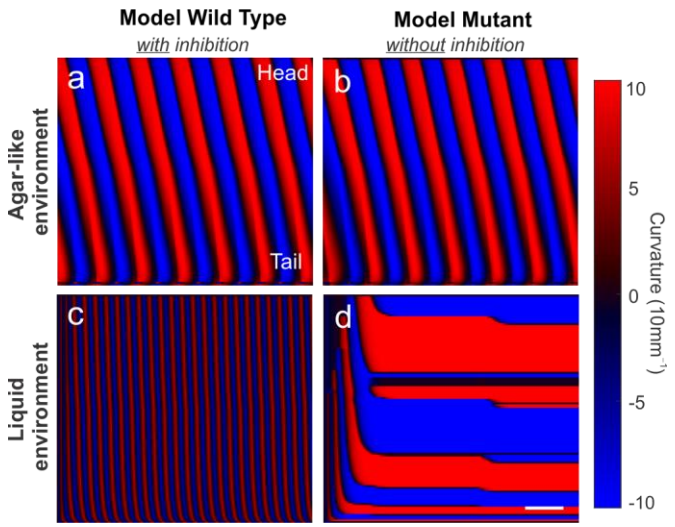

Figure 2.11 In proprioceptive mechanisms control model, elimination of inhibitory reset of VB from VD caused failure in generating curvature along the body. The kymograms show curvature dynamics in environments in agar-like environment (ab) and liquid environment (cd) of model wild type animal (ac) and model mutant animal (bd). In agar-like environment, there is no difference with or without the inhibitory reset. In water environment, elimination of the inhibition resulted in failure of curvature generation along the body. Scale bar = 1 s.

and 42% in agar-like and liquid environments, respectively). Intuitively, for proprioceptive control, continuous activation within the antagonistic muscle during bending causes stiffness of muscles, slowing down bending, and in turn delaying the state switch of the adjacent motoneurons (i.e., the propagation of the undulatory wave). The same simulations also showed a decrease in overall locomotion speed, which was proportional to the frequency decrease in liquid, but disproportionately small in agar. In contrast, in our model of CPG control, muscle inhibition had no effect on the undulation frequency. We also found that removing cross-inhibition of model muscles results in reduced speed, whereas removing muscle disinhibition resulted in increased locomotion speeds, indicating that the propagation of smooth sinusoidal, rather than square, muscle activation wave is mechanically more efficient (Lighthill, 1960). Together, these results suggest that the observed frequency-speed dependence is a signature of proprioceptively driven neural

control. Our model further suggests that inhibition of GABAergic motoneurons influences undulation frequency primarily at the neuromuscular junctions. We note that additional frequency modulation mechanisms, which lie outside the scope of our model, may also be present under CPG-driven control.

We next tested the inhibitory reset of the neuronal synapse from VD to VB. A previous neuromechanical model by Boyle *et al.* (2012) suggests that as a consequence of bistability of the A- and B-type motoneurons (Liu et al., 2014), ventral and dorsal motoneurons may simultaneously occupy the same state, effectively pausing locomotion in a manner that is reminiscent of the *shrinker* phenotype. To resume healthy locomotion, Boyle *et al*. (2012) proposed that VD to VB inhibition acts as a neural reset mechanism, switching VB off in order to facilitate a dorsal bend. Simulations of Boyle *et al*.'s model show that this neural reset has little effect on slow locomotion (in the agar-like environment) but is required for coordinated undulations during fast locomotion (in the liquid environment). This result inspired our third hypothesis and the reimplementation of this mechanism in the current model (see Methods). We simulated animals lacking neural inhibition of VB by VD in our proprioceptive model. The simulated mutant did not show any significant change in frequency in an agar-like environment (Figures 2.10 and 2.11). However, when simulated in a liquid-like environment, these simulated mutants became severely uncoordinated and fail to make progress, consistent with Boyle *et al.* (2012). This result indicates a requirement for a neural inhibitory reset mechanism to sustain coordinated fast undulations, at least in the absence of additional backup mechanisms (such as CPG control).

To summarize, our model results suggest that under proprioceptively driven locomotion, muscle cross-inhibition enhances locomotion frequency and speed. The associated frequency-speed dependence is consistent with our experimental observations. In this model, cross-inhibition and disinhibition of the body-wall muscles support high-frequency undulatory locomotion, whereas the neural inhibition within the motor circuit can stabilize high-frequency undulations.

2.4 Discussion

We investigated the role of inhibition in the locomotion circuit by analyzing the behavior of wild type and mutant animals, recording neuronal and muscular activity in undulating intact animals, and testing possible mechanisms with a computational model. Both wild type and GABA transmission mutants responded to harsh touches to the head or tail by shrinking, suggesting that dorsoventral coactivation is produced by the unimpaired nervous system. Impairment of GABA transmission, either genetically or optogenetically, induced lower undulation frequency and lower translocation speed during crawling and swimming in both directions. GABAergic motoneurons' activity pattern was different during low and high undulation frequency. During low undulation frequency, VD and DD showed the similar activity pattern; while during high undulation frequency their activity alternate. We suggested three hypotheses for the inhibitory mechanism in high-frequency undulation and tested them computationally. Our model results suggested that cross-inhibition and disinhibition of the body-wall muscles support high-frequency undulatory locomotion. Finally, we suggest that the unimpaired locomotion circuit produces an undulatory motor program by two distinct modes of operation for low and high frequency undulations.

2.4.1 Shrinking occurs in wild type and GABA transmission mutants

The shrinking response, presumably from coactivation of dorsoventral muscle has been described in GABA transcription mutants (McIntire et al., 1993a; McIntire et al., 1993b) and following laser ablation of GABAergic motoneurons (Yanik et al., 2004). Here we show that shrinking commonly occurs in wild type animals in response to noxious touch stimuli to the head or tail. The shrinking response does not require the simultaneous contribution of cholinergic motoneurons associated with forward and backward directions. *vab-7* and *unc-4* mutant animals in which A- or B-type of cholinergic motoneurons are impaired, show shrinking response after the harsh touch stimulation which induces their normal undulatory locomotion (e.g. harsh head touch to *vab-7* induces wild-type-like brief shrinking response and rapid sinusoidal backward undulation). These results suggest that shrinking is not associated with backward locomotion or with a change of direction but rather with the switch from slow to fast locomotion and that shrinking is part of the motor program produced by the unimpaired nervous system.

The shrinking phenotype was first described in mutants and not discovered in wild type animals (McIntire et al., 1993b), probably because the latter resolve the coactivation and swiftly move away from noxious stimuli. It is therefore unlikely to capture the body shrinkage of wild type animals with the naked eyes and it requires a frame-by-frame inspection of video microscopy. Morphological measurement of the change of body length before and after harsh touch stimulation revealed that every animal, either wild type or the GABA transmission knockouts, shrank. It is the longer-lasting shrinkage and lower translocation speed of GABA transmission mutants that make the observation of shrinking phenotype easier.

2.4.2 The distinct phenotype of GABA transmission mutants is slow swimming

GABA transmission mutants, colloquially named *'shrinkers'*, such as *unc-46* and *unc-47* mutant strains defective in GABA vesicular transporter and *unc-49* mutant strain defective in anionic $GABA_A$ receptor, have been described as defective in backward locomotion because they fail to produce the wild type swift reversal following a harsh touch on the head (McIntire et al., 1993a; McIntire et al., 1993b; Schuske et al., 2004). A similar phenotype was described in animals that after laser ablation (Yanik et al., 2004). However, we found that the shrinking phenotype is not related to the target of noxious stimuli or direction of locomotion, as GABA transmission mutants shrink in response to harsh touch to the tail as well as the head. Moreover, wild type animals exhibit shrinking phenotype although smaller in magnitude and quicker to resolve. When suspended in liquid, GABA transmission mutants are uncoordinated and swim slowly with lower undulation frequency and translocation speed compared to those of wild type. They exhibit a similar but less prominent phenotype while crawling on agar plates. Hence, slow and uncoordinated swimming, rather than shrinking, is the distinct phenotype of GABA transmission mutants.

2.4.3 GABA transmission is necessary for fast dorsoventral alternation

During free crawling or swimming in either direction, an acute or chronic absence of GABA transmission leads to lower undulation frequency and translocation speed. The effect is more significant during swimming that is typically performed at higher undulation frequency. Even following noxious harsh touch stimuli that induce a rapid escape response in wild type, GABA transmission mutants do not increase their undulation frequency and translocation speed and are slower than those of wild type. These results deem GABA transmission necessary for fast locomotion. Yet GABA transmission mutants alternate

dorsoventral body-wall muscles to move at lower undulation frequency and translocation speed, in comparable pattern to wild type.

Undulation frequency dictates translocation speed during sinusoidal crawling and swimming behaviors in wild type and mutant animals. Correlations between undulation frequency and translocation speed were always positive and stronger during crawling than in swimming, probably due to slippage. The slope of the linear regression was always steeper for wild type, suggesting a more efficient translation of undulation frequency to translocation speed. This suggests a subtle contribution of inhibition to the motor program of slow locomotion because the data for locomotion of mutant animals is for slower translocation speed. Shape related parameters such as amplitude and wavelength are weakly correlated to instantaneous translocation speed, although they may contribute to fast locomotion.

2.4.4 GABAergic motoneurons exhibit dorsoventral alternating inactive phases that match the activation of their postsynaptic body-wall muscles only during high-frequency undulation

Morphologically, GABAergic motoneurons synapse to the muscle arms of body-wall muscles (White et al., 1976, 1986), and their inhibitory effect on body-wall muscles was confirmed by laser ablation, muscle electrophysiology during bath application of GABA, and activation GABAergic motoneurons optogenetically (McIntire et al., 1993b; Bamber et al., 2005; Gao and Zhen, 2011; Inoue et al., 2015). The neuronal activity of the GABAergic motoneurons has not been reported and was presumed to be similar to that of its antagonistic muscle, as both are activated by the same excitatory motoneurons. However, when we recorded the changes in calcium levels in GABAergic motoneurons during undulations we found that they exhibit a baseline level of activity interspaced by phases of

inactivity and that the pattern of activity was frequency-dependent. In high-frequency undulation, when ventral body-wall muscles were activated around 270° of the locomotion cycle, VD motoneurons were inactive and when the dorsal body-wall muscles were activated around 90° DD motoneurons were inactive (Figure 2.9). These inactivity windows could allow postsynaptic muscles to escape from inhibition and be activated more sharply, or they could amplify muscle activity through disinhibition. In contrast, during low-frequency undulation, VD and DD exhibit similar activity patterns with a wide inactivity trough from 90° to 270° that include portions of ventral and dorsal bending regions. Our calcium imaging of GABAergic motoneurons further supports their involvement in high-frequency undulations as their activity patterns are different for low and high undulation frequencies.

2.4.5 Other possible inhibitory roles of GABAergic motoneurons in high-frequency undulation

GABAergic motoneurons might play several inhibitory roles during high-frequency undulation. We tested three hypotheses for the neuronal mechanisms that underlie these roles using proprioceptive mechanisms control and feedforward motor control models: 1) Cross-inhibition, in which when the body wall muscle is activated, the coactivated GABAergic motoneurons inhibit the opposing body wall muscle; 2) disinhibition of the innervated body wall muscles, in which the release from inhibition enhances muscle activation in particular during its rising phase; 3) inhibitory reset of VA and VB, in which VD input terminates the locomotion cycle early and allows higher locomotion frequency (Boyle et al., 2012; Cohen and Sanders, 2014; Cohen and Denham, 2019). Our model results suggested that cross-inhibition and disinhibition of the body-wall muscles support high-frequency undulatory locomotion, whereas the neural inhibition within the motor

circuit stabilizes such high-frequency undulations. Besides the aforementioned roles of inhibition, there are other possible roles that we did not test because of experimental or computational model limitations. First, VD disinhibition of VA and VB, in which the activation of ventral cholinergic motoneurons is amplified in particular during their rising phase. Second, reciprocal or nonreciprocal inhibition between DD and VD motoneurons which might reinforce the antiphasic activity of GABAergic motoneurons during rapid locomotion. All these inhibition or disinhibition are not exclusive in sustaining the fast dorsoventral body-wall muscle alternation. Cross-inhibition and disinhibition of muscles fulfill the activation-relaxation alternation of dorsoventral muscles, and the neural inhibition helps to stabilize the motor circuit.

2.4.6 Two modes of locomotion

We have demonstrated that the inhibitory GABAergic motoneurons of the locomotion circuit are necessary only for high-frequency undulations and that their activity pattern during high-frequency undulations is different. The frequency-dependent activity pattern of GABAergic motoneurons, the brief shrinking behavior when initiating a rapid escape response, and the absence of high-frequency undulations when inactive suggest a role for inhibition in the unimpaired nervous system. In addition, the distributions of frequency and translocation speed during crawling in both directions in the wild type are bimodal. Together these results suggest that the locomotion circuit produces an undulatory motor program by two distinct modes of operation: low-frequency undulations that do not require inhibition and high-frequency undulations that require inhibition and in which GABAergic motoneurons exhibit alternating activity pattern.

CHAPTER 3

AN IONOTROPIC GABA RECEPTOR, EXPRESSES IN MOTONEURONS AND MUSCLE AND FUNCTIONS IN C. ELEGANS LOCOMOTION

3.1 Introduction

Inhibition is ubiquitous in the nervous system, from synapses to brain regions, to modulate neuronal signals spatially and temporally. In motor systems inhibition plays important roles in supporting fast antagonistic muscle alternation. For example, as locomotion speed increases, more neural inhibition is required (Kiehn, 2011). In Chapter 2, we suggest roles for inhibition in underlying fast undulatory locomotion of *C. elegans*.

In the ventral nerve cord, excitatory cholinergic motoneurons and inhibitory GABAergic motoneurons are hypothesized to generate the dorsoventral alternation of body-wall muscles (Gjorgjieva et al., 2014). There are two classes of inhibitory GABAergic motoneurons: thirteen VD motoneurons innervate ventral body wall muscle cells while six DD motoneurons innervate the dorsal muscle. Excitatory cholinergic motoneurons are divided into six classes: VA (12), DA (9), VB (11), DB (7), AS (11), and VC (6). VA and VB motoneurons innervate ventral body-wall muscle cells, as well as DD motoneurons. DA, DB, and AS motoneurons innervate dorsal body-wall muscle cells as well as VD motoneurons. VC motoneurons innervate ventral body-wall muscle cells very sparsely, instead, they innervate DD motoneurons; two mid-body VC motoneurons innervate vulva muscles (White et al., 1976, 1986; Haspel and O'Donovan, 2011; Emmons, 2015). Cross inhibition of muscle cells was suggested to underlie muscle alternation during backward locomotion based on motoneuronal synaptic connectivity so that when ventral cholinergic motoneurons (VA) activate ventral body-wall muscles, they activate DD

motoneurons to inhibit dorsal muscles at the same time, and vice versa to dorsal cholinergic motoneurons (DA and AS) and VD motoneurons (McIntire et al., 1993b). However, DB and VB motoneurons that are involved in forward locomotion (Haspel et al., 2010) also innervate VD and DD, respectively; moreover, our previous study shows that the GABAergic motoneurons are not necessary for slow dorsoventral muscle alternation, but are necessary to generate and sustain rapid alternation during fast crawling and swimming.

We suggested and tested three roles for inhibition from the GABAergic motoneurons in the locomotion circuit of *C. elegans*. First, in cross-inhibition, when muscle cells on one side of the body are is activated, GABAergic motoneurons inhibit muscle cells on the opposing side. Second, in disinhibition of body-wall muscle, the release from presynaptic GABAergic motoneurons sharpens muscle activation by excitatory motoneurons. Third, inhibitory reset of VA and VB, in which VD input terminates the locomotion cycle early. In addition, according to the published connectivity data set, VD and DD motoneurons are connected by synapses (Haspel and O'Donovan, 2011; Altun and Hall, 2020), with yet unknown function, though they may contribute in stabilizing the alternating of activity between VD and DD motoneurons during rapid undulatory locomotion.

Five genes for ionotropic $GABA_A$ receptors have been reported to express in locomotion motoneurons. GAB-1, LGC-35 and LGC-37 express in DA and DB motoneurons; GAB-1, LGC-35, LGC-36, LGC-37 and LGC-38 express in VA and VB motoneurons; GAB-1 and LGC-37 express in AS and VC motoneurons (Bamber et al., 1999; Jobson et al., 2015; Gendrel et al., 2016). LGC-35 expresses in cholinergic A and B motoneurons and was reported to function as an excitatory receptor receiving spillover GABA signal (Jobson et al., 2015; Nicholl et al., 2017). The functions of GAB-1, LGC-

36, LGC-37, and LGC-38 are unknown. No expression of $GABA_A$ receptor was reported in GABAergic motoneurons DD and VD.

UNC-49, an inhibitory ionotropic $GABA_A$ receptor, was only reported to express in body-wall muscles (Bamber et al., 1999; Bamber et al., 2005). The gene products of *unc-49* are channel subunits with three major splicing patterns: UNC-49A, UNC-49B, and UNC-49C. The major splicing products have the same N-terminus (exons 1-5), but different GABA binding domains and transmembrane domains. The coding exons of UNC-49A end at the 13^{th} exon of *unc-49*, that of UNC-49B at the 21^{st} exon, and that of UNC-49C at 26^{th} exon, which is also the last exon of the *unc-49* gene. A fourth gene product, UNC-49Cshort, includes the same C-terminus as UNC-49C but does not have N-terminus (Figure 3.1). UNC-49 subunits are not homologous to vertebrate $GABA_A$ receptor subunit classes, but close to $GABA_A$ receptor RDL in Drosophila. The UNC-49 subunits might form a heteromultimeric $GABA_A$ ionotropic receptor. UNC-49B and UNC-49C colocalize in the ventral and dorsal nerve cord, while the expressions of UNC-49A and UNC-49Cshort are undetectable (Bamber et al., 1999). UNC-49B and UNC-49C form a heteromeric receptor *in vivo*, while UNC-49B homomer is sufficient to form the receptor. The main functions of UNC-49C are reducing GABA sensitivity and increasing desensitization (Bamber et al., 1999; Bamber et al., 2005).

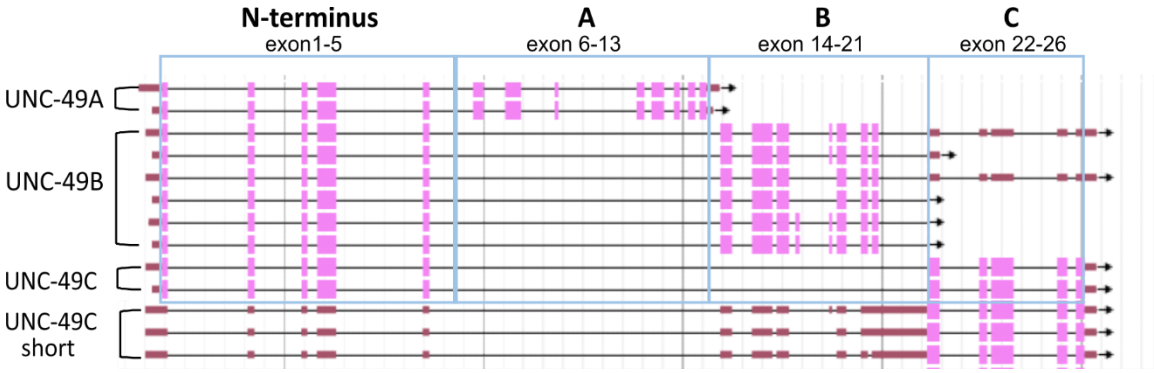

Figure 3.1 Alternative splicing of *unc-49* codes for four subunits of GABA ionotropic receptor: UNC-49A, UNC-49B, UNC-49C and UNC-49Cshort. Except for UNC-49Cshort, the other subunits share the identical N-terminus which is encoded by exon 1-5. GABA binding domain and transmembrane domain of subunit UNC-49A are encoded by exon 6-13, those of UNC-49 by exon 14-21, and those of UNC-49C and UNC-49Cshort by 22-26. Genomic map depicts introns or un-translational regions (black lines), exons (pink boxes), and 5' or 3' un-translational regions (brown boxes); each row is one *unc-49* isoform (not all the isoforms are shown). Adapted from genome browser of Wormbase (https://wormbase.org/species/c_elegans/gene/WBGene00006784#0-9f-3); accessed on Feb 20th 2020 .

All *C. elegans* locomotion motoneurons synapse onto thin processes called muscle arms that are extended from muscle cells onto the ventral or dorsal nerve cord (White et al., 1976, 1986; Altun et al., 2009; Emmons, 2015). Hence neuromuscular junctions, as well as synapses to other motoneurons, are in the ventral and dorsal nerve cords (White et al., 1976). Former studies used fluorescent proteins fused to the receptor subunits UNC-49A/B/C::GFP (Bamber et al., 1999). In this experimental design, GFP tagged proteins found in the dorsal and ventral nerve cords could be expressed on postsynaptic neurons or muscle cells. In the published connectivity dataset, there are synapses that so far got little attention from GABAergic motoneurons to motoneurons: the chemical synapses from VD to DD motoneurons, from DD to VD motoneurons, and from VD to VA and VB motoneurons. In Chapter 2, we presented calcium imaging and computational results that suggest a function for the inhibition from VD motoneurons to VA and VB motoneurons.

Therefore, we reevaluated the cellular expression of the receptor subunits UNC-49A/B/C by describing the expression of soluble cytoplasmic eGFP (spliced-off the mRNA with the trans-splicing leader *sl2*) [*unc-49p::unc-49A/B/C::sl2::egfp*] and a transcription reporter driven by the native promoter [*unc-49p::egfp*]. We used three motoneuron-identification methods and found that in the adult nematode UNC-49A/B/C expressed in body-wall muscle (as previously reported), in GABAergic motoneurons, and occasionally in VA and VB motoneurons. Furthermore, to test the contribution of UNC-49 in these tissues to support fast locomotion, we used tissue-specific promoters to transgenically rescue the expression of UNC-49 in either body-wall muscle cells, GABAergic motoneurons, or VA and VB motoneurons, in *unc-49* knockout mutants and assayed their swimming behavior. Animals that expressed UNC-49C in body-wall muscles (but not motoneurons) exhibited the largest recovery of rapid undulatory locomotion, suggesting that the main function of UNC-49 in locomotion is to mediate inhibition of body-wall muscle.

3.2 Methods

3.2.1 *C. elegans* strains

We maintained all the *C. elegans* strains under the standard laboratory condition which was on Nematode Growth Medium (NGM) agar plates with OP-50-1 *Escherichia col*i (*E. coli*) bacterial lawn at 15 or 20°C (Brenner, 1974). We used the following strains for neuron identification: TOL39 (*aatEx22 [unc-49p::unc-49 subunitA::sl2::egfp, pha-1(+), pha-1(lf) e2123 III]*), TOL65 (*aatEx65 [unc-49p::unc-49 subunitB::sl2::egfp, pha-1(+), pha-1(lf) e2123 III]*), TOL41 (*aatEx23 [unc-49p::unc-49 subunitC::sl2::egfp, pha-1(+), pha-1(lf)*

e2123 III]), TOL62 (*aatEx62 [unc-49p::unc-49 subunit A::sl2::egfp, otIs669 (NeuroPAL)V]*), TOL63 (*aatEx63 [unc-49p::unc-49 subunit B::sl2::egfp, otIs669 (NeuroPAL)V]*), TOL61 (*aatEx61 [unc-49p::unc-49 subunit C::sl2::egfp, otIs669 (NeuroPAL)V]*), TOL40 (*aatEx21 [unc-49p::egfp, pha-1(+), pha-1(lf) e2123 III]*), UL4020 *[unc-49p::gfp, unc-4p::mCherry]*, TOL29 (*aatEx9 [unc-49p::egfp, unc-25p::Cerulean, del-1p::wrmScarlet, pha-1(+)； pha-1(lf) e2123 III]*) and TOL64 (*aatEx64 [unc-49p::egfp, otIs669 (NeuroPAL)V]*). We generated UNC-49 rescue strains (details in Chapter 3): TOL51 (*aatEx27 [myo-3p::unc-49(C)::sl2:: egfp; unc-49 (lf/ko) tm5487 III]*), TOL52 (*aatEx28 [unc-25p::unc-49C::sl2::egfp; unc-49 (lf/ko) tm5487 III]*), and TOL56 (*aatEx31 [del-1p::unc-49 subunit C::sl2::egfp; unc-49 (lf/ko) tm5487 III]*). The other strains used in this study were N2 (a reference laboratory strain considered as wild type) from Caenorhabditis Genetic Center (CGC) of University of Minnesota (https://cgc.umn.edu/), and TM5487 *[unc-49 (tm5487) III]* from National Bioresource Project of Japan (https://shigen.nig.ac.jp/c.elegans/top.xhtml).

3.2.2 Plasmid construction

We constructed all plasmids using Gibson Assembly (Gibson et al., 2009; Gibson et al., 2010). We amplified plasmid fragments by PCR (Phusion® High-Fidelity PCR Master Mix), ran the PCR product in DNA agarose gel, extracted the target DNA fragments (QIAEX II Gel Extraction Kit), then assembled the fragments into plasmids (NEB Gibson Assembly® Cloning Kit).

We PCR-amplified DNA fragments from N2 genome and other plasmids: *unc-49p* promoter (4k upstream sequence), *unc-49* subunits and *unc-49* gene were from N2 genome, green fluorescent reporter eGFP from pOKA073 (Okazaki et al., 2012), cerulean

fluorescent protein from pCS2+8CCerulean (Addgene plasmid; http://n2t.net/addgene:34937) (Gokirmak et al., 2012), and red fluorescent protein wrmScarlet and transplicing sequence *sl2* from pSEM89 (El Mouridi et al., 2017).

3.2.3 Generation of transgenic strains

We generated all the identification and rescue transgenic strains by microinjection according to the methods previously documented (Mello and Fire, 1995), except for TOL64 which was generated by crossing TOL40 with OH15262 (*NeuroPAL otIs669)*. We generated TOL39 by microinjecting 35 ng/uL *unc-49p::unc-49 subunit A::sl2:: egfp* (pLD17), 35 ng/uL *pha-1(+)* (pBX) into GE24 *[pha-1(lf) e2123 III]*, TOL65 by microinjecting 25 ng/uL *unc-49p::unc-49 subunit B::sl2:: egfp* (pLD18), 25 ng/uL *pha-1(+)* (pBX) into GE24 *[*pha-1(lf) e2123 III*]*, TOL41 by microinjecting 15 ng/uL *unc-49p::unc-49 subunit C::sl2:: egfp* (pLD19), 35 ng/uL *pha-1(+)* (pBX) into GE24 *[pha-1(lf) e2123 III]*, TOL62 by microinjecting 20 ng/uL *unc-49p::unc-49 subunit A::sl2:: egfp* (pLD17), 80 ng/uL *pBluescript* into OH15262 (*NeuroPAL otIs669*), TOL63 by microinjecting 25 ng/uL *unc-49p::unc-49 subunit B::sl2:: egfp* (pLD18), 75 ng/uL *pBluescript* into OH15262 (*NeuroPAL otIs669*), TOL61 by microinjecting 20 ng/uL *unc-49p::unc-49 subunit C::sl2:: egfp* (pLD19), 80ng/uL *pBluescript* into OH15262 (*NeuroPAL otIs669*), TOL40 by microinjecting 50 ng/uL *unc-49p:: egfp* (pLD8), 50 ng/uL *pha-1(+)* (pBX) into GE24 *[pha-1(lf) e2123 III]*, TOL29 by microinjecting 50 ng/uL *unc-49p:: egfp* (pLD8), 50ng/uL *unc-25p::Cerulean* (pLJ4), 40 ng/uL *del-1p::wrmScarlet* (pLJ1), 30 ng/uL *pha-1(+)* (pBX) into GE24 *[pha-1(lf) e2123 III]*, TOL51 by microinjecting 30 ng/uL *myo-3p::unc-49C::sl2::egfp* (pLD26); 70 ng/uL *pBluescript* into TM5487 *[unc-49 (lf/ko) tm5487]III*, TOL52 by microinjecting 30 ng/uL *unc-25p::unc-*

49C::sl2::egfp (pLD20); 70 ng/uL *pBluescript* into TM5487 *[unc-49 (lf/ko) tm5487]III*, and TOL56 by microinjecting 50ng/uL *del-1p::unc-49 subunit C::sl2::egfp* (pLD32); 50ng/uL *pBluescript* into TM5487 *[unc-49 (lf/ko) tm5487]III* (Table 3.1).

Table 3.1 Transgenic Strains for Motoneuron Identification and UNC-49 Rescue Strains

Strain Name	Genotype Name	Genotype	Generation methods	Comment
TOL39	*aatEx22*	*unc-49p::unc-49 subunit A::sl2::egfp, pha-1(+), pha-1(lf) e2123 III*	Microinjected 35 ng/uL *unc-49p::unc-49 subunit A::sl2::egfp* (pLD17), 35 ng/uL *pha-1(+)* (pBX) into GE24 *[pha-1(lf) e2123 III]*	For identifying UNC-49A in L1s
TOL65	*aatEx65*	*unc-49p::unc-49 subunit B::sl2::egfp, pha-1(+), pha-1(lf) e2123 III*	Microinjected 25 ng/uL *unc-49p::unc-49 subunit B::sl2::egfp* (pLD18), 25 ng/uL *pha-1(+)* (pBX) into GE24 *[pha-1(lf) e2123 III]*	For identifying UNC-49B in L1s. Lost, because overexpression was toxic to animals
TOL41	*aatEx23*	*unc-49p::unc-49 subunit C::sl2::egfp, pha-1(+), pha-1(lf) e2123 III*	Microinjected 15 ng/uL *unc-49p::unc-49 subunit C::sl2::egfp* (pLD19), 35 ng/uL *pha-1(+)* (pBX) into GE24 *[pha-1(lf) e2123 III]*	For identifying UNC-49C in L1s
TOL62	*aatEx62*	*unc-49p::unc-49 subunit A::sl2::egfp, otIs669 (NeuroPAL)V*	Microinjected 20 ng/uL *unc-49p::unc-49 subunit A::sl2::egfp* (pLD17), 80 ng/uL *pBluescript* into OH15262 *[otIs669(NeuroPAL)]V*	For identifying UNC-49A in NeuroPAL
TOL63	*aatEx63*	*unc-49p::unc-49 subunit B::sl2::egfp, otIs669 (NeuroPAL)V*	Microinjected 25 ng/uL *unc-49p::unc-49 subunit B::sl2::egfp* (pLD18), 75 ng/uL *pBluescript* into OH15262 *[otIs669(NeuroPAL)]V*	For identifying UNC-49B in NeuroPAL
TOL61	*aatEx61*	*unc-49p::unc-49 subunit C::sl2::egfp, otIs669 (NeuroPAL)V*	Microinjected 20 ng/uL *unc-49p::unc-49 subunit C::sl2::egfp* (pLD19), 80ng/uL *pBluescript* into OH15262 *[otIs669(NeuroPAL)]V*	For identifying UNC-49C in NeuroPAL
TOL40	*aatEx21*	*unc-49p::egfp, pha-1(+), pha-1(lf) e2123 III*	Microinjected 50 ng/uL *unc-49p::egfp* (pLD8), 50 ng/uL *pha-1(+)* (pBX) into GE24 *[pha-1(lf) e2123 III]*	For identifying *unc-49p::egfp* without identification marker

UL4020		*unc-49p::egfp, unc-4p::mCherry*	From Hope Lab	For identifying *unc-49p::gfp* with identification marker expressing in DA and VA motoneurons
TOL29	*aatEx9*	*unc-49p::egfp, unc-25p::Cerulean, del-1p::wrmScarlet, pha-1(+), pha-1(lf) e2123 III*	Microinjected 50 ng/uL *unc-49p::egfp* (pLD8), 50ng/uL *unc-25p::Cerulean* (pLJ4), 40 ng/uL *del-1p::wrmScarlet* (pLJ1), 30 ng/uL *pha-1(+)* (pBX) into GE24 *[pha-1(lf) e2123 III]*	For identifying *unc-49p::egfp* with identification markers expressing in D-motoneurons (cerulean) and VA and VB motoneurons (bright red)
TOL64	*aatEx64*	*unc-49p::egfp, otIs669 (NeuroPAL)V*	Crossed TOL40 with OH15262 (*NeuroPAL otIs669*), then screened for the homozygous of *NeuroPAL otIs669*	For identifying *unc-49p::egfp* in NeuroPAL
TOL51	*aatEx27*	*myo-3p::unc-49(C)::sl2::egfp; unc-49 (lf/ko) tm5487 III*	Microinjected 30 ng/uL *myo-3p::unc-49C::sl2::egfp* (pLD26); 70 ng/uL *pBlueScript* into TM5487 *[unc-49 (lf/ko) tm5487]III*	Rescue of UNC-49 and expression of eGFP in body-wall muscle
TOL52	*aatEx28*	*unc-25p::unc-49C::sl2::egfp, unc-49 (lf/ko) tm5487 III*	Microinjected 30 ng/uL *unc-25p::unc-49C::sl2::egfp* (pLD20); 70 ng/uL *pBlueScript* into TM5487 *[unc-49 (lf/ko) tm5487]III*	Rescue of UNC-49 and expression of eGFP in D-motoneurons
TOL56	*aatEx31*	*del-1p::unc-49 subunit C::sl2::egfp, unc-49 (lf/ko) tm5487 III*	Microinjected 50ng/uL *del-1p::unc-49 subunit C::sl2::egfp* (pLD32); 50ng/uL *pBluescript* into TM5487 *[unc-49 (lf/ko) tm5487]III*	Rescue of UNC-49C and expression of eGFP in VA and VB motoneurons

3.2.4 Identification of motoneurons in the ventral nerve cord

We used three methods for motoneuron identification. First, without co-expression of other fluorescent proteins, we identified the motoneurons in the ventral nerve cord by their number and position during developmental stages. Second, with co-expression of identification markers, we identified motoneurons by known expression of fluorescent

markers in the ventral nerve cord. The identification fluorescent markers we used were *unc-4p::mCherry* expressing in VA and DA motoneurons (Lickteig et al., 2001), *unc-25p:: Cerulean* expressing in GABAergic motoneurons (Jin et al., 1999), *del-1p::wrmScarlet* expressing in VA and VB motoneurons (Tavernarakis et al., 1997). Third, we compared the expression of green eGFP in a multicolor identification strain, namely NeuroPAL. In an adult NeuroPAL animal, VD expresses blue fluorescence, DD blue and week green, VA red, DA green and red, VB red and weak blue, DA green and red, and DB green, red and weak blue.

3.2.5 Microscopy

We anesthetized and mounted animals on glass microscope slides with 36% Pluronic F-127 (that is liquid on ice but turns solid at room temperature) with 1mM tetramisole (a nematode specific nicotinic blocker). We acquired fluorescence images and volume stacks with a laser scanning confocal microscope (Leica SP8 with LAS X software). We reconstructed maximum intensity projections with ImageJ software (imagej.nih.gov). For one image (Figure 3.4a) We used an epifluorescence compound microscope (Olympus IX73) to acquire tiled images and stitched them to a single image with CorelDRAW (2018).

3.2.6 Free swimming behavior assay

Free Swimming Behavior Recording. We recorded swimming behavior of wild type (N2), *unc-49* knockout strain (TM5487), and UNC-49 rescued strains (TOL51, TOL52, and TOL56) in NGM buffer using a static multi-worm tracker. The tracker was composed of three major parts from top to bottom: a camera (Basler ace acA4024-29um) connected with a fixed focal length lens (C Series 5MP 35mm 2/3" fixed focal length lens, Edmund Optics) with an infrared cut-off filter (M25.5 x 0.5 Mounted IR Cut-Off Filter, Edmund Optics); a

specimen stage for plates or slides; and an infrared LED light (M850L3, Thorlabs) mounted with a collimation adaptor (COP1-B-Collimation Adaptor, Thorlabs).

One day before the tracking, we transferred fourth larval stage (L4) animals to new NGM plates with healthy OP-50-1 *E. coli* bacterial lawn. To focus on motoneuron-specific rescue in the strains TOL52 and TOL56, we picked only animals without green fluorescence in body-wall muscle cells under a fluorescence stereomicroscope (Leica MZ16 FA). During tracking, at least 30 animals were freely swimming in NGM solution between a microscopic slide and a coverslip 1 mm apart. We recorded at least 9 videos (with Pylon-Viewer from Basler pylon Camera Software Suite) at 25 frames per second (fps) for 15 to 20 s. During acquisition, we cropped video frame dimensions to around 2,000x2,000 pixels. For swimming behavior tracking of N2, the numbers of videos, animals, and data points were 10, 207, 57745, respectively; for TM5487 the numbers were 9, 204, 60669; for TOL51 the numbers were 10, 219, 63819; for TOL52 the numbers were 10, 213, 71676; for TOL56 the numbers were 11, 264, 81318.

Behavioral Tracking Analysis. We processed tracking videos with a multi-worm behavior tracker software (Tierpsy Tracker v1.4.0, https://github.com/ver228/tierpsy-tracker/releases/) (Javer et al., 2018). Tierpsy generates hdf5 files that we analyzed with custom programs written in Matlab. We measured translocation speed and undulation frequency during forward and backward locomotion. Tierpsy computes the undulation frequency using the waveform frequency from the largest peak at the midbody via the Fourier transform over a time window. We collated the means of these parameters from individual animals from all the videos, and then used one-way ANOVA and post-hoc Tukey's multiple comparison test to compare the estimated population means among

strains or different conditions. We plotted scatter plots, histograms and box plots to visualize the data distribution with Matlab and CorelDraw.

3.3 Results

3.3.1 Subunits of UNC-49 ionotropic GABA receptor expressed in GABAergic motoneurons

To identify the cells that express UNC-49 subunits, we constructed plasmids in which *sl2*::*eGFP* cassette fused after UNC-49 subunits. Here, *sl2* is a trans-splicing sequence that allows translation of soluble eGFP released into the cytoplasm, facilitating cell identification. We used two methods for cell identification of motoneurons expressing UNC-49 receptor subunits and eGFP: one was taking advantage of different numbers of motoneuron subsets on the first larval stage, and the other using the multicolor identification strain NeuroPAL in which subsets of motoneuron express unique color combinations (a generous gift from Oliver Hobert and Eviatar Yemini pre-publication).

For the first method, we imaged L1 animals of three transgenic strains (TOL39, TOL65, TOL40; n= 3, 3, 5) which express constructs UNC-49A/B/C::sl2::eGFP by native promoter *unc-49p*, respectively. We found the expression of eGFP in body-wall muscles as expected, and in motoneurons. Only 22 ventral cord motoneurons can be found in L1 animals: 9 DAs, 7 DBs, and 6 DDs, and motoneuronal identity can be deduced from the number of expressing neurons. The six neurons that express eGFP in the ventral nerve cord of L1s suggested that these neurons might be DD motoneurons (Figure 3.2). To further identify these neurons, we used the second method. We imaged the adult animals of three transgenic strains (TOL62, TOL63, TOL61; n=6, 6, 3) which express the constructs UNC-49A/B/C::sl2::eGFP by *unc-49p,* restively, and unique colors in different subsets of

motoneurons from NeuroPAL. We found eGFP expressing in body-wall muscle cells as formerly reported (Figure 3.3 left panels). Moreover, by comparing expression of eGFP and the different colors expressed in NeuroPAL motoneurons and taking into account motoneuronal position along the ventral nerve cord, we found that eGFP (hence UNC-49A, B, and C) expressed in VD and DD motoneurons (Figure 3.3 right panels). In addition, we occasionally found expression of eGFP in VA and AS (VA05 in one TOL63 and AS02 in one TOL61).

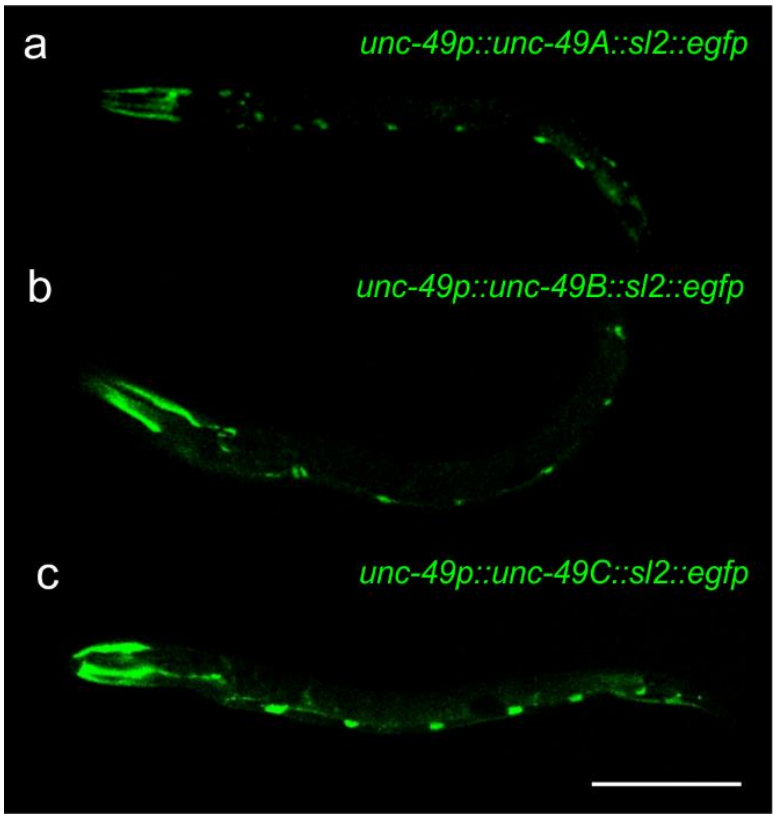

Figure 3.2 UNC-49 subunits A, B and C expressed in 6 motoneurons in newly hatched larvae. The expression of green fluorescent reporter (unc-49p::unc-49A/B/C::sl2::egfp) in 6 motoneurons in L1 larvae suggests the expression of UNC-49 subunits limited to DD because L1 larvae have only 6 DD, 7 DB, and 9 DA motoneurons. The transgenic strains TOL39 (a), TOL65 (b) and TOL41 (c) express the subunits UNC-49A/B/C respectively as well as eGFP under the native promoter *unc-49p.* Note some expression in other head and tail neurons and in head muscle. Scale bar = 50 μm.

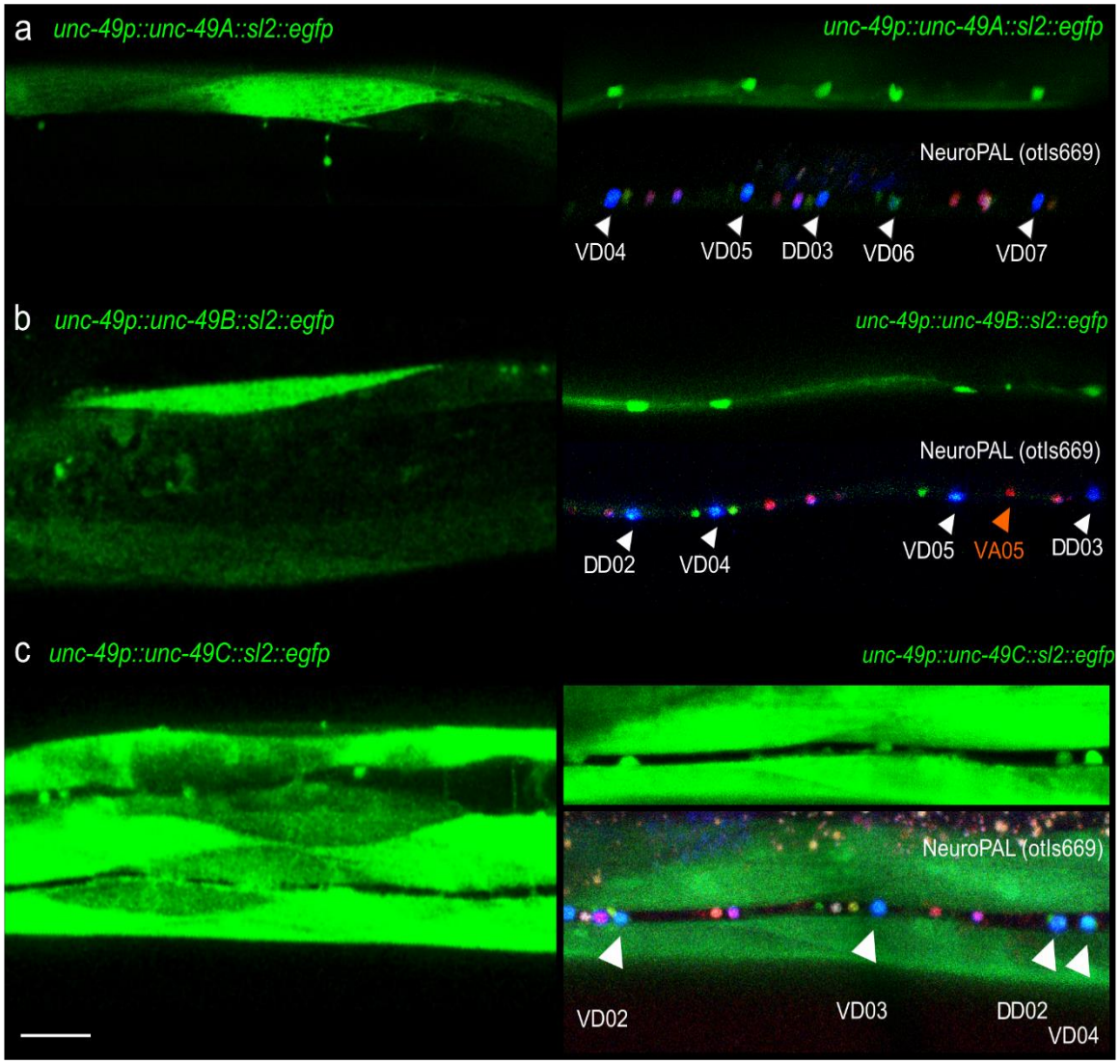

Figure 3.3 UNC-49 subunits A, B, and C expressed in body-wall muscles (left panel) and GABAergic motoneurons (right panel). The transgenic NeuroPAL strain in which each neuronal class is uniquely identified by color is designed for neuron identification. In the adult animals, VD expressed blue fluorescence, DD blue and week green, VA red, DA green and red, VB red and weak blue, and DB green, red and weak blue. The transgenic strains TOL62 (a), TOL63 (b) and TOL61 (c) express the subunits unc-49A/B/C respectively as well as eGFP under the native promoter *unc-49p* in NeuroPAL strain. Fluorescent reporter eGFP (hence UNC-49 subunits) expressed in body-wall muscles (left panel) and colocalized with VD and DD motoneurons in NeuroPAL (right panel). eGFP in one TOL63 (b) colocalized with VA05 motoneuron. Scale bar = 20 µm.

3.3.2 UNC-49 native promoter drove gene expression in body-wall muscles, GABAergic, and ventral cholinergic motoneurons

The counting and NeuroPAL methods demonstrated that UNC-49 subunits A, B, and C express in GABAergic motoneurons and muscle cells, and occasionally UNC-49B expressed in VA motoneuron. Indeed, the published connectivity dataset, as well as our own results in Chapter 2, suggest postsynaptic inhibitory connections from VD to ventral cholinergic motoneurons. However, no transcriptional expression of promoter u*nc-49p* in GABAergic and ventral cholinergic motoneurons were reported.

Therefore, we used green fluorescent reporter GFP or eGFP to take a closer look at the transcriptional expression of the native upstream promoter (*unc-49p::gfp/egfp*) with three identification methods. First, we looked at the expression of eGFP alone without identification markers in adults and L1 animals (TOL40, n>50), and found eGFP expressing in motoneurons in 3 adults and 1 L1 animal (Figure 3.4ab). Second, we looked at the expression of green fluorescence in NeuroPAL (TOL64, n>150), and only found 1 lava expression green fluorescence in two motoneurons. NeuroPAL is not accurate in neuron identification in animals earlier than the third larval stage, so we were unable to identify these motoneurons. Third, we compared the expression pattern of GFP with that of the class-specific markers for DA and VA motoneurons (*unc-4p::mCherry)* in a transgenic strain (UL4020, n=4). We found GFP expressing in body-wall muscles and motoneurons, and the red fluorescent protein mCherry expressing in motoneurons. There was co-localization of GFP and mCherry in some motoneurons, but there were some motoneurons expressing GFP only and some expressing mCherry only (Figure 3.4c). In another transgenic strain (TOL29, n=4) with class-specific markers in GABAergic (*unc-25p::Cerulean)* and ventral cholinergic VA and VB motoneurons (*del-1p::wrmScarlet),*

we found co-expression of eGFP with a cyan fluorescent protein (cerulean) that expressed in GABAergic motoneurons or with a red fluorescent protein (wrmScarlet) that expressed in VA and VB motoneurons (Figure 3.4d, n=4 animals).

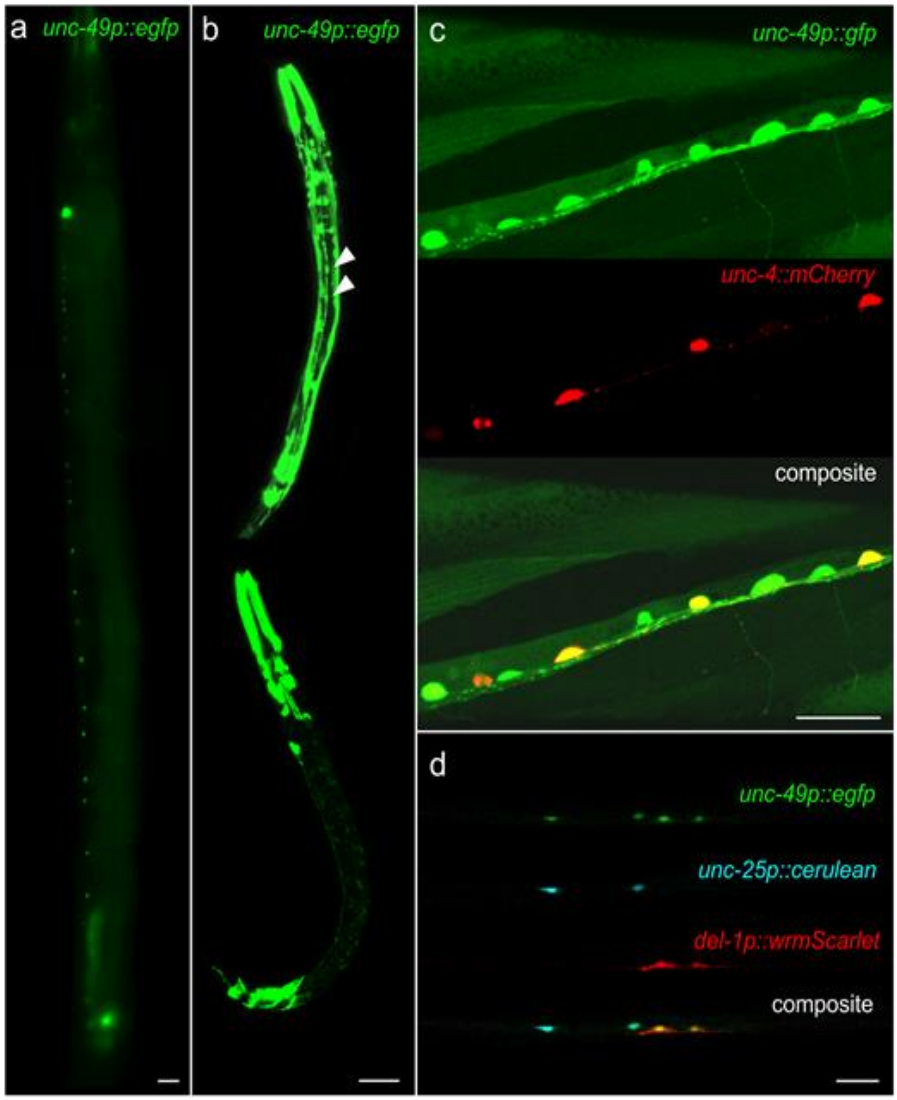

Figure 3.4 Promoter *unc-49p* initiated transcription in GABAergic motoneurons as well as VA and VB motoneurons. (ab) Under promoter *unc-49p* (transgenic strain TOL40), eGFP commonly expressed in body-wall muscles and a single non-neuronal knot close to the head. Occasionally eGFP was expressed in motoneurons in some adult (a) and L1 (b) animals. (c) A similar transgenic strain (UL4020) drove expression of GFP in body-wall muscle cells and motoneurons, and mCherry in cholinergic VA and DA motoneurons (*unc-4p::mCherry*). GFP co-localized with a majority of the mCherry expressing motoneurons. (d) In another transgenic strain (TOL29) eGFP encoded under the promoter *unc-49p* co-localized with either blue fluorescent cerulean (in GABAergic motoneurons, *unc-25p::cerulean*) or red fluorescent wrmScarlet (in VA and VB motoneurons, *del-1p::wrmScarlet*). Scale bars = 20 µm.

3.3.3 Tissue-specific rescue of UNC-49 expression in body-wall muscle exhibited more recovery of swimming behavior than rescue in GABAergic and ventral cholinergic motoneurons

According to our and others' transcriptional and translational expression patterns, and the GABAergic synapses in the published connectivity dataset, UNC-49 subunits of the ionotropic GABA receptor express in body-wall muscle cells, in GABAergic motoneurons, and may also express in VA and VB motoneurons. In Chapter 2, we show that in the absence of *unc-49* gene animals exhibit only slow undulatory locomotion. Here we examine the contribution of UNC-49 subunits and inhibitory synapses onto body-wall muscle cells, GABAergic motoneurons, and ventral cholinergic motoneurons to rapid swimming behavior. We transgenically rescued the gene *unc-49* in a tissue-specific manner in body-wall muscles (with *myo-3p::unc-49::sl2::egfp*; TOL51), in GABAergic motoneurons (with *unc-25p::unc-49::sl2::egfp*; TOL52), and in VA and VB motoneurons (with *del-1p::unc-49::sl2::egfp*; TOL56), in a *unc-49* knockout strain. While muscle-specific rescue expression (visualized with eGFP) was restricted to muscle cells, we saw the expression in muscle cells in the motoneuron-specific rescue animals (Figure 3.5). In ventral-cholinergic-motoneuron rescue animals, we saw eGFP expression in other motoneurons that according to their number and position might be GABAergic motoneurons (Figure 3.5a).

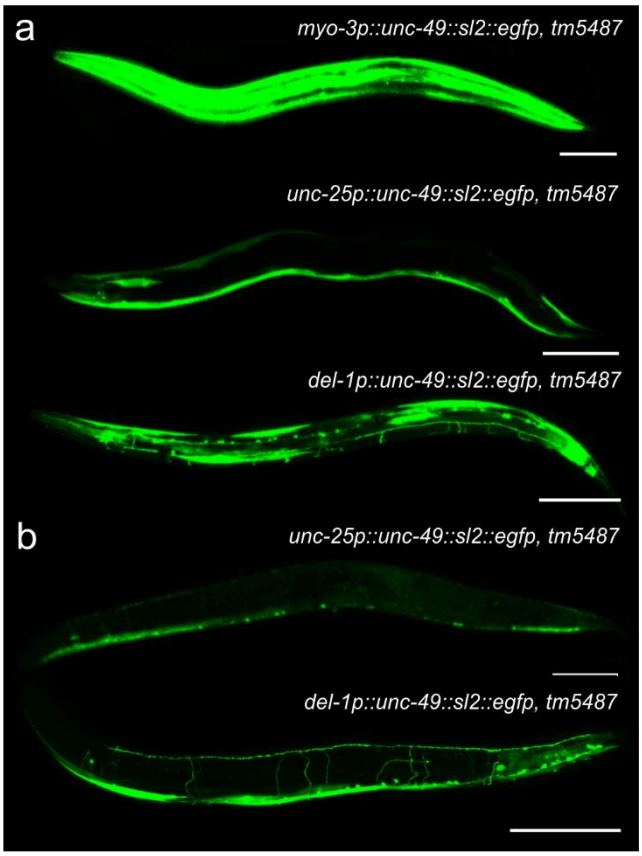

Figure 3.5 Green fluorescent protein marked tissue-specific-rescue in *unc-49* knockout animals. (a) eGFP (and hence UNC-49) expressed only in body wall muscle cells under promoter *myo-3p* (TOL51, top); expression under promoter *unc-25p* was localized in GABAergic motoneurons but included unintended protein expression in body-wall muscle cells (TOL52, middle); expression under promoter *del-1p* was localized in VA and VB motoneurons but included unintended protein expression in body-wall muscle cells and putative GABAergic motoneurons (TOL56, bottom). (b) Only the transgenic animals (top: TOL52, bottom: TOL56) that had little green fluorescence in body-wall muscles were assayed for rescue of swimming behavior. Scale bars = 100 μm.

To study contributions of UNC-49 to rapid undulatory locomotion we tracked swimming behavior of tissue-specific rescued animals (n>30 in each stain, Figure 3.5b). To isolate motoneuron-specific rescue we selected animals without eGFP expression in muscle. During forward swimming, the mean translocation speeds of wild type, *unc-49* knockout, muscle-specific rescue, GABAergic motoneuron-specific rescue and ventral cholinergic motoneuron specific rescue were 389±121 μm, 76±55 μm, 282±88 μm, 171±72

μm, 159±64 μm, respectively; their mean undulation frequencies were 1.6±0.28 Hz, 0.58±0.44 Hz, 1.23±0.21 Hz, 0.94±0.28 Hz, and 0.82±0.35 Hz, respectively. During backward swimming, their mean translocation speeds were -403±117 μm, -69±22 μm, -283±53 μm, -158±45 μm, and -145±26 μm, respectively; their mean undulation frequencies were 1.20±0.43 Hz, 0.52±0.31 Hz 1.12±0.28 Hz, 0.87±0.50 Hz 0.76±0.16 Hz, respectively. Compared to the *unc-49* knockout strain, all tissue-specific rescue strains showed significant increases in translocation speed ($p<0.001$) and undulation frequency ($p<0.001$) during forward and backward swimming. Compared to wild type, they showed significantly lower translocation speed ($p<0.001$) and undulation frequency ($p<0.001$) during forward and backward swimming, except that the undulation frequency of muscle-specific rescue during backward swimming was not statistically different from that of wild type ($p=0.99$). Hence UNC-49 expression in body-wall muscle cells, GABAergic motoneurons, or VA and VB motoneurons conveyed a partial recovery of swimming. Within these tissues, the expression in body-wall muscle cells conveyed the highest degree of recovery, and its undulation frequency during backward swimming was not statistically different from that of wild type (Figure 3.6).

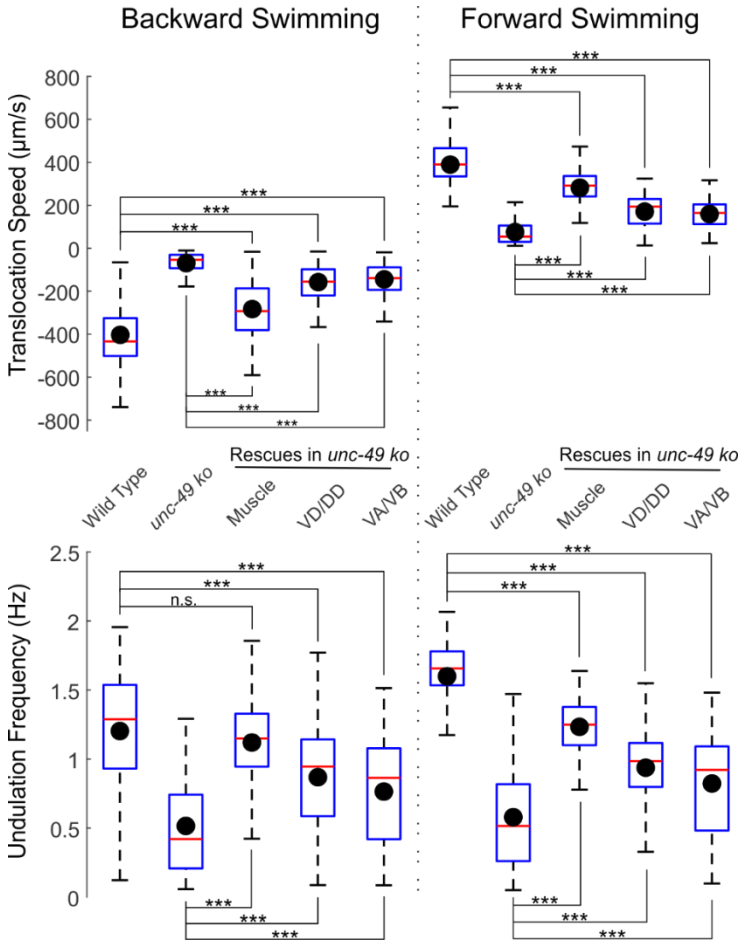

Figure 3.6 Transgenic expression of UNC-49 receptor in specific tissue of *unc-49* knockout animals partially rescued swimming behavior. Animals transgenically expressing UNC-49 and eGFP in body-wall muscles (TOL51), VD and DD motoneurons (TOL52), and VA and VB motoneurons (TOL56) had different degree of recovery of translocation speed and undulation frequency in either direction of swimming. Specific rescue in body-wall muscle cells exhibited the most recovery. Estimated population means of translocation speed and undulation frequency of all rescued strains in either direction of swimming were significantly higher than those of *unc-49* knockout (TM5487), but significantly lower than those of wild type (N2), except for the undulation frequency of muscle-specific rescues during backward swimming that exhibited complete rescue and not different from wild type. Blue boxes indicate the first and the third quartiles of dataset; black dots represent mean values; red lines indicate medians; black whiskers indicate minimum and maximum excluding outliers (beyond 1.5 times of interquartile range from the first and the third quartiles). Statistical test is ANOVA with Tukey's multiple comparison, n.s. $p>0.05$, *** $p<0.001$.

3.4 Discussion

3.4.1 GABA ionotropic receptor UNC-49 expresses in GABAergic motoneurons and other motoneurons besides body-wall muscles

The GABA ionotropic receptor UNC-49 had been studied for over 20 years, its expression has been reported only in body-wall muscle cells. One of the reasons is that researchers used reporters fused to the protein for identification. They inserted fluorescent proteins (e.g. GFP or YFP) to the end of the last exon of GABA receptor subunits and found fluorescence expression along the ventral and dorsal nerve cord, as well as in muscle cells and muscle arms (Bamber et al., 1999; Gally and Bessereau, 2003; Bamber et al., 2005; Maro et al., 2015). However, the expression of the fluorescent reporter reported in the nerve cord cannot exclude the possibility of their existence at the dendrites of the postsynaptic motoneurons, because the synaptic cleft of the neuromuscular junction and that of the motoneurons all located in the nerve cord. Therefore, for a fused protein, such as UNC-49C::GFP, it is hard to distinguish between fluorescent reporter expression at the postsynaptic sites of muscle arms or motoneurons. The other reason is that the native upstream promoter *unc-49p* by itself mainly induces gene expression in the body-wall muscle cells. It was rare to find fluorescent reporter expression in motoneurons in the transgenic animals which had been injected with *unc-49p::egfp* without any identification markers. In the wild type animal, the native upstream promoter *unc-49p* may need an intron mediated enhancer or regulator to induce transcription in motoneurons. When we used other plasmids that included parts of the native gene sequence or other promoters with known expression patterns to help identify, we saw the expression of *unc-49p::gfp* easily in DD, VD, VA, and VB motoneurons (Figure 3.4cd). The regulator controlling transcription in GABAergic motoneurons may be in the *unc-49* gene. In the rescue animal

in which *unc-49* gene is not under the GABAergic motoneuron specific promoter, there was extra fluorescent reporter expression in GABAergic motoneurons. Gene *unc-49* may also contain a sequence that can initiate transcription in body-wall muscle cells (in particular ventral muscle cells), as in the motoneuron-specific rescue animals there was extra protein expression in body-wall muscles.

The expression patterns induced by UNC-49 subunits are more consistent. We looked at the expression of UNC-49A, UNC-49B and UNC-49C (including UNC-49Cshort) by microinjecting *unc-49p::unc-49A/B/C::sl2::egfp* into wild type and NeuroPAL strain, and confirmed their expressions in GABAergic motoneurons in L1 larvae and adults (Figure 3.2 and 3.3). In addition, UNC-49 subunits occasionally express in other motoneurons such as VA and AS motoneurons.

3.4.2 GABA ionotropic receptor UNC-49 in neuromuscular junctions contributes the most to rapid dorsoventral alternation

Cross-inhibition was suggested to underlie backward undulatory locomotion in *C. elegans* (McIntire et al., 1993b; Schuske et al., 2004). In Chapter 2 we suggest other roles for inhibition from GABAergic motoneurons. The GABAergic neuromuscular junction can support cross-inhibition of opposing muscles, as well as disinhibition in which removal of inhibition sharpens and enhances muscle activation. The GABAergic synapse from VD to VA and VB motoneurons could temporally modulate the undulation cycles by inhibiting the ventral cholinergic motoneurons before the end of the ventral activation phase, which terminates the present cycle early and shorted each cycle. Ventral GABAergic (VD) motoneurons innervate their dorsal counterparts (DD) and vice versa according to the connectivity dataset based on electromicrographs (White et al., 1976; Haspel and

O'Donovan, 2011). Yet the roles of these connections are unknown; they might reinforce the antiphasic activity of the GABAergic motoneurons during rapid locomotion.

We demonstrated the necessity of GABAergic motoneurons to sustaining fast undulatory locomotion in Chapter 2. Rapid locomotion of *C. elegans*, in particular swimming behavior, is impaired when GABA transmission is defective or GABAergic neurons are inactivated. Here we demonstrated that the ionotropic $GABA_A$ receptor UNC-49 is expressed in GABAergic motoneurons and putative VA and VB motoneurons, as well as body-wall muscle cells. Hence, these tissues receive GABAergic chemical synapses, indicating that UNC-49 may play inhibitory roles in these compartments to support fast undulatory locomotion. To test the inhibitory contribution of UNC-49, we rescued the receptor in specific tissues: the body-wall muscle cells, the GABAergic motoneurons, and the ventral cholinergic motoneurons, in an *unc-49* knockout strain and assayed the change of their swimming behavior. The specific rescue in body-wall muscle cells had the highest degree of behavior recovery, suggesting that UNC-49 plays its most important role in providing inhibition to body-wall muscle cells that underlies cross-inhibition, disinhibition, or both. The inhibitory role of the synapses between ventral and dorsal GABAergic motoneurons and those from VD to VA and VB motoneurons are less conclusive because the effects of the tissue-specific rescues are smaller and because we observed unintended expression in body-wall muscle cells in the rescue strains. For our assays, we picked animals without visible fluorescence in body-wall muscle cells, but we cannot exclude the possibility that small amounts of UNC-49 were expressed in the muscle.

To sum, we demonstrated the expression of the $GABA_A$ receptor UNC-49 in motoneurons (mainly in GABAergic motoneurons) as well as the formerly known

expression in body-wall muscles. In these postsynaptic locations, UNC-49 may play several roles in *C. elegans* locomotion, most prominently the receptors in body-wall muscles to support rapid dorsoventral alternation of activity.

CHAPTER 4

CONCLUSION AND DISCUSSION

4.1 Main Results

4.1.1 Main results of Chapter 2: Inhibition underlies fast undulatory locomotion in *C. elegans*

We studied the roles of inhibition in the locomotion circuit of *C. elegans* by behavioral tracking, calcium imaging of neuronal and muscular activity in undulating intact animals, and by testing possible mechanisms with two computational models. First, we re-evaluated the shrinking phenotype which had been a signature phenotype of the transgenic mutants defective in GABA transmission. We harshly touched the head or tail of wild type and GABA transmission knockout animals during their forward crawling and measured their body length change compared to their pre-stimulus value. We identified the shrinking phenotype not only in response to head touch in the GABA transmission knockout animals as previously reported, but also in wild type animals, and regardless of locomotion direction. In particular, wild type shrank less and recovered to their pre-stimulus body length sooner, as well as crawled away from the stimulation with higher translocation speed and undulation frequency. Furthermore, we carried out the similar harsh-touch stimulation experiments on *vab-7* and *unc-4* mutant animals in which forward and backward locomotion are impaired due to defects in B-type and A-type cholinergic motoneuron differentiation, respectively. We triggered their directional locomotion that is unaffected by the mutation and measured their body length. The body shrinkage of these two mutants was not statistically different from that of wild type, suggesting that the shrinking phenotype is caused by co-activation of dorsal and ventral A- or B-type cholinergic

motoneurons, rather than the co-activation of A- and B-type cholinergic motoneurons. Second, we tracked the free bidirectional crawling and swimming of wild type, GABA transmission knockout animals, and an optogenetic strain in which GABAergic motoneurons can be acutely inhibited by light. When GABA transmission was taken away chronically or acutely, the animal's dorsoventral alternation frequency decreased, resulting in lower translocation speed. During both crawling and swimming, the undulation frequency correlated to translocation speed in wild type and GABA transmission knockout strains. Third, we recorded the cellular activity of GABAergic motoneurons and body-wall muscles in non-GABA transmission animals. GABAergic motoneurons' activity pattern was different during low and high undulation frequency. During low undulation frequency, VD and DD exhibited similar activity patterns; while during high undulation frequency, their activity alternated. Fourth, following the experimental results, we suggested and computationally tested three hypotheses for the inhibitory mechanism that supports high-frequency undulation. Our modeling results suggested that cross-inhibition and disinhibition of the body-wall muscles contribute to high-frequency undulations in a proprioceptive-driven network, while in a CPG-like network these inhibitory mechanisms do not make a difference. Finally, we suggested that the unimpaired locomotion circuit produces an undulatory motor program by two distinct modes of operation for low and high-frequency undulations.

4.1.2 Main results of Chapter 3: An ionotropic GABA receptor, expresses in motoneurons and muscle and functions in *C. elegans* locomotion

UNC-49 is an inhibitory ionotropic $GABA_A$ receptor with several subunits coded as alternative splicing of the gene. Of these, only subunits UNC-49B and UNC-49C had been located and both expressed only in body-wall muscles (Bamber et al., 1999; Bamber et al.,

2005). We re-evaluated the cellular expression of the receptor subunits UNC-49A/B/C by describing the expression of soluble cytoplasmic eGFP (spliced-off the mRNA with the trans-splicing leader *sl2*, [*unc-49p::unc-49A/B/C::sl2::egfp*]) and a transcription reporter that is driven by the native promoter [*unc-49p::egfp*]. We used three motoneuron-identification methods: taking advantage of the small and distinct number of motoneurons of each class in newly hatched animals, an identification strain NeuroPAL in which different types of motoneurons express a different set of fluorescent proteins, and motoneurons-specific identification markers. We found that in the adult nematode UNC-49A/B/C expressed in body-wall muscle (as previously reported), in GABAergic motoneurons, and occasionally in VA and VB motoneurons. Furthermore, to test the contribution of UNC-49 in these tissues to support fast locomotion, we used tissue-specific promoters to transgenically rescue the expression of UNC-49 in either body-wall muscle cells, GABAergic motoneurons, or VA and VB motoneurons, in *unc-49* knockout mutants and assayed their swimming behavior. Animals that expressed UNC-49C in body-wall muscles (but not motoneurons) exhibited the most pronounced recovery of rapid undulatory locomotion, suggesting that the main function of UNC-49 in locomotion is to mediate inhibition of body-wall muscle.

4.2 General Discussion

This dissertation challenges the prevalent hypothesis that cross-inhibition mediates backward locomotion in *C. elegans*. GABAergic D-type motoneurons in the ventral nerve cord of *C. elegans* synapse onto body-wall muscles (White et al., 1976). Their inhibitory effect to body-wall muscles was confirmed through multiple methodologies: laser ablating

D-type motoneurons, electrophysiology recording with GABA bathing or pulses, and activating GABAergic D-type motoneurons optogenetically (McIntire et al., 1993b; Bamber et al., 2005; Gao and Zhen, 2011; Inoue et al., 2015). Because of the determined inhibitory effect of GABAergic D-type motoneurons and the connectivity of the neural circuit in the ventral nerve cord as well as the shrinking phenotype of GABA transmission mutants, it was believed that cross-inhibition is necessary for backward undulatory movement in *C. elegans*. According to this hypothesis, for example, when the ventral excitatory cholinergic motoneurons are activating the ventral side of body-wall muscles, they activate the dorsal inhibitory GABAergic motoneurons to relax the muscles on the dorsal side. However, when we analyzed the locomotion behavior of mutant strains that are defective in different parts of GABA transmission, we found that these strains can perform forward and backward crawling during free locomotion and after stimulation, but with lower translocation speed and undulation frequency. This suggests that cross-inhibition is not necessary for undulatory locomotion in *C. elegans* but is instead crucial for rapid dorsoventral alternation. We were the first to record the cellular activity of these GABAergic D-type motoneurons during different undulation frequencies. Our results for both low and high undulation frequencies show that GABAergic motoneurons interact differently in low and high undulation frequency. The dorsal and ventral D motoneurons alternate their activity and possibly provide alternating inhibition or disinhibition during high undulation frequency, while in low undulation frequency the dorsal and ventral D motoneuron show similar patterns of activity with a wide inactive phase that might allow their innervated body-wall muscle to follow the activation pattern of excitatory motoneurons. Finally, in collaboration with the Cohen laboratory (of Leeds University),

we tested three roles of inhibition in a proprioceptive mechanical control model and a feedforward control model. Taken together, this study introduces two main novel aspects. First, we studied bidirectional locomotion rather than a single locomotion direction. We are the first to describe the shrinking phenotype caused by either head or the tail harsh touch stimulation in both wild type and GABA transmission mutant animals, as well as slow locomotion in both forward and backward locomotion while inhibition is impaired. Second, we study the neuronal activity in different undulation frequencies. Published calcium imaging results in any *C. elegans* neurons were primarily obtained from low undulation frequency and are presented against time (Chronis et al., 2007; Chung et al., 2013; Venkatachalam et al., 2016; Gao et al., 2018; Kagawa-Nagamura et al., 2018). In contrast, our calcium imaging results describe the signal change within an undulation cycle against the locomotion phase, collected from multiple animals and cells, in both low and high undulation frequency.

We also complete the expression identification of UNC-49 subunits. Formerly, only the expression patterns of UNC-49B and UNC-49C subunits were determined to be in body-wall muscles, and no UNC-49 subunit was reported in motoneurons. One of the possible reasons is that researchers used fusion protein for identification. They attached fluorescent protein such as GFP or YFP to the end of the last exon of UNC-49 subunits and found fluorescent proteins expressing along the ventral nerve cord, which colocalized with the neuromuscular junction between motoneurons and muscle arms of body-wall muscles (Bamber et al., 1999; Gally and Bessereau, 2003; Bamber et al., 2005; Maro et al., 2015). Since the synapses between motoneurons are also located in the ventral nerve it is hard to distinguish whether the fluorescent reporter expresses at the postsynaptic muscle arms or

postsynaptic motoneurons. Another reason is that even in our hands the promoter *unc-49p* by itself mainly promotes gene expression in the body-wall muscles. We only observed several out of hundreds of cases in which the transcriptional reporter (*unc-49p::eGFP*) expressed in motoneurons. However, when the transcriptional reporter co-expressed with other identification markers, it expressed in GABAergic and ventral cholinergic motoneurons.

This study of the inhibitory GABAergic motoneuron and UNC-49 inhibitory ionotropic receptor demonstrates the importance of inhibition in rapid motor output. When inhibition is taken away, *C. elegans* will fail to produce rapid dorsoventral body-wall alternation. Inhibitory motoneurons may play different roles to enhance the amplitude of undulation through cross-inhibition, to enhance and sharpen the initial rising phase of a bend via disinhibition, and to advance the next cycle through an inhibitory reset. Inhibitory ionotropic receptors take part to fulfill the inhibitory roles at the postsynaptic body-wall muscles or motoneurons. Other than in locomotion, inhibition and regulation play important roles in speeding up processes in very disparate fields. For example, rule-of-way and traffic lights can increase efficiency and the overall rate of movement for pedestrian dynamics, vehicle traffic, logistics, public transportation, social dynamics, ecological systems, and adaptation by modulating individual performance to overall speed up the complex systems (Gershenson and Helbing, 2015). Negative autoregulation, in which a gene product plays as a repressor of their transcription, speeds up the response time of gene circuits making it reach an earlier steady-state, while also promoting robustness to fluctuations in gene production rate (Alon, 2007).

Counterintuitively, inhibition does not stop or slow down systems. Instead, it plays important roles in modulating dynamical systems by sharpening excitatory signals both spatially and temporally, as well as filtering out unwanted or redundant signal. In *C. elegans*, and probably in other animals one can only go so fast without inhibition.

APPENDIX A

EXPERIMENTAL OPTIMIZATION IN CALCIUM IMAGING, LARGE PLASMID CONSTRUCTION AND MOTONEURON IDENTIFICATION

In Appendix A, we elaborate on experimental approaches in developing two-channel calcium imaging, technical details and a protocol for constructing large plasmids for transgenic manipulations, and technical details for using multicolor fluorescent strains for motoneuron identification. In the first chapter, besides recording calcium imaging signal from GCaMP alone, we also tried to improve the signal to noise ratio by introducing a reference protein. In the second chapter, we constructed large plasmids for identification of UNC-49 and its subunits, as well for rescuing GABA ionotropic receptor UNC-49 in different subsets of cells involved in undulatory locomotion. In addition, to identify motoneurons, we used identification strains NeuroPAL that have a unique combination of fluorescent proteins in each neuronal class.

A.1 Synchronized Two-channel Calcium Imaging

In Chapter 1 we used GCaMP, a genetically encoded calcium sensor, alone for activity imaging in the microfluidic waveform channel. In an effort to increase the signal to noise ratio and control for movement artifacts, we introduced a calcium insensitive reference fluorescent protein. We recorded the fluorescence signal from both the calcium sensor and reference protein and calculated the ratio of fluorescent intensity signals. Unfortunately, the reference protein we chose were two bright fluorescent proteins, the green eGFP (Cormack et al., 1996) and red wrmScarlet (El Mouridi et al., 2017). Because of their high intensity, their signal changes were too big, in comparison with the calcium signals, to be

used as a reference. They also induced bleed-through into the calcium sensor channel, causing an interference.

In this section, we summarize the approach and attempts of two-channel calcium imaging, elaborate on possible pitfalls, and detail a protocol for synchronized two-channel calcium imaging with microfluidic devices for future experiments.

A.1.1 Strains used for two-channel calcium imaging

We used eGFP and wrmScarlet as reference proteins for RCaMP and GCaMP, respectively, in three transgenic strains for the two-channel calcium imaging. These three strains are TOL43 (*aatEx25 [myo-3p::nls::RCaMP2; myo-3p::nls::eGFP; pha-1(+); pha-1(lf) e2123 III]*), TOL45 (*aatIs1[unc-25p::GCaMP6s; unc-25p::wrmScarlet; pha-1(+); pha-1(lf) e2123 III]*) and TOL48 (*aatIs8 [acr-2p::GCaMP6s; acr-2p::wrmScartlet]*). TOL43 has red calcium sensor RCaMP2 and green calcium insensitive fluorescent protein eGFP in nuclei of body-wall muscles. We generated TOL43 by microinjecting 50 ng/uL *myo-3p::nls::RCaMP2* (pLQ1), 25 ng/uL *myo-3p::nls::eGFP* (pLD28) and 25 ng/uL *pha-1(+)* (pBX) into GE24 *[pha-1(lf) e2123 III]*. TOL45 has green calcium sensor GCaMP6s and red calcium insensitive fluorescent protein wrmScarlet in GABAergic motoneurons. TOL48 has green calcium sensor GCaMP6s and red calcium insensitive fluorescent protein wrmScarlet in A and B motoneurons. We generated TOL45 by microinjecting 50 ng/uL *unc-25p::GCaMP6s* (pVM1), 25 ng/uL *unc-25p::wrmScarlet* (pLJ3) and 25 ng/uL *pha-1(+)* (pBX) GE24 *[pha-1(lf) e2123 III]*, and TOL48 by microinjecting 50 ng/uL *acr-2p::GCaMP6* (pLD5) and 50 ng/uL *acr-2p::wrmScarlet* (pLD11) into N2. We integrated the extrachromosomal arrays of TOL45 and TOL48 into the animals' genome via UV irradiation methods and backcrossed with wild type N2 for 5 generations (Ahringer, 2006).

The bright calcium insensitive proteins eGFP and wrmScarlet were much brighter than the calcium sensor. eGFP is around fivefold brighter than RCaMP2 and wrmScarlet is around tenfold brighter than GCaMP6s. The bright reference protein made the observation of fluorescent animals easy using a fluorescence stereomicroscope (Leica MZ16 FA); however, these bright reference proteins introduced experimental obstacles. Because of their high fluorescence intensity, it bled through into the calcium sensor channel at a level equivalent in intensity to the calcium signal. To sum, for future two-channel imaging experiments, the brightness intensity of the reference protein should be equivalent to that of the calcium sensor, or the dichroic mirror needs to be optimized to drastically reduce bleed-through.

A.1.2 Two-channel calcium imaging protocol using a microfluidic device

Synchronizing the cameras of two imaging channels at an acquisition rate of 100 frames per second (fps) turned out to be non-trivial. We combined advice from Hamamatsu representatives and an external advisor to use an Arduino controller under the micromanager software to provide a timing signal. Here, instead of describing my approach or the hardware, it is most useful for future readers that we provide a standard operating procedure (SOP) for recording fluorescent signals from two synchronized channels in animals moving through microfluidic waveform channels.

A. Device setup.

1. Turn on the general switch connected with OLYMPUS microscope, X-Cite 120 LED light, two Hamamatsu ORCA-Flash 4.0 cameras, and Arduino box. Make sure the status light of Hamamatsu ORCA-Flash 4.0 cameras is green.

2. Turn on Dell Precision Tower 7910.

3. Open Micro-Manager 2.0.0-beta. At Micro-Manager startup configuration, load Hardware Configuration ‘MMConfig_2Flash4-TwinCam_serial_TG-19-01-25’.

4. Check whether the view through eyepieces is in the same orientation as the view acquired by cameras. If not, go to ‘Image Flipper’ on Micro-Manager to rotate the image. (Plugins tab -> On-The Fly Image Processing -> Image Flipper.)

5. In ‘imaging setting’, set ‘Exposure [ms]’ to ~ 10 ms, and adjust ‘Binning’ if necessary. In ‘Configuration settings’, change ‘Camera-Trigger’ to ‘External’ and change ‘Trigger Mode’ to ‘start’ so that Micro-Manager will wait for acquisition orders from Arduino (Figure A.1a).

6. Click ‘Multi-D Acq.’ to open the ‘Multi-Dimensional Acquisition’ window. In ‘Time Points’ section, set ‘Count’ to the number of frames you want to acquire in each channel, and leave ‘Interval’ as 0 ms. In the ‘Save Images’ section, change ‘Directory root’ and ‘Name prefix’, and check ‘Separate image files’ as the ‘Saving format’ (Figure A.1b).

7. Open Arduino file ‘thom.ino’.

8. Click ‘Serial Monitor’ at the right top corner to open ‘COM3 (Arduino Genuino Uno)’ window (Figure A.2a).

9. On ‘COM3 (Arduino Genuino Uno)’ window, enter serial settings: Exposure duration [ms], Interval [ms], Number of frames. The highest acquisition frequency is 91 fps in this Arduino program (Serial setting: 10, 1, number of frames, Figure A.2b).

a

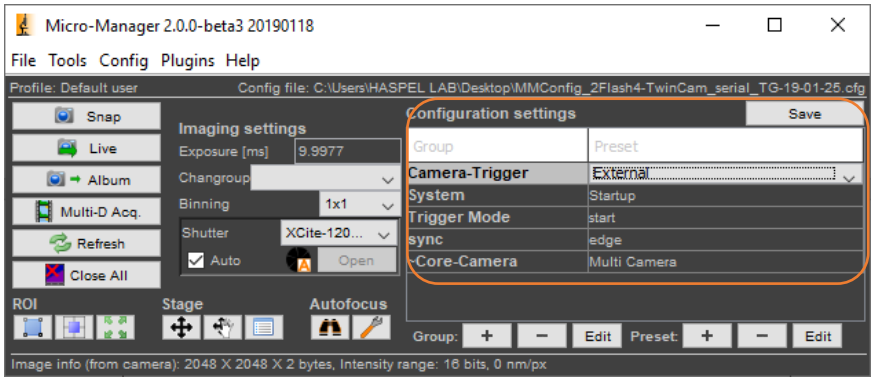

b

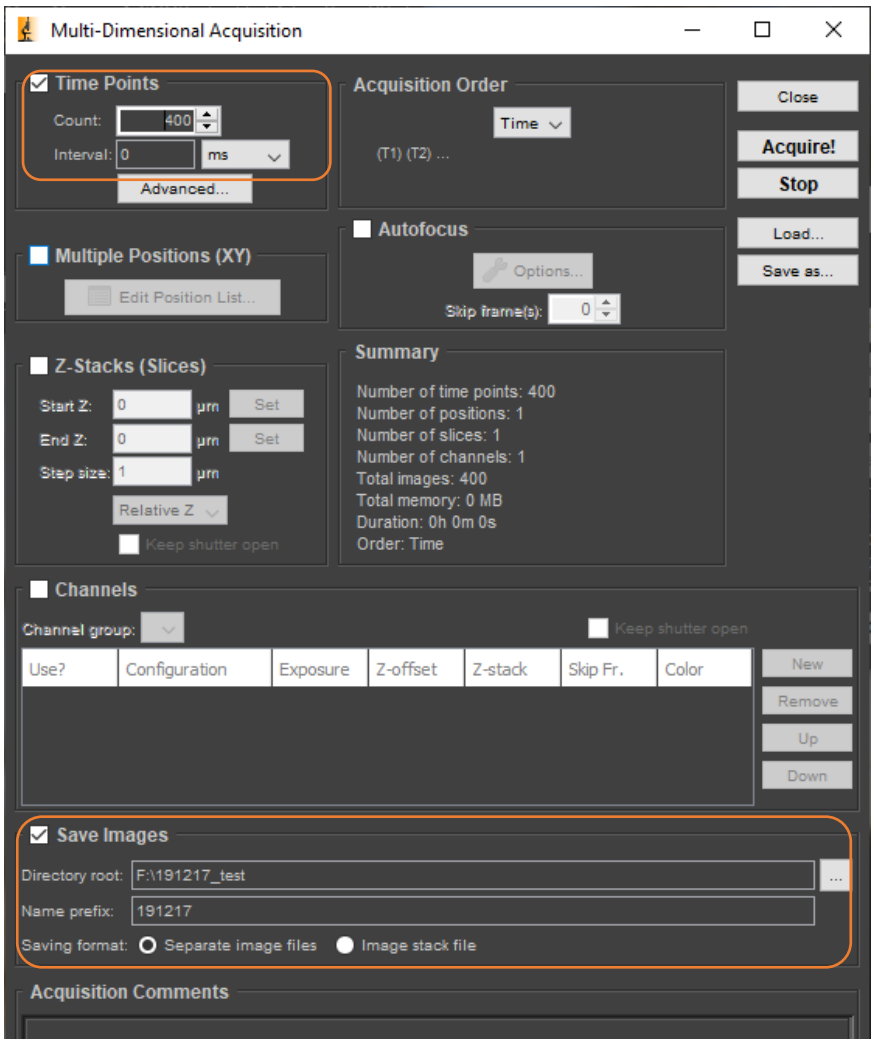

Figure A.1 Micro-Manager setup for synchronized two-channel calcium imaging. (a) To introduce Arduino as an external trigger for the two cameras, load or switch Hardware Configuration 'MMConfig_2Flash4-TwinCam_serial_TG-19-01-25'. In 'Configuration Setting', change 'Camera-Trigger' to 'External' and 'Trigger Mode' to 'start'. (b) On 'Multi-Dimensional Acquisition' window, change 'Count' to the number of frames to acquire in each imaging channel, leave 'Interval' as 0 ms. Change the 'Directory root' and 'Name prefix' if necessary. Check 'Save Images' and 'Separate image files'. All the important operations are highlighted in orange boxes.

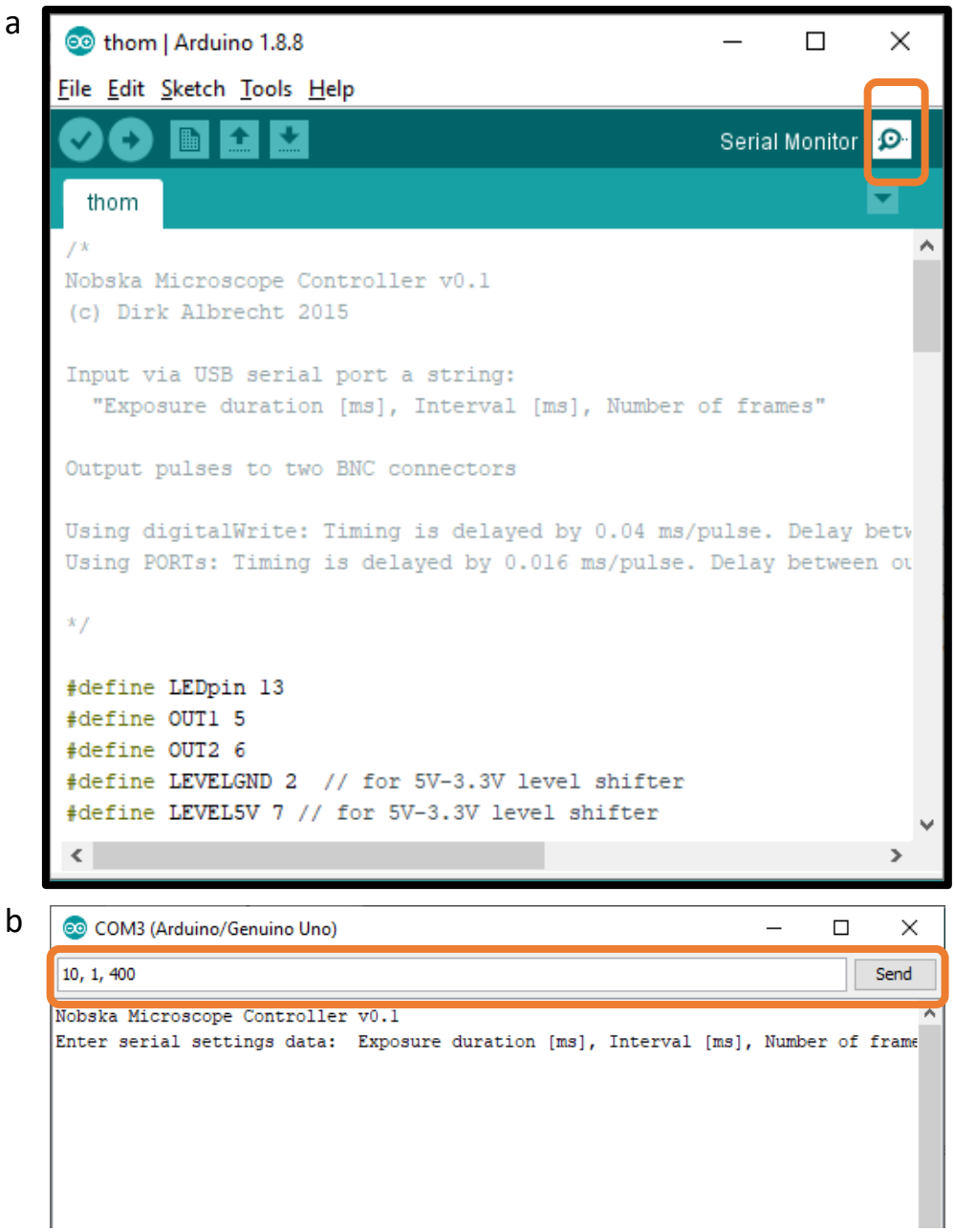

Figure A.2 Arduino setup for synchronized two-channel calcium imaging. (a) Open 'thom.ino'. On the right top corner, click 'Serial Monitor' icon to open 'COM3 (Arduino/Genuino Uno)' window. (b) Input serial settings: exposure duration [ms], interval [ms], number of frames. For example, '10, 1, 400' indicates 10 ms as exposure time, 1 ms between each exposure, and 400 frames in each channel. The combination of 10 ms as exposure time and 1 ms as interval is the highest acquisition frequency in this setup. Once one acquisition is finished, close 'COM3 (Arduino/Genuino Uno)' window and start over from Arduino main window. All the important operations are highlighted in orange boxes.

B. Animal Preparation and Image Acquisition.

1. Place the microfluidic device on a microscopic slide, channels facing up. Add drops of methyl cellulose on the channels of the microfluidic device. Transfer young adult animals inside the drops.

2. Place a 25 mm round micro cover glass between the quick-release non-magnetic imaging chambers to anchor (Figure A.3b). Flip the microfluidic device and press it gently on the cover glass.

3. Place the microfluidic device on the stage of a microscope. Find the animal to image under 40x/0.95 UPlanSApo objective.

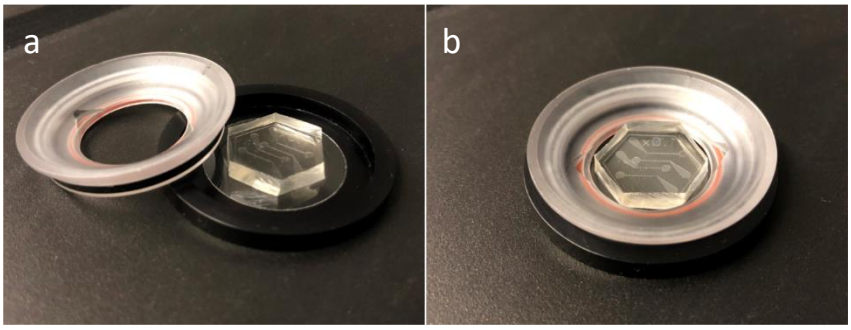

Figure A.3 Assembly of microfluidic device, 25 mm cover glass and quick release imaging chambers for calcium imaging. (a) The imaging chambers comprise of two ring chambers: the black chamber at the bottom and the white one on the top. (b) A round 25 mm cover glass is placed between these two chambers, then the microfluidic device is pressed on the cover glass.

4. Cover the microfluidic device to block the light from the environment. Turn on 100% white excitation light (filter 4) and keep the shutter fully open.

5. Click ‘Acquire!’ on ‘Multi-Dimensional Acquisition’ on Micro-Manager, move the microscope stage to place the animal to image in the view. Then click ‘send’ on ‘COM3 (Arduino/Genuino Uno)’ window. There is a time limit between the clicking operation on ‘Acquire!’ and the clicking operation on ‘send’, so do it quickly.

6. When image acquisition is done, double-check the real-time interval between frames. The real-time interval is the time difference of the last frame and the first frame divided by the total frame number. This information can be found at the bottom of the image window (Figure A.4).

7. To perform another acquisition, close ‘COM3 (Arduino/Genuino Uno)’ window, start a new one by clicking ‘Serial Monitor’ on the main Arduino window, then input serial settings: Exposure duration [ms], Interval [ms], Number of frames. Repeat steps 5-6.

C. Microfluidic cleaning and storing. After the experiment, rinse the device using running tap water, clean the channel using Ultrasonic LC60 for one minute, air dry the device using air outlet. Use Scotch magic tape to cover the waveform channels and paste the device on a microscopic slide.

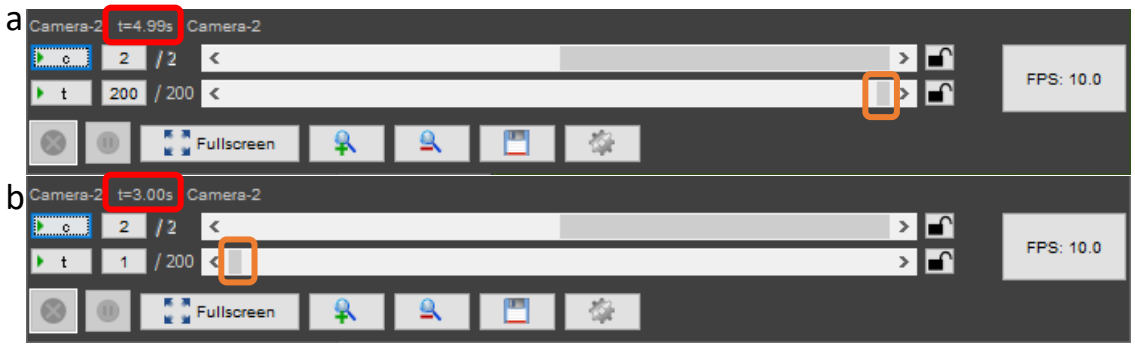

Figure A.4 Calculation of acquisition frame rate and frame interval after image acquisition. The real frame rate may not the same as the setting in Arduino, so it is better to double check the real acquisition frame rate and the interval time between frames after each video acquisition. (a) When image acquisition is done, scroll the time bar to the right (orange box) and get the time of the last frame (red box). (b) Scroll the time bar to the left (orange box) and get the time of the first frame (red box). The interval time between frames is the difference between the last and the first frames divided by the frame number. For example, the time interval in the image acquisition in this figure is (4.99-3.00)/200 = 9.95 ms. The real frame rate is 1000/9.95 = 100.5 fps.

A.1.3 Two-channel calcium imaging analysis

After image acquisition, there are three steps for two-channel calcium imaging analysis. The first step is to change image names to 'GreenImg' and 'RedImg'. The second step is to get the signal from the cell of interest. The third step is to plot traces of calcium signal results.

Step 1. Change the image names.

Usually, we save multiple tiff files under a single folder for each trial. We wrote a Matlab code to change the image name from 'position000' to 'GreenImg' and from 'position001' to 'RedImg' of all the files in each folder. After starting the code, the user needs to select

the folder manually, then name changing procedure will start. The name changing codes are listed below:

```
Folder=uigetdir('Select a folder', 'C:\Users\Lan\Desktop\');
cd(Folder);
% The directory of 'Folder' is where folders of images stored
VideoList = ls(Folder);
[m,n] = size(VideoList);

for i = 3:m
   VideoName = VideoList(i,:);
   filepath = strcat(Folder, '\', VideoName);
   cd(filepath);
   inx = 0;
fnameG = ['img_channel000_position000_time' num2str(inx, '%09d') '_z000.tif'];
while exist(fnameG, 'file')

   newnameG =  ['img_' num2str(inx, '%09d') '_GreenImg.tif'];
   fnameR = ['img_channel001_position000_time' num2str(inx, '%09d') '_z000.tif'];
   newnameR =  ['img_' num2str(inx, '%09d') '_RedImg.tif'];
   movefile(fnameG, newnameG);
   movefile(fnameR, newnameR);
   inx=inx+1;
   fnameG = ['img_channel000_position000_time' num2str(inx, '%09d') '_z000.tif'];
end
end
```

Step 2. Track and measure fluorescence signal from calcium sensor and reference protein, calculate ratio and phase (Figure A.5).

1. Open Matlab. Go to the folder '20190405_Tiff Analyzer for CalImg_SynchronizedTwoChannels', run 'ImagingAnalyzer02_1_intensity'.

2. On 'ImagingAnalyzer02intensity' window, change 'fps' (frames per second) if necessary. Select 'ratio: GCaMP/Red' if the calcium sensor is green; select 'ratio: RCaMP/Green' if the calcium sensor is red; select 'dFF: demean' if there is only one channel.

3. Click the 'Load folder of TIFs'. In the open dialog, select the first calcium sensor image of a series of tiffs to be analyzed.

4. Wait for the blue and yellow figure opened on the 'ImagingAnalyer02intensity' window.

5. Change the numbers in 'First frame' and 'Last frame' if necessary.

6. Click the ‘Track and plot’ button, then a new window with the blue and yellow figure opens.

7. On this new window, use the black crossing cursor to draw a rectangle to circle the cell of interest. If the cell is close to the edge, an error may occur. If so, repeat steps 6 and 7.

8. After drawing a rectangle, a new window appears. On the left bottom of the new window, a magnified view in the selected rectangle appears. In the magnified view at the left bottom, use the black crossing cursor to draw a polygon to circle the cell of interest. Double click to end the polygon drawing.

9. A new magnified view appears with the cell of interest in the next frame. Move the mouse to place the long black crossing cursor at the center of the cell, then click.

10. Then this window renews, and the right bottom magnified view shows the cell of interest in the next magnified frame.

11. Repeat step 9 until the cell of interest goes out of the original view, or click ‘q’ on the keyboard to stop acquiring fluorescence signal.

12. Go back to ‘ImagingAnalyzer02intensity’ window, input the name of the cell, click ‘Name neuron’, choose the head position (‘Head left’ or ‘Head right’). Choose a phase degree (‘0 deg’, ’90 deg’, ‘180 deg’, or ‘270 deg’), then move the long black crossing cursor to the chosen phase degree in the blue and yellow image and click to mark the chosen degree on the image. The name you enter will be used to calculate the location of the neuromuscular junction with respect to the cell body that you tracked, and the location of a known phase will be used to calculate its phase along the locomotor cycle in every frame.

13. Click ‘Reset image’ to clean the neuron name or chosen degree in the blue and yellow image if needed.

14. Click ‘Press for Phase’ to change the x-axis of the plot on the left bottom, and to create calcium signal plots and reference protein signal plots over time and undulatory phases.

15. Click ‘Save fig and traces’ to save plots, screenshot, and data into a mat file.

16. In the mat file, ‘NeurName’ is the neuron’s name. ‘UndFreq’ is the undulation frequency the cell traveled inside the waveform channel in the microfluidic device. ‘Ytrace’ is a serial of calcium signal from all the frames analyzed; the value in each frame is the average of the pixels with top 50% intensity in the polygon in step 8 subtracted by the medium intensity of this frame (considered as background signal). ‘rYtrace’ is a serial of signal from the reference protein channel. ‘dFF’ is the ratio of calcium signal to reference

protein signal. ‘PhaseSpace’ and ‘Time’ are the corresponding undulation phases and time of these analyzed frames, respectively.

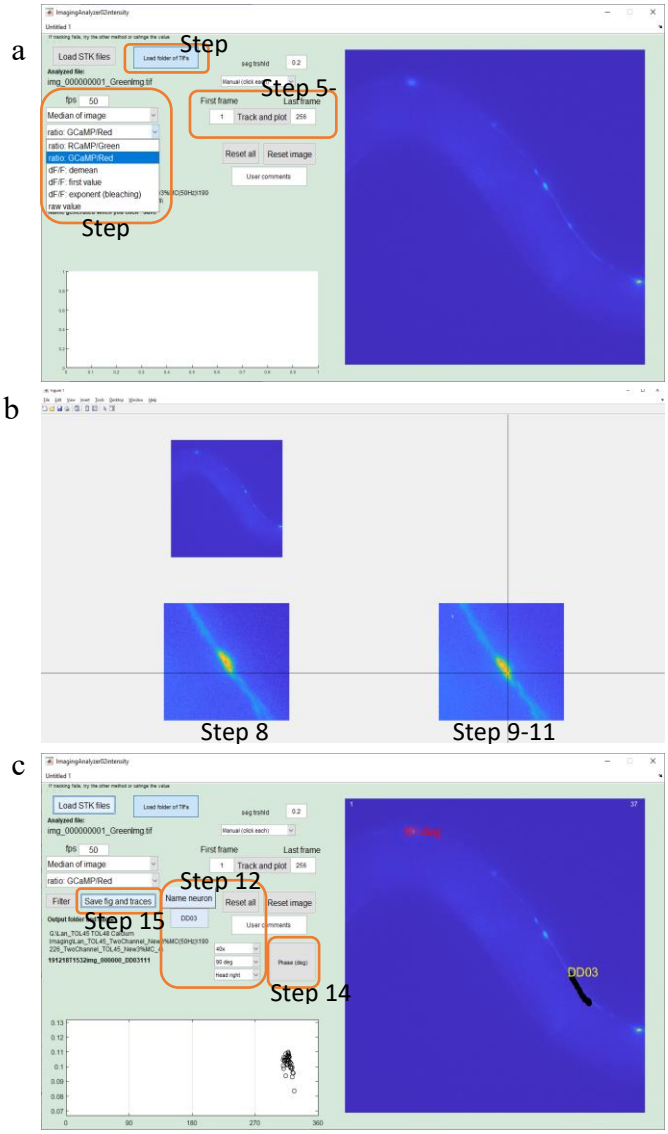

Figure A.5 Graphic user interface (GUI) of ‘Tiff Analyzer for CalImg’, Matlab codes for synchronized two-channel calcium imaging method. (a) On ‘ImagingAnalyzer02intensity’ window, change frame per second (fps); select signal output, ‘ratio:GCaMP/Red’ or ‘ratio:RCaMP/Green’ for two-channel method, or select ‘dF/F:demean’ for single-channel method (Step 2). Click ‘Load folder of TIFs’ to load tiff files (Step 3). Click ‘Track and plot’ to select the cell of interest (Step 5-6). (b) After drawing a rectangle box to circle a region to magnify, draw a polygon to select the cell of interest in the magnified rectangle box at the left bottom (Step 8), then move the long black crossing cursor to the center of the cell in the right bottom box and click (Step 9-11). (c) Input the cell name and click ‘Name neuron’; select a phase and head direction (Step 12). Click ‘Press for Phase’ to create new plots (Step 14). Click ‘Save fig and traces’ to save plots, a screenshot and a mat file (Step 15).

Step 3. Plot calcium imaging in phase space (Figure A.6).

1. Save all the mat files of one type of cell into one folder.

2. Run the Matlab code 'SignalToPhasePlots_Collator' in the folder '20160818_CalImg Analysis'. A window of 'SignalToPhasePlots_Collator' opens.

3. Check 'load folder' and 'Delete the First Frame'. Click 'Load mat files' and select the folder saved with mat files.

4. Edit 'Neur class', 'Direction(F/B)' and 'Genotype'. Change 'Bin size (deg.)' to change the plot binning number, and change 'Error shading' to select the data type for the shaded area.

5. Click 'Plot'. Change the plot type if necessary: 'Scatter', 'Line' or 'Both'.

6. Click 'Save fig and values' to save the screenshot and a mat file.

7. To load another folder of mat files, re-run the Matlab code 'SignalToPhasePlots_Collator' and repeat steps 3-6.

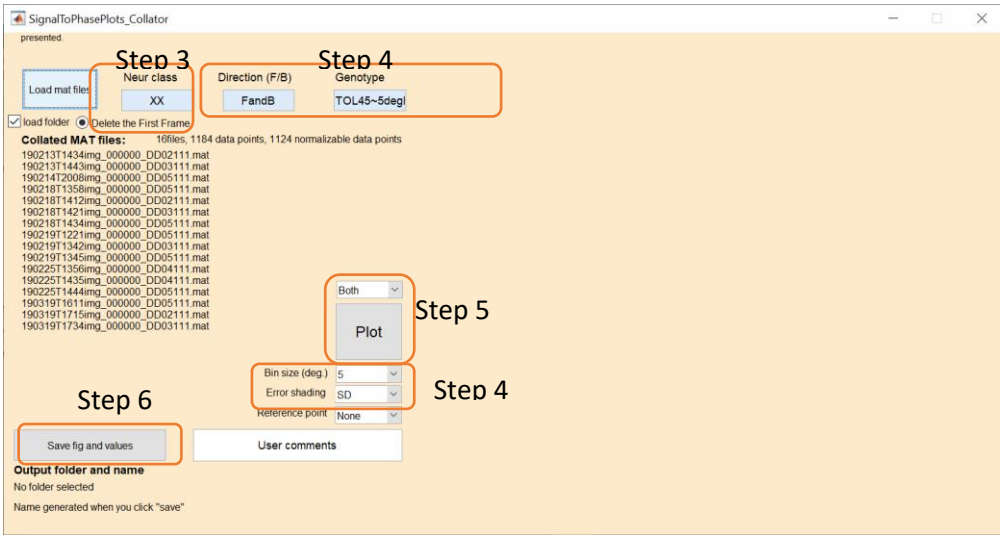

Figure A.6 Operations of Calcium imaging analysis using Matlab code 'SignalToPhasePlots_Collator'. Check 'load folder' and 'Delete the First Frame', and load mat file by clicking 'Load mat files' (Step 3). Edit 'Neur class', 'Direction (F/B)' and 'Genotype'; change 'Bin size (deg.)' and 'Error shading' (Step 4). Click 'Plot' and change plot type (Step 5). Click 'Save fig and values' to save the screenshot and a mat file.

A.2 Large Plasmid Construction Using Gibson Assembly

In Chapter 3, to identify *unc-49* gene expression pattern, we made large (15-20kb) plasmids comprising the 4 kb of *unc-49* promoter, 6.8 to 11.6 kb *unc-49* transgene, 1.8 kb of *sl2::egfp::unc-54 3'UTR* (un-translational region) and 2.6 kb of plasmid-backbone components like ampicillin resistance and Cole1 origin (ColE1) sequence. The total size of these plasmids ranges from 15 kb to 20 kb (Figure A.7).

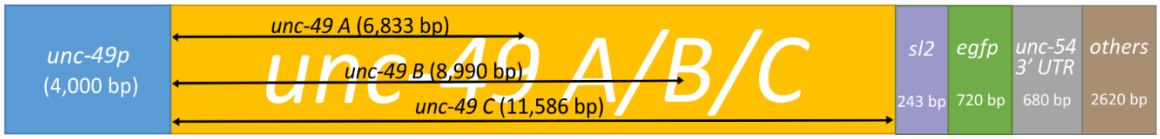

Figure A.7 The constructions of large plasmids for UNC-49 subunit identification. These plasmids compose of 4kb promoter unc-49, different UNC-49 subunits and other components. The size of these plasmids ranges from 15 to 20 kb.

We use the NEB Gibson Assembly® Cloning Kit for plasmid construction. This molecular cloning method developed by Gibson *et al.* can assemble 2-6 linear DNA fragments into a circular plasmid (Gibson et al., 2009; Gibson et al., 2010). The operations of this assembly kit are very handy. First, design primers for PCR amplification of the DNA fragment using the NEBuilder online tool (http://nebuilder.neb.com/#!/). Second, PCR amplifies the fragments using a high-fidelity PCR reagent. The amplified fragments are designed to have overlapping ends, which are short sequences identical to the end of another DNA fragments. Third, mix DNA fragments and Gibson Assembly Master Mix (exonuclease, DNA polymerase, DNA ligase, and nucleotides) and incubate for assembly reaction. Fourth, transform the assembled plasmid into competent *E.coli* cells and select for antibiotic-resistant colonies to amplify and verify by sequencing.

In the third step, the exonuclease, DNA polymerase, and DNA ligase in the Gibson Assembly Master mix contribute to plasmid assembly. The exonuclease chews the 5' ends

of the double-strand DNA fragments to allow the single-strand 3' ends to anneal, then the DNA polymerase extends the 3' end. In the end, DNA ligase takes part to ligate the chewed 5' end and the extended 3' end to finish plasmid assembly (Figure A.8). However, the difficulty of plasmid assembly increases as the size of the complete plasmid and the number of DNA fragments increase. Therefore, in this section, we explain how we generated large plasmids using pLD19 (*unc-49p::unc-49C::sl2::egfp::unc-54 3'UTR*) as an example. Moreover, we note how we modified the Gibson Assembly protocol to accommodate large plasmid construction.

A.2.1 Plasmid pLD19 (*unc-49p::unc-49C::sl2::egfp::unc-54 3'UTR*) assembly

When we first tried to assemble 5 DNA fragments into a circular plasmid, we failed by using the default NEB Gibson Assembly protocol (https://www.neb.com/protocols/2012/12/11/gibson-assembly-protocol-e5510). Therefore, we performed multistage assemblies starting from assembling pLD8 (*unc-49p::egfp::unc-54 3'UTR*), pLD13 (*unc-49p::egfp::unc-54 3'UTR*) and pLD9 (*unc-49p::unc-49::unc-54 3'UTR*) (Figure C.9a) first, then we amplified DNA fragments from pLD13 and pLD9 for the large plasmid assembly (Figure A.9 b - d). In this section, we used the assembly of pLD19 (*unc-49p::unc-49C::sl2::egfp::unc-54 3'UTR*) as an example of plasmid construction.

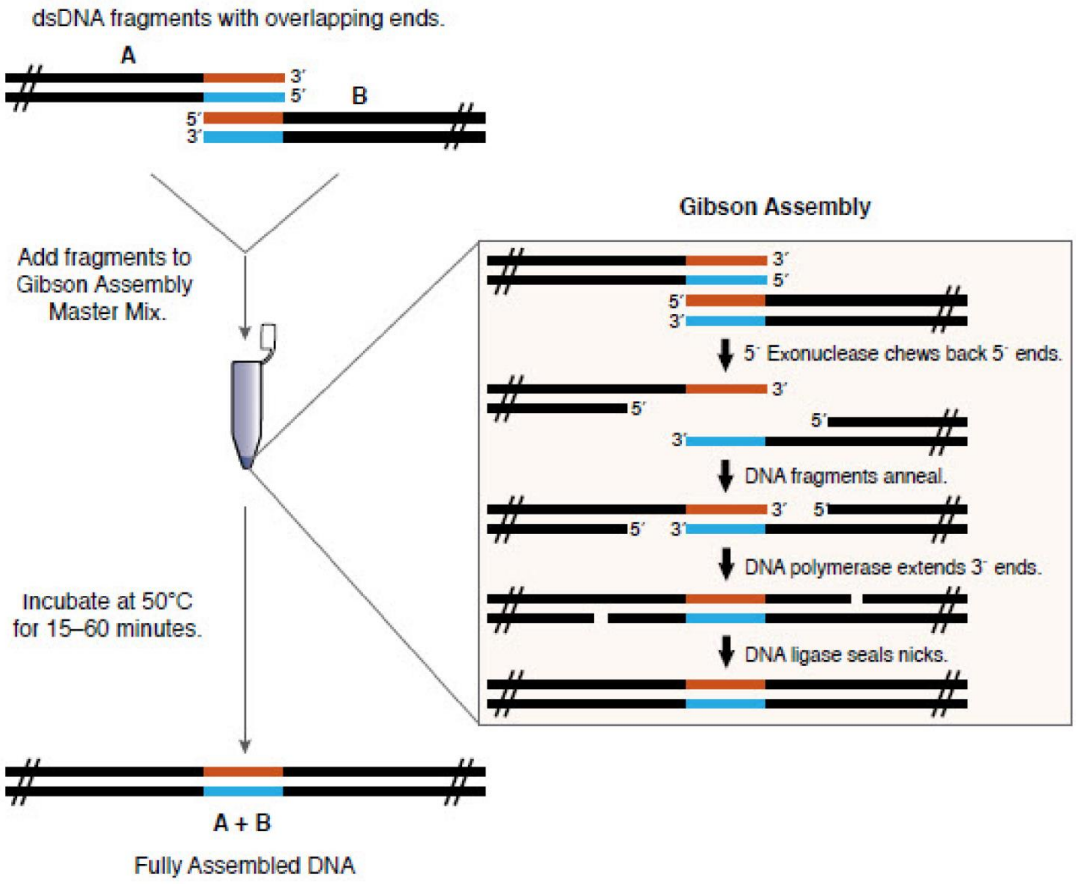

Figure A.8 The Gibson assembly reaction in the step of incubating DNA fragments and Gibson Assembly Master mix. When DNA fragments and Gibson Master mix are incubating at 50°C, the exonuclease chews the 5' ends of the double strand DNA fragments to allow the single strand 3' ends to anneal, then the DNA polymerase extends the 3' end. DNA ligase takes part to ligate the chewed 5' end and the extended 3' end to finish plasmid assembly. Obtained from 'Gibson Assembly Master Mix Instruction Manual' from NEB website (https://www.neb.com/); accessed on Feb 20th 2020.

Primer design. For pLD19, we designed an assembly of three DNA fragments. The first fragment was a 2750 bp DNA sequence containing *sl2*, *egfp*, and the first half of the ampicillin-resistant gene (*AmpR*). The second fragment was a 7435 bp DNA sequence containing the second half of *AmpR*, *unc-49p*, and the *unc-49* gene sequence from the beginning to the third exon. The third fragment was a 9779 bp sequence containing the *unc-49* gene sequence from the third exon to the end of the gene. The first fragment

sl2::egfp::AmpR was amplified from pLD13, the remaining fragments *unc-49p::unc-49 (3rd exon)* and *unc-49 (3rd exon to end)* from pLD9. After getting the fragment sequences from pLD9 and pLD13, we used the NEB online tool NEBuilder (http://nebuilder.neb.com/) to design the primers for Gibson Assembly. In NEBuilder, we set the longest fragment *unc-49(3rd exon to end)* as the backbone. Then NEBuilder designed the primers required for plasmid assembly according to the DNA fragments and the settings; moreover, according to the PCR polymerase, NEBuilder offered the accordant annealing temperatures of primers.

Table A.1 Primers for pLD19 Assembly

		Primers Designed by NEBuilder*		Modified Primers		
DNA Fragments	Size (bp)	Forward Primer	Reverse Primer	Forward Primer	Reverse Primer	Ta**
sl2::egfp:: AmpR	2750	atgctccagaccttc attaaGCTGTC TCATCCTAC TTTCACC	gtgtcacgctCGT CGTTTGGTA TGGCTTC	same as NEBuilder	gtgtcacgctcgt cgttt	64°C
unc-49p::unc-49(3exon)	7435	ccaaacgacgAG CGTGACACC ACGATGC	atcaacttctgaaact gcagAGATTG AAGAAACGT GTATCGTAA TTC	ccaaacgacg agcgtgac	catatcaacttctg aaactgcag	63°C
unc-49(3exon to end)	9779	CTGCAGTTT CAGAAGTTG ATATG	TTAATGAAG GTCTGGAGC	same as NEBuilder	same as NEBuilder	63°C

*In the column of Primers Designed by NEBuilder, the uppercase letters indicate the part of the primer that anneals to the template, and the lowercase letters are hangovers.

NEBuilder assumes that all these DNA fragments come from different plasmids without any overlapping. However, this did not apply to the assembly of pLD19. Templates pLD9 and pLD13 have thousands of the same sequence, such as *unc-49p, sl2, egfp, unc-54 3'UTR*, and *AmpR*; and the annealing temperatures provided by NEBuilder are calculated by the part of the primer that anneals to the template. Therefore, we modified primers. If the overlapping part of a primer can also anneal to the template, we usually only keep the overlapping part of the primer and trim it to a ~20 bp sequence (Table A.1). For two reasons, first, long primers are expensive; second, the annealing temperature of them is high, sometimes higher than the maximum annealing temperature of the PCR kit. To

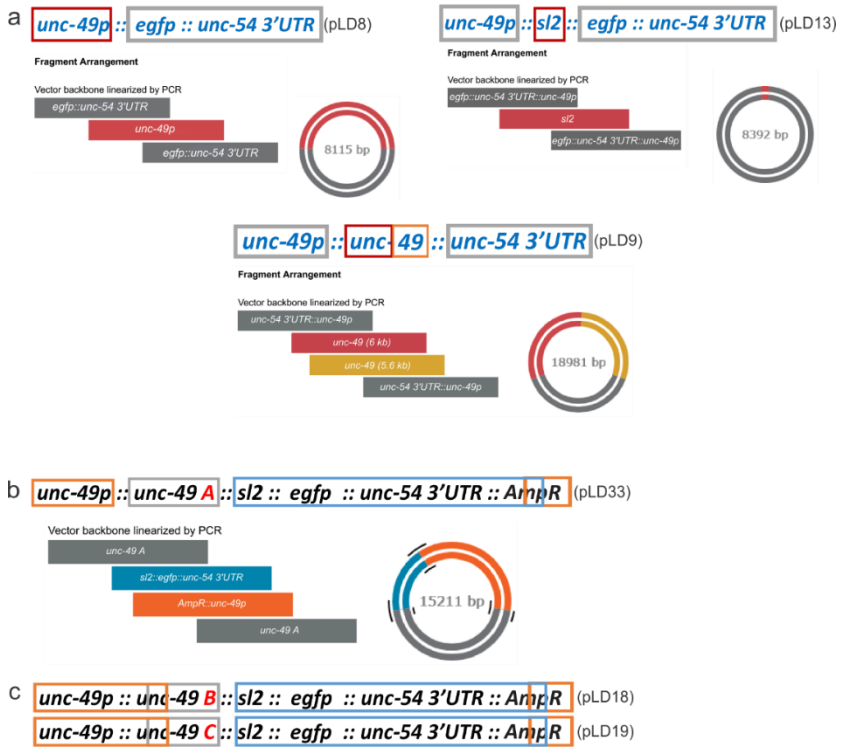

Figure A.9 Assembly steps for large plasmids pLD33, pLD18 and pLD19. To make large plasmids, we carried out multistage assembly. pLD8, pLD13 and pLD9 in (a) were made first, then these plasmids served as templates for DNA fragments for large plasmids assembly in b and d. To increase assembly successful rate, the overlapping between two DNA fragments can be longer than 100 bp. In pLD33 (b), pLD18 and pLD19 (c), the long overlapping is the intersects of blue and orange boxes

increase the DNA fragment assembly probability, we usually increase the overlapping region of two DNA fragments to over 100 bp.

DNA fragment preparation for Gibson Assembly. To increase the assembly successful rate, we prepared high concentrations of DNA fragments for the step of fragment assembly. To get more amount of DNA fragments, we amplified the DNA fragments with a high volume of PCR reaction mixture. To avoid unwanted DNA fragments, we did not use the PCR product for assembly directly as documented in NEB Gibson Assembly protocol; instead, we ran the PCR product into DNA agarose gel and extracted the desired DNA bands. This step not only excludes the unwanted band but also concentrates the DNA fragment, as well as increases the accuracy in the calculation of fragment amount in the assembly step.

For pLD19 plasmid assembly, first, we prepared 75 µL PCR reaction mixture for fragment *sl2::egfp::AmpR*, 200 µL PCR reaction mixture for fragment *unc-49p::unc-49(3exon)* and 200 µL PCR reaction mixture for fragment *unc-49 (3exon to end),* and PCR amplified these fragments. Second, we ran the PCR product in agarose gel and extracted the unwanted DNA bands. After the gel extraction experiment, the concentrations of these three DNA fragments were 190.3 ng/ µL, 180.3 ng/ µL, and 202.5 ng/ µL, respectively. Third, we prepared the mixture for Gibson assembly according to Table A.2 and incubated the mixture in a thermocycler at 50°C for one hour for plasmid assembly. Fourth, we transformed 4 µL of the mixture to Beta 10 competent cells. Fifth, we seeded 4 ampicillin selection LB plates with 200 µL of transformed cells and incubated these plates overnight at 37°C. On the following day, we got 20 single bacterial colonies in total. We picked 14 colonies to do colony PCR to check the junction of two DNA fragments and got 8 strong

positive results. To further confirm my plasmid, we sent two plasmids to sequence all the junction parts of DNA fragments, and all the sequence results indicated the successful and correct plasmid assembly.

Table A.2 Gibson Assembly Mixture for pLD19 Assembly

	sl2::egfp::AmpR	*unc-49p::unc-49(3exon)*	*unc-49(3exon to end)*
Size (bp)	2750	9779	7434
Concentration (ng/μL)	169.3	202.5	180.3
Mass (ng)	0.4	0.2	0.2
Volume (μL) = Mass/Concentration	0.4*2750*650/1000 = 715.0	0.2*9779*650/1000 = 1271.27	0.2*74340*650/1000 = 966.4

*The volume of 2X Gibson assembly master mix is the sum of all DNA fragments, which is 5.36+6.27+4.22 = 15.85 μL

A.2.2 Protocol of large plasmid assembly using NEB Gibson assembly

In this section, we combined the procedures from primer design to competent cell transformation and modified them for large plasmid assembly.

A. Primer Design using NEBuilder.

1. Go to NEBuilder (http://nebuilder.neb.com/)

2. Paste or load the sequences to be assembled, select 'PCR' as a method for production of a linearized fragment, and leave the remaining by default.

3. Modify 'Product/Kit', 'Minimum Overlap (nt)', and 'PCR Polymerase/Kit' in 'Building Settings' if necessary, then click 'Done'.

4. Check whether the assembled sequence is the same as the designed plasmid.

5. Go to the 'Summary' tab, export summary report by clicking the 'Export summary (PDF)', and save primer sequences by clicking 'Export oligos'.

6. If the plasmids or genomes where DNA fragments will be amplified from do not have overlapping, double-check the annealing temperature of the annealing part of the designed primer (capitalized) with NEB Tm calculator and modify the primer sequence by increasing or reducing base pairs if necessary.

If the plasmids or genomes where DNA fragments will be amplified from do have overlapping, for example, one DNA fragment ends in the middle of ampicillin-resistant gene and another one starts at that the same position as pLD33, redesign this pair of primers manually. First, reduce the length of the primers to ~20 bp. Second, move the ~20 bp primers further away from the junction so that the overlapping of these two DNA fragments can be longer, which increases the assembly rate.

B. DNA fragment preparation using Phusion High-Fidelity DNA Polymerase Kit and QIAEX II Gel Extraction Kit.

1. PCR amplify each DNA fragment using 25 µL of Phusion High- Fidelity DNA Polymerase Kit according to the primer design and run the PCR product in an agarose gel to check if the bands are correct or not.

2. Decide the total volume of PCR reaction for each DNA fragment according to Table A.3.

Table A.3 Volumes of PCR Reaction and QIAEX II for Different DNA Fragment Size

DNA fragment size	PCR reaction volume	QIAEX II volume
< 2 kb	50 µL	10 µL
2 - 5 kb	100 µL	15 µL
5 - 7 kb	150 µL	20 µL
> 7 kb	200 µL	30 µL

3. PCR amplify the DNA fragments using the Phusion High-Fidelity DNA Polymerase Kit.

4. Run all the PCR products into trick 0.8% agarose gel.

5. Excise the DNA band from the agarose gel with a clean and sharp razor.

6. Use a 15 mL centrifuge tube to hold the gel slices, and measure the weight of the gel, which is the weight difference between the empty tube and the tube with gel slices. Each centrifuge tube should only use for one DNA fragment.

7. Convert the weight of gel to its volume using the following formulation: 1 g ≈ 1 mL. Add Buffer QX1 according to DNA fragment size: 6 volumes for < 100 bp; 3 volumes for 100 bp - 4 kb; 3 volumes with 2 volumes of nuclease-free-water for > 4 kb. Add 6 volumes of Buffer QX1 when using > 2% or Metaphor agarose gels.

8. Resuspend QIAEX II by vortexing for 30s. Add QIAEX II to the centrifuge tubes and vortex to mix. Use 10 µL QIAEX II for < 2kb DNA fragment; 15 µL QIAEX II for 2 - 5 kb DNA fragment; 20 µL QIAEX II for 5 - 7kb DNA fragment; 30 µL QIAEX II for > 7kb DNA fragment (Table A.3).

9. Incubate the centrifuge tubes at 50°C for 20-30 minutes to solubilize the agarose and allow QIAEX II to bind DNA. Mix by vortexing every 2 min to keep QIAEX II suspended.

10. Transfer 1.5 mL sample to a 1.8 mL Eppendorf tube, centrifuge the sample for 30 s, then pour out the supernatant. Repeat this step till all the samples centrifuged.

11. Wash the pellet with 500 µL Buffer QX1. Resuspend the pellet by vortexing. For Fragments larger than 8 kb, resuspend the pellet by inverting and flicking the tube. Centrifuge the sample for 30 s, pour the supernatant and discard the remaining trace of supernatant using a pipet.

12. Wash the pellet *TWICE* with 500 µL Buffer PE. Resuspend the pellet by vortexing. Fragments larger than 8 kb, resuspend the pellet by inverting and flicking the tube. Centrifuge the sample for 30 s and carefully remove all traces of supernatant with a pipet.

13. Air-dry the pellet for 15 to 30 minutes till the pellet becomes white. Do not over-dry the pellet.

14. To elute DNA, add 20 µL of nuclease-free-water and resuspend the pellet by vortexing. Fragments larger than 8 kb, resuspend the pellet by inverting and flicking the tube. Incubate the Eppendorf tube at 50°C for 10 minutes, or at room temperature overnight.

15. Centrifuge for 1 minute, and carefully pipet the supernatant into a clean tube. The supernatant now contains the purified DNA.

16. Optional: repeat steps 14 and 15 and combine the eluates. A second elution step will increase the yield by approximately 10 - 15%.

C. Plasmid Assembly using NEB Gibson Assembly Kit.

1. Measure the DNA concentration (ng/µL) using the Thermo Scientific NanoDrop Lite spectrophotometer.

2. Calculate the amount of DNA fragments according to Table A.4 and prepare the assembly mixture accordingly.

3. Incubate the mixture in a thermocycler at 50°C for 1 hour, then store it at 4°C or -20°C for subsequent transformation. After this incubation, there should be some assembled plasmid in the mixture.

Table A.4 Amount of Fragments for Gibson Assembly

	2-4 Fragment Assembly
Total Amount of Fragments	0.02–1 pmols*
	X µl
Gibson Assembly Master Mix (2X)	half of the total volume
Nuclease-free-water	half of the total volume - X µl
Total Volume	20-30 µl

* pmols = (weight in ng) x 1,000 / (base pairs x 650 daltons)
Optimized cloning efficiency is 50-100 ng of vector with a 2-fold molar excess of each insert. Use 5 times more of inserts if size is less than 200 bps.

D. Transform assembled plasmid to NEB® 10-beta competent E. coli cells.

1. Thaw a tube of NEB 10-beta Competent *E. coli* cells on ice for 5 minutes, or till the frozen cells are completely thawed.

2. Add 2-10 µl of assembled plasmid mixture to the cell mixture, and carefully flick the tube 4-5 time to mix the cell and the assembled plasmid. Do not vortex.

3. Place the tube on ice for 30 minutes. Do not mix.

4. Microwave ~300 mL water for 1 minute and adjust the temperature to EXACTLY 42°C. Heat shock the tube in 42°C water bath for EXACTLY 30 seconds. Do not mix.

5. Place the tube on ice for 5 minutes. Do not mix.

6. Pipette 950 µl of room temperature NEB 10-beta/Stable Outgrowth Medium into the mixture.

7. Place the tube to a 37°C shaker and sake the tube vigorously (250 rpm) for 1 hour. Meanwhile, warm 4 selection plates to room temperature.

8. Mix the tube by inverting 5 times, and seed 50-200 µL cell mixture to each selection plate, then incubate these plates at 37°C overnight. Alternatively, incubate at 30°C for 24-36 hours or 25°C for 48 hours.

E. Confirm positive colony and store.

1. Pick multiple colonies for colony PCR using OneTaq Quick-Load 2X Master Mix to check a junction of assembled fragments.

2. Run the colony PCR product in agarose gel to check the DNA bands.

3. Select 2 colonies with positive colony PCR results for 10 mL culture in LB medium.

4. Extract plasmids kit from these 2 colonies using MiniPrep extraction and send these two plasmids for sequencing all the junctions of all the DNA fragments.

5. If the sequence results are correct, culture the colony in 25-50 mL LB medium and extract the plasmid using the MidiPrep extraction kit.

6. Inventory the plasmid and update its sequence information to Quartzy.

A.2.3 Five rules of thumb for large plasmid construction

First, use the High-Fidelity PCR Kit to prepare DNA fragments to reduce possible mutations in DNA fragment amplification. Second, the longer overlap between DNA fragments the better. The longest overlap we successfully tried was around 120 bp. Third, 3 to 4 DNA fragments for assembly are ideal. Fourth, start with making small plasmids, then use them as fragments for large plasmid assembly. Fifth, the higher the concentration of DNA fragment for assembly the better.

A.3 Motoneuron Identification in NeuroPAL

In Chapter 2, to identify gene expression patterns, we used an identification strain NeuroPAL, which had been developed by Eviatar Yemini from the Hobert Laboratory at Columbia University. In NeuroPAL, different classes of neurons express unclearly localized fluorescent proteins of different color and color combinations, except for green, yellow, and cerulean. It is then possible to unambiguously identify any motoneuron that transgenically expresses fluorescent reporters GFP, YFP or CFP by the different fluorescence patterns of NeuroPAL and its neuronal position along the ventral nerve cord. In this section, we detail how we incorporated the gene to be identified into NeuroPAL strain, how we imaged eGFP as a fluorescent reporter, and the different fluorescent proteins in NeuroPAL, and how we performed motoneuron identification.

A.3.1 NeuroPAL strains

The Hobert Laboratory has graciously shared NeuroPAL strains with us pre-publication. The strain we received were OH15262 (*otIs669[NeuroPAL]V*), OH15263 (*otIs670[NeuroPAL]V*), OH15495 (*otIs696[NeuroPAL]*), OH15500 (*otIs669[NeuroPAL]V, otIs672[Panneuronal GCaMP6s]*), OH15363 (*otIs669[NeuroPAL]V, him-5 (e1490) him-5*), OH15364 (*otIs670[NeuroPAL]V, him-8(e1489)IV*) and OH15528 (*otIs696[NeuroPAL]V, him-5(e1490)V*) (Table A.5).

NeuroPAL expresses four fluorescent proteins: TagRFP-T (red), mTagBFP-2 (blue), CyOFP (orange) and mNeptune2.5 (infrared). TagRFP-T expresses in all the neurons (panneurnally), while mTagBFP-2, CyOFP and mNeptune2.5 express in subsets of neurons.

A.3.2 Incorporating genes to be identified to NeuroPAL

To identify the expression pattern of *unc-4p::unc-49A/B/C::sl2::egfp*, we tried two methods in incorporating pLD17, pLD18 and pLD19 to NeuroPAL strains. The first method was microinjecting the plasmids into NeuroPAL strain OH15262. The second method was crossing the animals expressing plasmids with NeuroPAL strain OH15262. The details of these two methods were described in Chapter 2. For the first method, we made TOL62 (*aatEx62 [unc-49p::unc-49 subunit A::sl2:: egfp, otIs669 (NeuroPAL)V*]), TOL63 (*aatEx63 [unc-49p::unc-49 subunit B::sl2:: egfp, otIs669 (NeuroPAL)V*]) and TOL61 (*aatEx61 [unc-49p::unc-49 subunit C::sl2:: egfp, otIs669 (NeuroPAL)V]*). For the second method, we made TOL64 (*aatEx64 [unc-49p::egfp, otIs669 (NeuroPAL)V]*).

Table A.5 NeuroPAL Strains

Strain Name	Genotype	Backcrossing	Fluorescence brightness	Others

OH15262	*otIs669[NeuroPAL]V*	8x outcrossed	The brightest NeuroPAL so far.	
OH15263	*otIs670[NeuroPAL]V*	8x outcrossed	Medium brightness	this strain useful when imaging weak GFP/YFP/CFP reporters.
OH15495	*otIs696[NeuroPAL]*	8x outcrossed	Medium brightness	The array seems to have landed somewhere on chromosomes I-III. Useful for crossing to reporters/mutants on V
OH15500	*otIs669[NeuroPAL]V ; otIs672[Panneuronal GCaMP6s]*	23x (both integrates were outcrossed 8x prior to crossing them)		A relatively isogenic NeuroPAL; GCaMP6s strain
OH15363	*otIs669[NeuroPAL]V ; him-5 (e1490) him-5*			
OH15364	*otIs670[NeuroPAL]V ; him-8(e1489)IV*			
OH15528	*otIs696[NeuroPAL]V ;him-5(e1490)V*			

Microinjection turned out to be more feasible than crossing. Because the fluorescent protein in NeuroPAL is not typical GFP/RFP, it is very hard to see the fluorescence under our fluorescence stereomicroscope (Leica MZ16 FA). To use NeuroPAL for neuron deification, NeuroPAL must be homozygous, so we had to pick multiple animals from many plates and made them into slides and screened for the homozygous of NeuroPAL using a compound epifluorescence microscope (LEICA DM6000CS). Instead, using microinjections, we only needed to microinject plasmids to NeuroPAL strains and looked for green fluorescent animals after several days.

A.3.3 Imaging GFP and NeuroPAL

Animal Preparation The fluorescent reporter in TOL61 - TOL 64 is eGFP. One day before imaging animals, we picked green fluorescent animals in the fourth larval stage (L4) and stored them at 15°C overnight, so during imaging, these animals would be young adults or still in the fourth larval stage.

Confocal microscopy. To image GFP and NeuroPAL fluorescent proteins, we used a laser scanning confocal microscope (Leica SP8) with 40x and 1.3NA oil objective. On the confocal software (Leica LAS X), we set up two serial acquisition series with three between-line acquisition channels for each. In the first serial acquisition, we acquired brightfield transmission, GFP, and TgRFP-T. To acquire bright-field transmission, we turned the transmitted light PMT gain to ~600%; for GFP we used 488 nm excitation laser at 2% and emission wavelength between 498 and 520 nm, with HyD detector at 100% and green pseudo-color channel; for TgRFP-T we used 522 nm excitation laser at 9.2% and emission wavelength between 560 and 620 nm, with PMT detector at 800% and gray pseudo-color channel. TgRFP-T is a panneuronal marker, so by checking the co-localization with GFP we determined whether the GFP was expressed in neurons. If it did, we made sure not to move the sample or change the Z-stack setting and ran the second serial acquisition series for mTaqBFP2, CyOFP, and mNeptune2.5. In this acquisition series, for mTaqBFP2 we used 405 nm excitation laser at 5% and emission wavelength between 430 and 470 nm, with HyD detector at 385% and blue pseudo-color channel; for CyOFP, we used 488 nm excitation laser at 17% and emission wavelength between 606 and 623 nm with PMT detector at 946% and green pseudo-color channel; for mNeptune2.5 we used 638 nm excitation laser at 32% and emission wavelength between 625 and 722

nm with HyD detector at 346% and red pseudo-color channel (Table A.6). Because the neuronal position along the ventral nerve cord is an important reference for neuron identification, we used the navigator module (in Leica LAS X) to tile images of the whole animal from the head to the tail.

Table A.6 LEICA Confocal Microscope Setting for NeuroPAL and GFP

	Excitation Light		Emission Light		
	Wavelength	Intensity	Wavelength	Gain	Pseudo-color
GFP*	488	2%	498 - 520	100%	Green
TgRFP-T*	552	9.20%	560 - 620	800%	Gray
mTaqBFP2**	405	5%	430 - 470	385%	Blue
CyOFP**	488	17%	606 - 623	946.50%	Green
mNeptune2.5**	638	32%	625 - 722	346%	Red

* these two channels were set together in one serial caption between lines

** these three channels were set together in another serial caption between lines

A.3.4 Motoneurons identification

To positively identify ventral nerve cord motoneurons, we used ImageJ (imagej.nih.gov) to generate a composite of the maximal intensity projections of mTagBFP2, CyOFP, and mNeptune2.5 and compared it to an image of eGFP-expressing neurons (Figure A.10). We used the combination of fluorescent NeuroPAL colors and neuronal position along the ventral nerve cord to identify each eGFP-expressing motoneuron. These two references are indispensable because neurons may shift their relative positions during development so documented positions might be inaccurate. Taking advantage of the NeuroPAL strains, we identified the motoneuron expression in TOL61, TOL62, and TOL63.

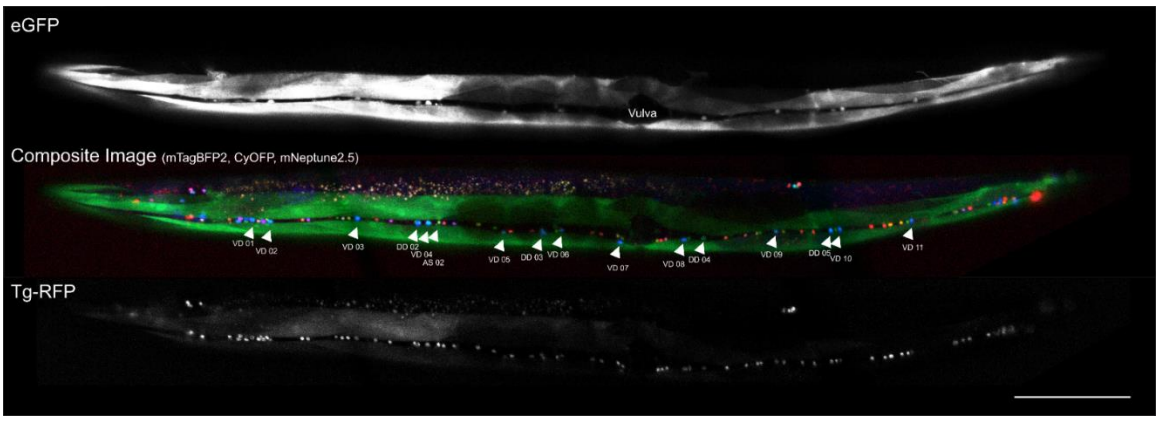

Figure A.10 All ventral cord motoneurons can be identified by NeuroPAL fluorescence and neuronal position. eGFP expression was identified mostly in DD and VD motoneurons (top); mTagBFP1, CyOFP and mNeptune2.5 are each expressed of subsets of neurons to generate class-specific color combinations (middle); TgRFP-T is expressed panneuronally (bottom). eGFP co-localized with AS02 and all DD and VD motoneurons in this young adult animal (TOL61, *aatEx61 [unc-49p::unc-49 subunit C::sl2:: egfp, otIs669 (NeuroPAL)V]*). Scale bar = 100 µm.

APPENDIX B

TRANSGENIC C. ELEGANS STRAINS

This appendix lists part of the transgenic animals we made through microinjection. We detailed the injection mixture ingredient with component concentration, strains got injected into and some comments for some injections.

Table B.1 Transgenic Strains

TOL name	aatEx Name	Genotype	Injection Mixture Ingredient	Worms Got Injected	Comment
TOL18	aatEx2	*myo-3p::nls::RCaMP2; mec-4p::ChR(H134R)::YFP; pha-1(+); pha-1(lf) e2123 III*	50 ng/uL myo-3p::nls::RCaMP2 (pLQ1); 50 ng/uL mec-4p::ChR(H134R)::YFP (pAG56); 50 ng/uL pha-1(+) (pBX)	GE24	
TOL 26	aatEx4	*unc-25p::RCaMP2; mec-4p::ChR(H134R)::YFP; myo-2p::GFP; pha-1(lf) e2123 III*	30 ng/uL unc-25p::RCaMP2 (pLD4); 50 ng/uL mec-4p::ChR(H134R)::YFP (pAG56); 30 ng/uL myo-2p::GFP (pCFJ421)	N2	
TOL 29	aatEx9	*unc-49p::EGFP; unc-25p::Cerulean; del-1p::wrmScarlet; pha-1(+)； pha-1(lf) e2123 III*	50 ng/uL unc-49p::EGFP (pLD8); 50ng/uL unc-25p::Cerulean (pLJ4); 40 ng/uL del-1p::wrmScarlet (pLJ1); 30 ng/uL pha-1(+) (pBX)	GE24	
TOL 30	aatEx10	*unc-49p::EGFP; unc-25p::Cerulean; acr-2p::wrmScarlet; pha-1(+)； pha-1(lf) e2123 III*	50 ng/uL unc-49p::EGFP (pLD8); 50 ng/uL unc-25p:Cerulean (pLJ4); 40 ng/uL acr-2p::wrmScarlet (pLD11); 30 ng/uL pha-1(+) (pBX)	GE24	
TOL 32	aatEx11	*acr-2p::RCaMP2; mec-4p::ChR(H134R)::YFP; myo-2p::GFP; pha-1(lf) e2123 III*	40 ng/uL acr-2p::RCaMP2 (pLD14); 50 ng/uL mec-4p::ChR(H134R)::YFP (pAG56); 40 ng/uL myo-2p::GFP (pCFJ421)	GE24	

Table B.1 Continued

TOL31	aatEx12	*unc-49p::unc-49 subnunitA::sl2::EGFP; unc-25p::Cerulean; del-1p::wrmScarlet; pha-1(+)； pha-1(lf) e2123 III*	50 ng/uL unc-49p::unc-49 subunitA::sl2::EGFP (pLD17); 50 ng/uL unc-25p::Cerulean (pLJ4); 50 ng/uL del-1p::wrmScarlet (pL1); 30 ng/uL pha-1(+) (pBX)	GE24	
TOL33	aatEx13	*unc-49p::unc-49 subunitA::sl2::EGFP; unc-25p::Cerulean; del-1p::wrmScarlet; myo-2p::mCherry*	35 ng/uL unc-49p::unc-49 subunitA::sl2::EGFP (pLD17); 35 ng/uL unc-25p::Cerulean (pLJ4); 35 ng/uL del-1p::wrmScarlet (pLJ1); 10 ng/uL myo-2p::mCherry (pCFJ90)	N2	del-1p::wrmScarlet (pLJ1) did not express
TOL38	aatEx14	*unc-49p::unc-49 subunitC::sl2::EGFP; unc-25p::Cerulean; del-1p::wrmScarlet; myo-2p::mCherry*	15 ng/uL unc-49p::unc-49 subunitC::sl2::EGFP (pLD19); 15 ng/uL unc-25p::Cerulean (pLJ4); 15 ng/uL del-1p::wrmScarlet (pLJ1); 10 ng/uL myo-2p::mCherry (pCFJ90)	N2	
	aatEx15				
TOL36	aatEx16	*unc-49p::unc-49 subunitB::sl2::EGFP; unc-25p::Cerulean; del-1p::wrmScarlet; myo-2p::mCherry*	23.3 ng/uL unc-49p::unc-49 subunitB::sl2::EGFP (pLD18); 23.3 ng/uL unc-25p::Cerulean (pLJ4); 23.3 ng/uL del-1p::wrmScarlet (pLJ1); 9 ng/uL myo-2p::mCherry (pCFJ90)	N2	
	aatEx17	*unc-49p::unc-49 subunitA::sl2::EGFP; unc-25p::Cerulean; del-1p::wrmScarlet; myo-2p::mCherry*	30 ng/uL unc-49p::unc-49 subunitA::sl2::EGFP (pLD17); 30 ng/uL unc-25p::Cerulean (pLJ4); 30 ng/uL del-1p::wrmScarlet (pLD22); 8 ng/uL myo-2p::mCherry (pCFJ90)	N2	
	aatEx18				
	aatEx19				
TOL37	aatEx20	*acr-2p::GCaMP6; acr-2p::wrmScarlet*	50 ng/uL acr-2p::GCaMP6 (pLD5); 50 ng/uL acr-2p::wrmScarlet (pLD11)	N2	
TOL47	aatIs7	*acr-2p::GCaMP6; acr-2p::wrmScarlet*	50 ng/uL acr-2p::GCaMP6 (pLD5); 50 ng/uL acr-2p::wrmScarlet (pLD11)	N2	

Table B.1 Continued

TOL48	*aatIs8*	*acr-2p::GCaMP6s; acr-2p::wrmScarlet*	50 ng/uL acr-2p::GCaMP6 (pLD5); 50 ng/uL acr-2p::wrmScarlet (pLD11)		
TOL40	*aatEx21*	*unc-49p::EGFP; pha-1(+); pha-1(lf) e2123 III*	50 ng/uL unc-49p::EGFP (pLD8); 50 ng/uL pha-1(+) (pBX)	GE24	
	NAN	*del-1p::Cerulean; unc-25p::wrmScarlet; pha-1(+); pha-1(lf) e2123 III*	35 ng/uL del-1p::Cerulean (pLD24); 35 ng/uL unc-25p::wrmScarlet (pLJ3); 30 ng/uL pha-1(+) (pBX)	GE24	del-1p(1.6kb)::Cerulean did not express
TOL39	*aatEx22*	*unc-49p::unc-49 subunitA::sl2::EGFP; pha-1(+); pha-1(lf) e2123 III*	35 ng/uL unc-49p::unc-49 subunitA::sl2::EGFP (pLD17); 35 ng/uL pha-1(+) (pBX)	GE24	
	NAN	*unc-49p::unc-49 subunitB::sl2::EGFP; pha-1(+); pha-1(lf) e2123 III*	25 ng/uL unc-49p::unc-49 subunitB::sl2::EGFP (pLD18); 25 ng/uL pha-1(+) (pBX)	GE24	LOST, unc-49B's concentration needs to decrease
TOL41	*aatEx23*	*unc-49p::unc-49 subunitC::sl2::EGFP; pha-1(+); pha-1(lf) e2123 III*	15 ng/uL unc-49p::unc-49 subunitC::sl2::EGFP (pLD19); 35 ng/uL pha-1(+) (pBX)	GE24	
	NAN	*del-1p::Cerulean; unc-25p::wrmScarlet; pha-1(+); pha-1(lf) e2123 III*	50 ng/uL del-1p::Cerulean (pLD24); 10 ng/uL unc-25p::wrmScarlet (pLJ3); 40 ng/uL pha-1(+) (pBX)	GE24	del-1p(1.6kb)::Cerulean did not express
TOL42	*aatEx24*	*unc-25p::GCaMP6s; unc-25p::wrmScarlet; pha-1(+); pha-1(lf) e2123 III*	50 ng/uL unc-25p::GCaMP6s (pVM1); 25 ng/uL unc-25p::wrmScarlet (pLJ3); 25 ng/uL pha-1(+) (pBX)	GE24	
TOL45	*aatIs1*	*unc-25p::GCaMP6s; unc-25p::wrmScarlet; pha-1(+); pha-1(lf) e2123 III*	50 ng/uL unc-25p::GCaMP6s (pVM1); 25 ng/uL unc-25p::wrmScarlet (pLJ3); 25 ng/uL pha-1(+) (pBX)	GE24	
TOL46	*aatIs2*	*unc-25p::GCaMP6s; unc-25p::wrmScarlet; pha-1(+); pha-1(lf) e2123 III*	50 ng/uL unc-25p::GCaMP6s (pVM1); 25 ng/uL unc-25p::wrmScarlet (pLJ3); 25 ng/uL pha-1(+) (pBX)	GE24	

Table B.1 Continued

TOL43	*aatEx25*	*myo-3p::nls::RCaMP2; myo-3p::nls::eGFP; pha-1(+); pha-1(lf) e2123 III*	50 ng/uL myo-3p::nls::RCaMP2 (pLQ1); 25 ng/uL myo-3p::nls::eGFP (pLD28); 25 ng/uL pha-1(+) (pBX)	GE24	
		unc-25p::Cerulean; acr-2p::wrmScarlet; pha-1(+); pha-1(lf) e2123 III	50 ng/uL unc-25p::Cerulean (pLJ4); 25 ng/uL acr-2p::wrmScarlet(pLD11) ; 25 ng/uL pha-1(+) (pBX)	GE24	acr-2p::wrmScarlet did not express well. Cerulean can be detected using fluorescent dissecting microscope under green channel
		del-1p(2.6kb from N2)::Cerulean; unc-25p::wrmScarlet; pha-1(+); pha-1(lf) e2123 III	50 ng/uL del-1p(2.6kb from N2)::Cerulean (pSV4); 25 ng/uL unc-25p::wrmScarlet (pLJ3); 25 ng/uL pha-1(+) (pBX)	GE24	pSV4 did not express
TOL50	*aatEx26*	*unc-25p::Cerulean; acr-2p::wrmScarlet; pha-1(+); pha-1(lf) e2123 III*	40 ng/uL unc-25p::Cerulean (pLJ4); 35 ng/uL acr-2p::wrmScarlet(pLD11) ; 25 ng/uL pha-1(+) (pBX)	GE24	
		del-1p::wrmScarlet; unc-25::Cerulean; pha-1(+); pha-1(lf) e2123 III	35 ng/uL del-1p::wrmScarlet (pLJ1); 40 ng/uL unc-25::Cerulean (pLJ4); 25 ng/uL pha-1(+) (pBX)	GE24	pLJ1's expression is not stable
		(2.6kb from N2) del-1p::Cerulean; ttx-3p::wrmScarlet; pha-1(+); pha-1(lf) e2123 III	50 ng/uL del-1p(2.6kb from N2)::Cerulean (pSV4); 25 ng/uLttx-3p::wrmScarlet; 25 ng/uL pha-1(+)	GE24	We did not see the expression of (2.6kb from N2) del-1p::Cerulean
		(1.85kb from N2) del-1p::unc-49A::sl2::eGFP; unc-49 (lf/ko) tm5487	30 ng/uL (1.85kb from N2) del-1p::unc-49A::sl2::eGFP (pLD27); 70 ng/uL pBlueScript	TM5487 [unc-49 ko III]	
TOL51	*aatEx27*	*myo-3p::unc-49C::sl2::eGFP; unc-49 (lf/ko) tm5487*	30 ng/uL myo-3p::unc-49C::sl2::eGFP (pLD26); 70 ng/uL pBlueScript	TM5487 [unc-49 ko III]	myo-3p UNC49C rescue
TOL52	*aatEx28*	*unc-25p::unc-49C::sl2::eGFP; unc-49 (lf/ko) tm5487*	30 ng/uL unc-25p::unc-49C::sl2::eGFP (pLD20); 70 ng/uL pBlueScript	TM5487 [unc-49 ko III]	Expression Pattern: D motoneurons ONLY

Table B.1 Continued

TOL53	*aatEx29*	*unc-25p::unc-49C::sl2::eGFP; unc-49 (lf/ko) tm5487*	30 ng/uL unc-25p::unc-49C::sl2::eGFP (pLD20); 70 ng/uL pBlueScript	TM5487 [unc-49 ko III]	eGFP in D motoneurons and Body-wall Muscles
		myo-3p::unc-49C::sl2::eGFP; unc-49 (lf/ko) tm5487	50 ng/uL myo-3p::unc-49C::sl2::eGFP (pLD26); 50 ng/uL pBlueScript	TM5487 [unc-49 ko III]	The same expression pattern as injLAN17 and injLAN18.
		unc-25p::unc-49C::sl2::eGFP; unc-49 (lf/ko) tm5487	50 ng/uL unc-25p::unc-49C::sl2::eGFP (pLD20); 50 ng/uL pBlueScript	TM5487 [unc-49 ko III]	
TOL54	*aatEx30*	*del-1::Arch::GFP; pha-1(+); pha-1(lf) e2123 III*	50 ng/uL del-1::Arch::GFP (pOKA73); 40 ng/uL pha-1(+) (pBX)	GE24	
TOL49	*aatEx49*	*del-1p::wrmScarlet; unc-25::Cerulean; pha-1(+); pha-1(lf) e2123 III*	35ng/uL del-1p::wrmScarlet(pLD30) ; 25 ng/uL unc-25p::Cerulean (pLJ4); 40 ng/uL pha-1(+) (pBX)	GE24	Identification Strain of DD, A and B Motoneurons
TOL56	*aatEx31*	*del-1p::unc-49 subunit C::sl2::eGFP; unc-49 (lf/ko) tm5487*	50ng/uL del-1p::unc-49 subunit C::sl2::eGFP (pLD32); 50ng/uL pBluescript	TM5487 [unc-49 ko III]	eGFP in A- and B-type MNs and Ventral Muscles
TOL62	*aatEx62*	*unc-49p::unc-49 subunit A::sl2::EGFP; otIs669*	20 ng/uL unc-49p::unc-49 subunit A::sl2::EGFP (pLD17); 80 ng/uL pBluescript	OH15262 (otIs669)	
TOL63	*aatEx63*	*unc-49p::unc-49 subunit B::sl2::EGFP; otIs669*	25 ng/uL unc-49p::unc-49 subunit B::sl2::EGFP (pLD18); 75 ng/uL pBluescript	OH15262 (otIs669)	
TOL61	*aatEx61*	*unc-49p::unc-49 subunit C::sl2::EGFP; otIs669*	20 ng/uL unc-49p::unc-49 subunit C::sl2::EGFP (pLD19); 80ng/uL pBluescript	OH15262 (otIs669)	
		unc-49p::EGFP	30 ng/uL unc-49p::EGFP (pLD8); 70 ng/uL pBlueScript	OH15262 (otIs669)	No fluorescent animals found
		unc-25p::GCaMP6s; pha-1(lf) e2123 III	50ng/uL unc-25p::GCaMP6s (pVM1); 30 ng/uL pha-1(+) (pBX); 20 ng/uL pBlueScript	GE24	Impossible to see GCaMP6s under fluorescent stereoscope
			30 ng/uL unc-49p::unc-49C::sl2::eGFP (pLD19); 70 ng/uL pBlueScript	TM5487 [unc-49 ko III]	
TOL66	*aatEx66*	*unc-49 (lf/ko) tm5487; unc-49p::unc-49::sl2::egf*	30 ng/uL unc-49p::unc-49 subunit C::sl2::EGFP (pLD19); 70ng/uL pBluescript	TM5487 [unc-49 ko III]	

APPENDIX C

SINGLE-WORM TRACKER

C.1 A single-worm Tracker Used for Crawling Tracking

Before using the multiple-worm tracker, we used a single-worm tracker developed by Yemini and Brown (Yemini and Brown, 2015) to record crawling behavior of wild type and GABA transmission mutants -- CB156, CB177, CB307, CB382 and CB407. These GABA transmission mutants have different single-base pair mutations in different genes of GABA transmission: CB156 has a single base-pair mutation in *unc-25*, CB177 in *unc-46*, CB307 in *unc-47*, and CB382 and CB407 in *unc-49*. These genes translate different proteins in GABA transmission in *C. elegans*: *unc-25* translates GABA synthesis enzyme glutamic acid decarboxylase, *unc-46* and *unc-47* vesicular transporters, and *unc-49* ionotropic GABA receptor (McIntire et al., 1993a; McIntire et al., 1993b).

One day prior to the tracking experiment, animals of the fourth larval stage (L4) were transferred onto a new NGM-agar plate with thick and healthy bacterial lawn (*E. coli*, OP50) and kept at 20°C overnight. For tracking, a single animal was transferred to a 60 mm NGM-agar plate with freshly seeded thin and small bacterial lawn and tracked for 3 minutes; for each strain, 30 animals were tracked using the single-worm tracker.

The tracking apparatus uses a static stage that holds the plate and a motorized USB-microscope (Dino-Lite, AM413-FIT) that keeps the tracked animal in the field of view over time (Yemini and Brown, 2015); the rest of the tracker setup is the same as the multiple worm tracker in Chapter 2.

Other than the tracker and the tracking software, Yemini and Brown developed a complementary Worm Analysis Toolbox to visualize and analyze the behavioral results (https://www.mrc-lmb.cam.ac.uk/wormtracker/index.php?action=analysis) (Yemini and Brown, 2015). However, when we took a closer look at the analyzed results, we found two major flaws. First, the analyzed data contain a lot of abnormal data points. For example, the data points of extremely high frequency or high speed resulting from the video frames when the motorized microscope was moving. Second, the results showed significant differences between almost all the comparisons, even within the same data set, because the Worm Analysis Toolbox uses all the data points for statistics like one-way ANOVA. Therefore, we wrote Matlab program to analyze these locomotion data rather than using the Worm Analysis Toolbox.

C.2 Customized Matlab Codes for Data Cleaning

The data points in which the motorized microscope was moving were removed by the following codes:

```
%Tease out the frames during stage movement
        if TimeS1 ~= MinTime && TimeS1 > MinTime;
          Z = ones(1,MinTime*1797);
          xCoor = worm.path.coordinates.x(Z);
        elseif TimeS1 == TimeS2 == MinTime;
            Z = ones(1,MinTime*1797);
          xCoor = worm.path.coordinates.x(Z);
        else
          xCoor = worm.path.coordinates.x;
        end
  Q = isnan(xCoor);
  k = 1;
  n = length(xCoor);
  NumStart = [];
  NumEnd = [];
  while k< (n-1);
```

```
    NumNaNs = 0;
    if Q(k) == 0; %if the cell is not NaN, continue to check the next cell
        k = k + 1;
    elseif Q(k) == 1; %if the cell is NaN, start counting how many NaNs and the starting
and ending numbers.
        NumStart= [NumStart k]; %put the index of the cell to NoStart
        while (k+1)<(n-1) && Q(k+1) == 1 ;%if the next cell is a NaN again
            k = k+1;
            NumNaNs = NumNaNs + 1; %Start counting how many NaNs in this NaN-piece
        end
        NumEnd = [NumEnd k]; %put the index number of the last NaN cell into NoEnd
        k = k+1;
    end
    end

    NumStart = int16(NumStart); %To debug 'Subscript indices must either be real
positive integers or logicals'
    NumEnd = int16(NumEnd); %To debug 'Subscript indices must either be real positive
integers or logicals'
    m = length(NumStart);
    A = ones(1,n);
    for j = 1:1:m
        if NumStart(j)-7 < 0
            continue
        end
        if NumStart(j)-7 == 0
            A(1,1:(NumEnd(j)+7)) = 0;
        else
            A(1, (NumStart(j)-7):(NumEnd(j)+7)) = 0;
        end
    end
    A =logical(A);
    speed = worm.locomotion.velocity.midbody.speed;
    speed = speed(:,A);
    freq = abs(worm.locomotion.bends.midbody.frequency(:,A));
    amp = worm.posture.amplitude.max(:,A);
    wav = worm.posture.wavelength.primary(:,A);
    singlespeed = [singlespeed speed];
    singlefreq = [singlefreq freq];
    singleamp = [singleamp amp];
    singlewav = [singlewav wav];
        end
        [A] = TeaseOutSmallPieces (singlespeed);
        if sum(A)< length(A)
        singlespeed(~A) = NaN;
        end
```

In addition, we found that there were some small pieces of data points containing abnormal data as well. Therefore, we further took out these small pieces of data points by the following Matlab function 'TeaseOutSamllPieces':

```
function [A] = TeaseOutSmallPieces (StrainData)
n = length(StrainData);
A = ~isnan(StrainData);%convert freq array into 1 and 0: 0 means NAN
j=1; %j is the number of the element in array A
b = 0; %Debug: some data are not start with NaN, but real number
while j < (n-1)
if A(j) == 0 && A(j+1) == 0 %if there is a piece which comprises of several NANs
   j = j + 1; % jump into the next element of the freq array
elseif A(j)==0 && A(j+1) == 1 %when start to meet '1' in array A
   b = 0; % a is the length of the video stretch. Start to count the length
   j = j + 1;
elseif A(j)==1 && A(j+1)==1 %continue to count the length, variable is a
   b = b + 1;
   j = j + 1;
else
   if b < 10 % if the length of a video stretch is shorter than 10, then it will be designed as
a junk piece. It will be erased.
      A(j-b:j) = 0; %erase the junk piece
      j = j + 1;
   else j = j + 1;
   end
end
end
```

C.3 Single Base-pair Mutations in the Genes involving GABA Transmission Resulted in Slow Crawling Locomotion

We had gotten similar results as the ones we got from GABA transmission knockout strains tracked by the multiple worm tracker: when GABA transmission is compromised because of single base pair mutation, *C. elegans* crawls in lower translocation speed and undulation frequency (Figure C.1). Moreover, we quantified the undulation frequency of these mutants during forward and backward crawling separately. In each moving direction of each strain,

we calculated the average of translocation speed and undulation frequency of each animal, then used these averages to estimate the population means and determined statistic differences. Similar to the results of GABA transmission knockout strains during crawling, the translocation speeds of the GABA transmission single-base pair mutants are significantly lower than that of wild type (data not shown). Even though the estimated population means of undulation frequency of the mutants are lower than that of wild type, majority of the mutant strains are not different from wild type statistically. Only CB156 during backward crawling, CB382 and CB407 show significant differences in undulation frequency compared to wild type N2 (Figure C.2). At that moment, we introduced the multiple worm tracker and the GABA transmission knockout strains, so we ceased in using the single-worm tracker for tracking and switched to the multiple worm tracker.

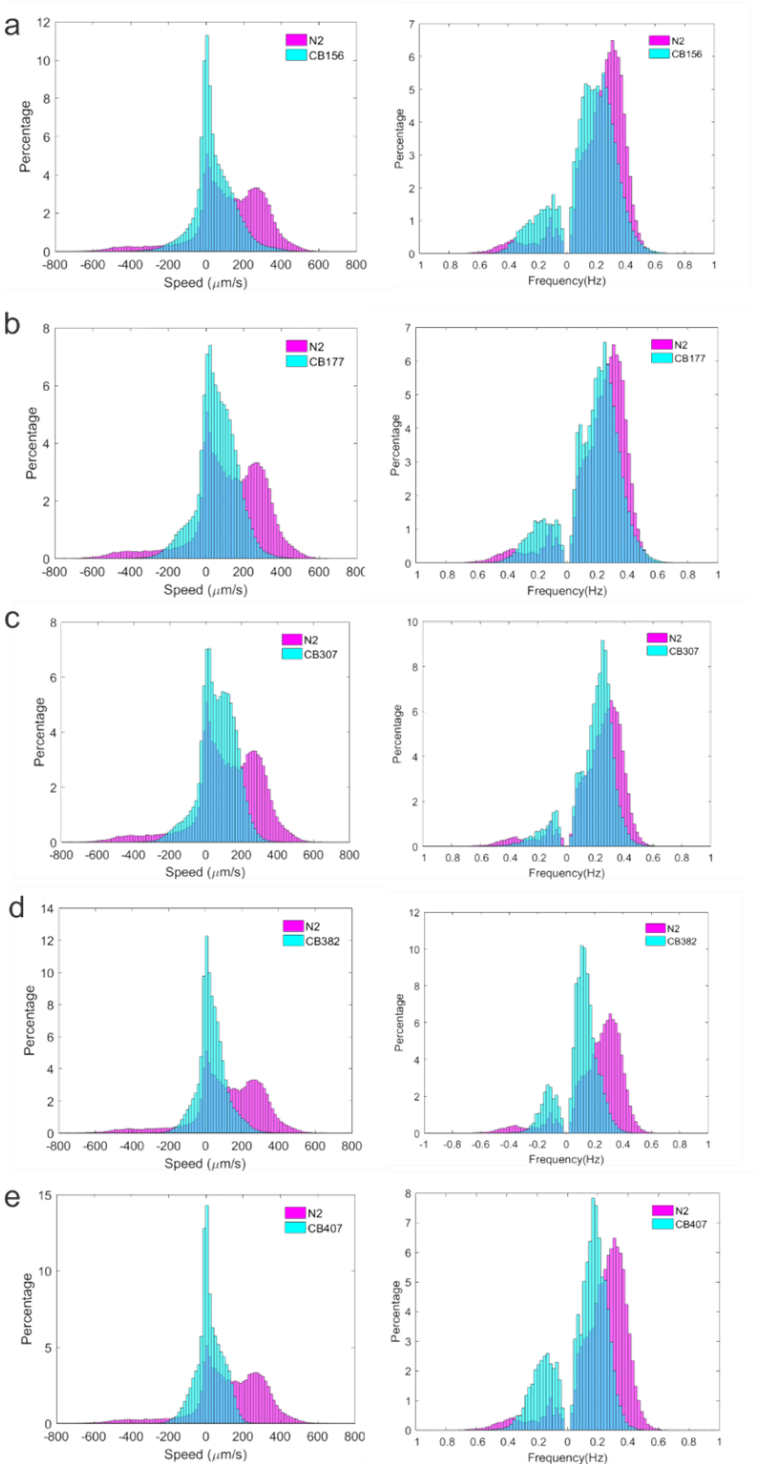

Figure C.1 Compared to wild type strain N2, the GABA transmission mutant strains have single base pairs mutations showed more data distribution in low translocation speed and low undulation frequency during free crawling. These single-base pair mutant strains are defective in GABA synthesis (a), GABA transporting (b and c) and GABA reception (d and e).

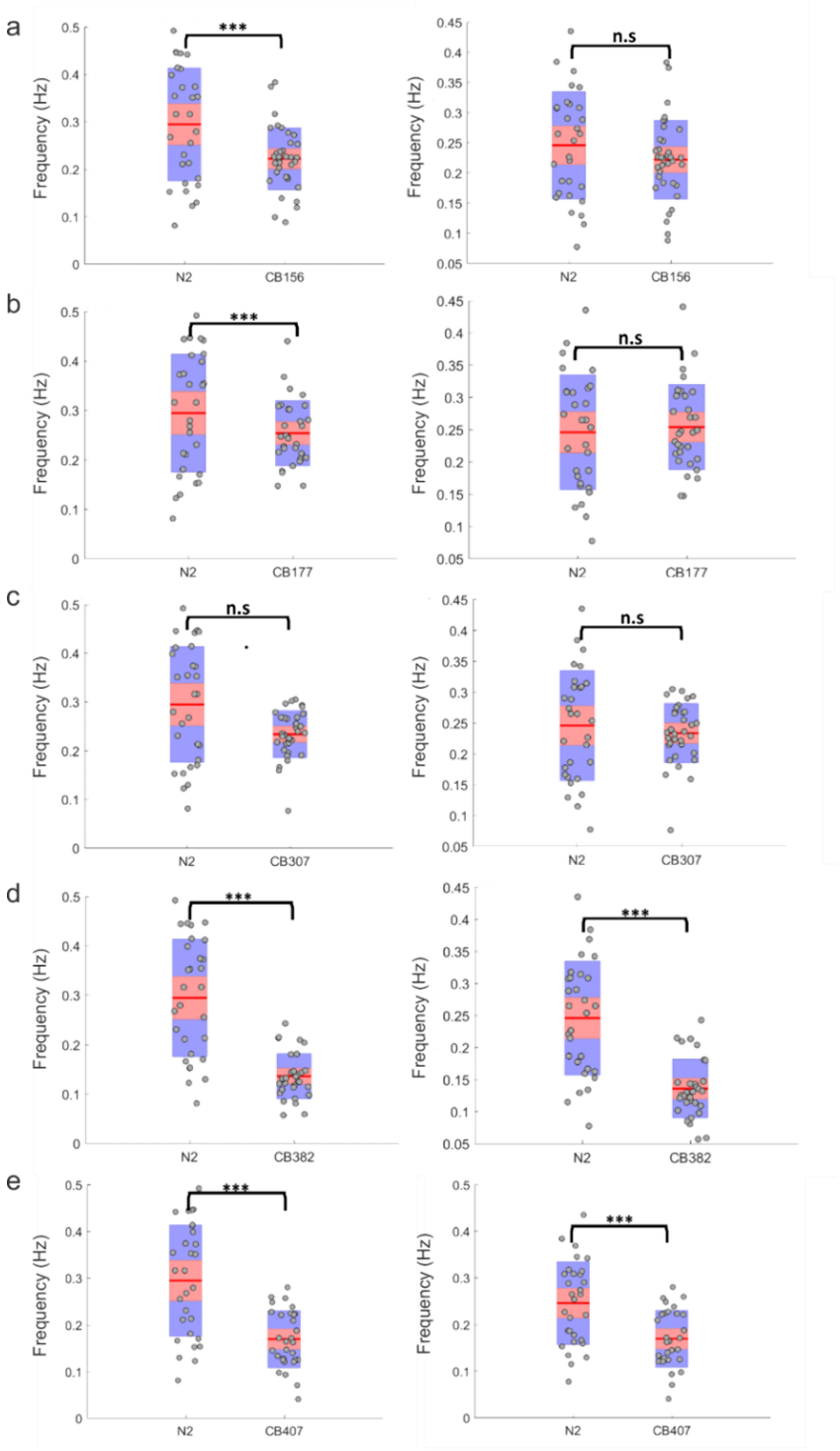

Figure C.2 The GABA transmission single base pair mutant strains crawled in low undulation frequency. ANOVA with Tukey's multiple comparison test, n.s. $p>0.5$, *** $p<0.001$.

REFERENCES

Ahringer J (2006) Reverse genetics. In: *WormBook,* ed. The *C elegans* Research Community, WormBook.

Alon U (2007) An introduction to systems biology : design principles of biological circuits. Boca Raton, FL: Chapman & Hall/CRC.

Altun ZF, Hall DH (2020) Handbook of *C. elegans* Anatomy. In *WormAtlas*.

Altun ZF, Chen B, Wang ZW, Hall DH (2009) High resolution map of *Caenorhabditis elegans* gap junction proteins. Developmental Dynamics 238:1936-1950.

Bamber BA, Beg AA, Twyman RE, Jorgensen EM (1999) The *Caenorhabditis elegans* unc-49 locus encodes multiple subunits of a heteromultimeric GABA receptor. The Journal of Neuroscience 19:5348-5359.

Bamber BA, Richmond JE, Otto JF, Jorgensen EM (2005) The composition of the GABA receptor at the *Caenorhabditis elegans* neuromuscular junction. British Journal of Pharmacology 144:502-509.

Bargmann CI (1998) Neurobiology of the *Caenorhabditis elegans* genome. Science 282:2028-2033.

Beg AA, Jorgensen EM (2003) EXP-1 is an excitatory GABA-gated cation channel. Nature Neuroscience 6:1145-1152.

Berri S, Boyle JH, Tassieri M, Hope IA, Cohen N (2009) Forward locomotion of the nematode *C. elegans* is achieved through modulation of a single gait. HFSP Journal 3:186-193.

Boulin T, Gielen M, Richmond JE, Williams DC, Paoletti P, Bessereau JL (2008) Eight genes are required for functional reconstitution of the *Caenorhabditis elegans* levamisole-sensitive acetylcholine receptor. Proceedings of the National Academy of Sciences of the United States of America 105:18590-18595.

Boyle JH, Berri S, Cohen N (2012) Gait modulation in *C. elegans*: an integrated neuromechanical model. Frontiers in Computational Neuroscience 6:10.

Brenner S (1974) The genetics of *Caenorhabditis elegans*. Genetics 77:71-94.

Broekmans OD, Rodgers JB, Ryu WS, Stephens GJ (2016) Resolving coiled shapes reveals new reorientation behaviors in *C. elegans*. eLife 5.

Butler VJ, Branicky R, Yemini E, Liewald JF, Gottschalk A, Kerr RA, Chklovskii DB, Schafer WR (2015) A consistent muscle activation strategy underlies crawling and swimming in *Caenorhabditis elegans*. Journal of the Royal Society Interface 12:20140963.

Byerly L, Cassada RC, Russell RL (1976) The life cycle of the nematode *Caenorhabditis elegans*. I. Wild-type growth and reproduction. Developmental Biology 51:23-33.

Chalfie M, Tu Y, Euskirchen G, Ward WW, Prasher DC (1994) Green fluorescent protein as a marker for gene expression. Science 263:802-805.

Chalfie M, Sulston JE, White JG, Southgate E, Thomson JN, Brenner S (1985) The neural circuit for touch sensitivity in *Caenorhabditis elegans*. The Journal of Neuroscience 5:956-964.

Chen BL, Hall DH, Chklovskii DB (2006) Wiring optimization can relate neuronal structure and function. Proceedings of the National Academy of Sciences of the United States of America 103:4723-4728.

Chronis N, Zimmer M, Bargmann CI (2007) Microfluidics for in vivo imaging of neuronal and behavioral activity in *Caenorhabditis elegans*. Nature methods 4:727-731.

Chung SH, Sun L, Gabel CV (2013) In *vivo* neuronal calcium imaging in *C. elegans*. Journal of Visualized Experiments.

Cohen N, Sanders T (2014) Nematode locomotion: dissecting the neuronal-environmental loop. Current Opinion in Neurobiology 25:99-106.

Cohen N, Ranner T (2017) A new computational method for a model of *C. elegans* biomechanics: insights into elasticity and locomotion performance. arXiv 170204988.

Cohen N, Denham J (2019) Whole animal modeling: piecing together nematode locomotion. Current Opinion in Systems Biology 13:150-160.

Consortium CeS (1998) Genome sequence of the nematode *C. elegans*: a platform for investigating biology. Science 282:2012-2018.

Cormack BP, Valdivia RH, Falkow S (1996) FACS-optimized mutants of the green fluorescent protein (GFP). Gene 173:33-38.

Corsi AK, Wightman B, Chalfie M (2015) A Transparent window into biology: a primer on *Caenorhabditis elegans*. In *WormBook*:1-31.

de Bono M, Maricq AV (2005) Neuronal substrates of complex behaviors in *C. elegans*. Annual Review of Neuroscience 28:451-501.

Del Castillo J, De Mello WC, Morales T (1967) The initiation of action potentials in the somatic musculature of *Ascaris lumbricoides*. The Journal of Experimental Biology 46:263-279.

Delcastillo J, Demello WC, Morales T (1963) The physiological role of acetylcholine in the neuromuscular system of *Ascaris lumbricoides*. Archives Internationales de Physiologie, de Biochimie et de Biophysique 71:741-757.

Denham JE, Ranner T, Cohen N (2018) Signatures of proprioceptive control in *Caenorhabditis elegans* locomotion. Philosophical Transactions of the Royal Society 373.

Donnelly JL, Clark CM, Leifer AM, Pirri JK, Haburcak M, Francis MM, Samuel AD, Alkema MJ (2013) Monoaminergic orchestration of motor programs in a complex *C. elegans* behavior. PLoS Biology 11:e1001529.

El Mouridi S, Lecroisey C, Tardy P, Mercier M, Leclercq-Blondel A, Zariohi N, Boulin T (2017) Reliable CRISPR/Cas9 genome engineering in *Caenorhabditis elegans* using a single efficient sgRNA and an easily recognizable phenotype. G3: Genes, Genomes, Genetics 7:1429-1437.

Emmons SW (2015) The beginning of connectomics: a commentary on White et al. (1986) 'The structure of the nervous system of the nematode *Caenorhabditis elegans*'. Philosophical Transactions of the Royal Society B: Biological Sciences 370.

Esmaeili B, Ross JM, Neades C, Miller DM, 3rd, Ahringer J (2002) The *C. elegans* even-skipped homologue, *vab-7*, specifies DB motoneurone identity and axon trajectory. Development 129:853-862.

Fang-Yen C, Wyart M, Xie J, Kawai R, Kodger T, Chen S, Wen Q, Samuel AD (2010) Biomechanical analysis of gait adaptation in the nematode *Caenorhabditis elegans*. Proceedings of the National Academy of Sciences of the United States of America 107:20323-20328.

Fleming JT, Squire MD, Barnes TM, Tornoe C, Matsuda K, Ahnn J, Fire A, Sulston JE, Barnard EA, Sattelle DB, Lewis JA (1997) *Caenorhabditis elegans* levamisole resistance genes *lev-1*, *unc-29*, and *unc-38* encode functional nicotinic acetylcholine receptor subunits. The Journal of Neuroscience 17:5843-5857.

Gally C, Bessereau JL (2003) GABA is dispensable for the formation of junctional GABA receptor clusters in *Caenorhabditis elegans*. The Journal of Neuroscience 23:2591-2599.

Gao S, Zhen M (2011) Action potentials drive body wall muscle contractions in *Caenorhabditis elegans*. Proceedings of the National Academy of Sciences of the United States of America 108:2557-2562.

Gao S, Guan SA, Fouad AD, Meng J, Kawano T, Huang YC, Li Y, Alcaire S, Hung W, Lu Y, Qi YB, Jin Y, Alkema M, Fang-Yen C, Zhen M (2018) Excitatory motor neurons are local oscillators for backward locomotion. eLife 7.

Gendrel M, Atlas EG, Hobert O (2016) A cellular and regulatory map of the GABAergic nervous system of *C. elegans*. eLife 5.

Gershenson C, Helbing D (2015) When slower is faster. arXiv 21(2):9-15.2015.

Gibson DG, Young L, Chuang RY, Venter JC, Hutchison CA, 3rd, Smith HO (2009) Enzymatic assembly of DNA molecules up to several hundred kilobases. Nature Methods 6:343-345.

Gibson DG et al. (2010) Creation of a bacterial cell controlled by a chemically synthesized genome. Science 329:52-56.

Gjorgjieva J, Biron D, Haspel G (2014) Neurobiology of *Caenorhabditis elegans* locomotion: where do we stand? Bioscience 64:476-486.

Gokirmak T, Campanale JP, Shipp LE, Moy GW, Tao H, Hamdoun A (2012) Localization and substrate selectivity of sea urchin multidrug (MDR) efflux transporters. Journal of Biological Chemistry 287:43876-43883.

Gray J, Lissmann HW (1964) The locomotion of nematodes. The Journal of Experimental Biology 41:135-154.

Haspel G, O'Donovan MJ (2011) A perimotor framework reveals functional segmentation in the motoneuronal network controlling locomotion in *Caenorhabditis elegans*. The Journal of Neuroscience 31:14611-14623.

Haspel G, O'Donovan MJ, Hart AC (2010) Motoneurons dedicated to either forward or backward locomotion in the nematode *Caenorhabditis elegans*. The Journal of Neuroscience 30:11151-11156.

Inoue M, Takeuchi A, Horigane S, Ohkura M, Gengyo-Ando K, Fujii H, Kamijo S, Takemoto-Kimura S, Kano M, Nakai J, Kitamura K, Bito H (2015) Rational design of a high-affinity, fast, red calcium indicator R-CaMP2. Nature Methods 12:64-70.

Izquierdo EJ, Beer RD (2018) From head to tail: a neuromechanical model of forward locomotion in *Caenorhabditis elegans*. Philosophical Transactions of the Royal Society B: Biological Sciences 373.

Javer A, Currie M, Lee CW, Hokanson J, Li K, Martineau CN, Yemini E, Grundy LJ, Li C, Ch'ng Q, Schafer WR, Nollen EAA, Kerr R, Brown AEX (2018) An open-source platform for analyzing and sharing worm-behavior data. Nature Methods 15:645-646.

Jin Y, Jorgensen E, Hartwieg E, Horvitz HR (1999) The *Caenorhabditis elegans* gene unc-25 encodes glutamic acid decarboxylase and is required for synaptic transmission but not synaptic development. The Journal of Neuroscience 19:539-548.

Jobson MA, Valdez CM, Gardner J, Garcia LR, Jorgensen EM, Beg AA (2015) Spillover transmission is mediated by the excitatory GABA receptor LGC-35 in *C. elegans*. The Journal of Neuroscience 35:2803-2816.

Kagawa-Nagamura Y, Gengyo-Ando K, Ohkura M, Nakai J (2018) Role of tyramine in calcium dynamics of GABAergic neurons and escape behavior in *Caenorhabditis elegans*. Zoological Letter 4:19.

Karbowski J, Cronin CJ, Seah A, Mendel JE, Cleary D, Sternberg PW (2006) Conservation rules, their breakdown, and optimality in Caenorhabditis sinusoidal locomotion. Journal of Theoretical Biology 242:652-669.

Kiehn O (2011) Development and functional organization of spinal locomotor circuits. Current Opinion in Neurobiology 21:100-109.

Kiehn O (2016) Decoding the organization of spinal circuits that control locomotion. Nature reviews Neuroscience 17:224-238.

Lickteig KM, Duerr JS, Frisby DL, Hall DH, Rand JB, Miller DM, 3rd (2001) Regulation of neurotransmitter vesicles by the homeodomain protein UNC-4 and its transcriptional corepressor UNC-37/groucho in *Caenorhabditis elegans* cholinergic motor neurons. The Journal of Neuroscience 21:2001-2014.

Lighthill M (1960) Note on the swimming of slender fish. Journal of Fluid Mechanics 9:305-317.

Liu P, Chen B, Wang ZW (2014) SLO-2 potassium channel is an important regulator of neurotransmitter release in *Caenorhabditis elegans*. Nature Communications 5:5155.

Lockery SR, Lawton KJ, Doll JC, Faumont S, Coulthard SM, Thiele TR, Chronis N, McCormick KE, Goodman MB, Pruitt BL (2008) Artificial dirt: microfluidic substrates for nematode neurobiology and behavior. Journal of Neurophysiology 99:3136-3143.

Maro GS, Gao S, Olechwier AM, Hung WL, Liu M, Ozkan E, Zhen M, Shen K (2015) MADD-4/Punctin and neurexin organize *C. elegans* GABAergic postsynapses through neuroligin. Neuron 86:1420-1432.

Mattis J, Tye KM, Ferenczi EA, Ramakrishnan C, O'Shea DJ, Prakash R, Gunaydin LA, Hyun M, Fenno LE, Gradinaru V, Yizhar O, Deisseroth K (2011) Principles for applying optogenetic tools derived from direct comparative analysis of microbial opsins. Nature Methods 9:159-172.

McIntire SL, Jorgensen E, Horvitz HR (1993a) Genes required for GABA function in *Caenorhabditis elegans*. Nature 364:334-337.

McIntire SL, Jorgensen E, Kaplan J, Horvitz HR (1993b) The GABAergic nervous system of *Caenorhabditis elegans*. Nature 364:337-341.

Mellem JE, Brockie PJ, Madsen DM, Maricq AV (2008) Action potentials contribute to neuronal signaling in *C. elegans*. Nature Neuroscience 11:865-867.

Mello C, Fire A (1995) DNA transformation. Methods Cell Biology 48:451-482.

Miller DM, Shen MM, Shamu CE, Burglin TR, Ruvkun G, Dubois ML, Ghee M, Wilson L (1992) *C. elegans unc-4* gene encodes a homeodomain protein that determines the pattern of synaptic input to specific motor neurons. Nature 355:841-845.

Miller DM, 3rd, Niemeyer CJ (1995) Expression of the *unc-4* homeoprotein in *Caenorhabditis elegans* motor neurons specifies presynaptic input. Development 121:2877-2886.

Mongan NP, Baylis HA, Adcock C, Smith GR, Sansom MS, Sattelle DB (1998) An extensive and diverse gene family of nicotinic acetylcholine receptor alpha subunits in *Caenorhabditis elegans*. Receptors Channels 6:213-228.

Nagel G, Brauner M, Liewald JF, Adeishvili N, Bamberg E, Gottschalk A (2005) Light activation of channelrhodopsin-2 in excitable cells of *Caenorhabditis elegans* triggers rapid behavioral responses. Current Biology : CB 15:2279-2284.

Nicholl GC, Jawad AK, Weymouth R, Zhang H, Beg AA (2017) Pharmacological characterization of the excitatory 'Cys-loop' GABA receptor family in *Caenorhabditis elegans*. British Journal of Pharmacology 174:781-795.

Okazaki A, Sudo Y, Takagi S (2012) Optical silencing of *C. elegans* cells with arch proton pump. PloS One 7:e35370.

Petrash HA, Philbrook A, Haburcak M, Barbagallo B, Francis MM (2013) ACR-12 ionotropic acetylcholine receptor complexes regulate inhibitory motor neuron activity in *Caenorhabditis elegans*. The Journal of Neuroscience 33:5524-5532.

Petzold BC, Park SJ, Ponce P, Roozeboom C, Powell C, Goodman MB, Pruitt BL (2011) *Caenorhabditis elegans* body mechanics are regulated by body wall muscle tone. Biophysical Journal 100:1977-1985.

Pierce-Shimomura JT, Chen BL, Mun JJ, Ho R, Sarkis R, McIntire SL (2008) Genetic analysis of crawling and swimming locomotory patterns in *C. elegans*. Proceedings of the National Academy of Sciences of the United States of America 105:20982-20987.

Roberts A, Li WC, Soffe SR (2008) Roles for inhibition: studies on networks controlling swimming in young frog tadpoles. Journal of Comparative Physiology A: Neuroethology, Sensory, Neural, and Behavioral Physiology 194:185-193.

Schuske K, Beg AA, Jorgensen EM (2004) The GABA nervous system in *C. elegans*. Trends in Neurosciences 27:407-414.

Stephens GJ, Johnson-Kerner B, Bialek W, Ryu WS (2008) Dimensionality and dynamics in the behavior of *C. elegans*. PLOS Computational Biology 4:e1000028.

Sulston JE, Horvitz HR (1977) Post-embryonic cell lineages of the nematode, *Caenorhabditis elegans*. Developmental Biology 56:110-156.

Sulston JE, Schierenberg E, White JG, Thomson JN (1983) The embryonic cell lineage of the nematode *Caenorhabditis elegans*. Developmental Biology 100:64-119.

Tavernarakis N, Shreffler W, Wang S, Driscoll M (1997) *unc-8*, a DEG/ENaC family member, encodes a subunit of a candidate mechanically gated channel that modulates *C. elegans* locomotion. Neuron 18:107-119.

Tolstenkov O, Van der Auwera P, Steuer Costa W, Bazhanova O, Gemeinhardt TM, Bergs AC, Gottschalk A (2018) Functionally asymmetric motor neurons contribute to coordinating locomotion of *Caenorhabditis elegans*. eLife 7.

Touroutine D, Fox RM, Von Stetina SE, Burdina A, Miller DM, 3rd, Richmond JE (2005) *acr-16* encodes an essential subunit of the levamisole-resistant nicotinic receptor at the *Caenorhabditis elegans* neuromuscular junction. Journal of Biological Chemistry 280:27013-27021.

Venkatachalam V, Ji N, Wang X, Clark C, Mitchell JK, Klein M, Tabone CJ, Florman J, Ji H, Greenwood J, Chisholm AD, Srinivasan J, Alkema M, Zhen M, Samuel AD (2016) Pan-neuronal imaging in roaming *Caenorhabditis elegans*. Proceedings of the National Academy of Sciences of the United States of America 113:E1082-1088.

Wen Q, Po MD, Hulme E, Chen S, Liu X, Kwok SW, Gershow M, Leifer AM, Butler V, Fang-Yen C, Kawano T, Schafer WR, Whitesides G, Wyart M, Chklovskii DB, Zhen M, Samuel AD (2012) Proprioceptive coupling within motor neurons drives *C. elegans* forward locomotion. Neuron 76:750-761.

White JG, Southgate E, Thomson JN, Brenner S (1976) The structure of the ventral nerve cord of *Caenorhabditis elegans*. Philosophical Transactions of the Royal Society B: Biological Sciences 275:327-348.

White JG, Southgate E, Thomson JN, Brenner S (1986) The structure of the nervous system of the nematode *Caenorhabditis elegans*. Philosophical Transactions of the Royal Society B: Biological Sciences 314:1-340.

Yanik MF, Cinar H, Cinar HN, Chisholm AD, Jin Y, Ben-Yakar A (2004) Neurosurgery: functional regeneration after laser axotomy. Nature 432:822.

Yemini EI, Brown AE (2015) Tracking single *C. elegans* using a USB microscope on a motorized stage. Methods in Molecular Biology 1327:181-197.